

Advances on Ruthenate Oxides through Transport and Spectroscopy Experiments

Dissertation

zur

Erlangung der naturwissenschaftlichen Doktorwürde

(Dr. sc. nat.)

vorgelegt der

Mathematisch-naturwissenschaftlichen Fakultät

der

Universität Zürich

von

Lakshmi Das Thazheveetil

Promotionskommission

Prof. Dr. Johan Chang (Vorsitz und Leitung der Dissertation)

Prof. Dr. Titus Neupert

Dr. Jonathan White

Dr. David Leboeuf

Zürich, 2020

Abstract

Transition metal oxides with $4d$ or $5d$ electrons exhibit a multitude of intriguing magnetic and electronic properties, including unconventional superconductivity, Mott transitions, spin orbital ordering, colossal magnetoresistance, to name a few, which are dictated by various interactions like hopping, electron correlations, spin orbit coupling, electron - phonon coupling etc. The highly extended nature of the $4d$ orbitals results in competition between comparable energy scales set by local interactions, including the Coulomb interaction, Hund's coupling and crystal field (CF) terms, together with intrinsic spin-orbit coupling (SOC) of transition metal ions. Hence in these materials, small perturbations can induce significant changes in their physical properties giving rise to a class of exotic phenomena rarely found in other materials. Perovskite ruthenium oxides of the Ruddlesden-Popper (RP) series, $(\text{Sr}/\text{Ca})_{n+1}\text{Ru}_n\text{O}_{3n+1}$ have attracted interest due to the discovery of unconventional superconductivity in Sr_2RuO_4 . Additionally these materials exhibit structural resemblance to cuprate superconductors and have been in the last two decades among the leading topic in condensed matter physics. The current interest in ruthenate materials encompasses studies beyond the nature of superconductivity in Sr_2RuO_4 .

While Sr_2RuO_4 is a metal and could be described within the framework of the Fermi - liquid theory, the isovalent substitution of Sr by Ca results in the $n = 1$ member - Ca_2RuO_4 - of the RP series, which is an insulator that shows a metal insulator transition at 356 K and a Néel transition at 110 K resulting in an anti ferromagnetic Mott insulator state. The metal insulator transition in this material has been proposed to be of the Mott Hubbard type resulting from the smaller size of the Ca^{2+} ions in comparison to the Sr^{2+} resulting in lattice distortions. Although the mechanism behind rendering the $2/3$ filled t_{2g} bands insulating has been credited to Mott type physics, the nature of Mott transition in Ca_2RuO_4 has been a subject of debate for decades with different scenarios proposed for the orbital occupancy. Thus, the need for a deeper understanding of this mechanism constituted one of the primary objectives of this study. Here, in the first part of the thesis, a high resolution oxygen K -edge resonant inelastic x - ray scattering (RIXS) study of the antiferromagnetic Mott insulating state of

Ca₂RuO₄ is presented. Our results strongly support a spin - orbit coupled band-Mott scenario - characterized by orbitally selective coexistence of a band and a Mott gap. From our studies we were able to conclude that the band - Mott scenario is triggered by a crystal field that renders the d_{xy} orbital band insulating with the half filled $d_{xz/yz}$ bands undergoing Mott transition driven by Coulomb interaction. RIXS study also showed a set of low - energy excitations (about 80 and 400 meV) and high - energy excitations (about 1.3 and 2.2 eV) , exhibiting strong incident light polarization dependence. With the support from theoretical modelling, the low - energy excitations were interpreted as a result of composite spin-orbital excitations. Their nature unveils the delicate and complicated interplay of crystal - field splitting and spin - orbit coupling in the band-Mott scenario. The high - energy excitations correspond to intra - atomic singlet - triplet transitions at an energy scale set by Hund's coupling. Our findings give a unifying picture of the spin and orbital excitations in the band-Mott insulator Ca₂RuO₄.

One of the most intriguing compounds belonging to RP series is Ca₃Ru₂O₇ ($n = 2$) which is a bilayered system intermediate between the Mott insulating antiferromagnet Ca₂RuO₄ ($n = 1$) and the metallic paramagnet CaRuO₃ ($n = \infty$). It undergoes an antiferromagnetic ordering at 56K and an insulating transition at 48K. It exhibits a variety of exotic phenomena including high sensitivity to impurities (even with minute amount of substitution of Ruthenium with Titanium about $\sim 0.03\%$) resulting in a Mott metal-insulator transition , metamagnetic transition, Colossal Magneto Resistance, and Shubnikov-de Hass oscillations. Recent angle resolved photo emission spectroscopy (ARPES) measurements have unveiled that the system undergoes multiple Fermi surface reconstructions concomitant with the various transitions in the system . Embarking on a strategy to exploit this electronic reconstruction in Ca₃Ru₂O₇, that results in electron like and hole like bands at low temperature, we performed magnetoresistance and magnetisation measurements and derived an analytical formulation of the conductivity of a two-band system . In this approach, electron and hole carrier densities and their respective conductivities are mapped into a two-dimensional phase space. Provided that the carrier density of one type of carrier is known, the dimensionless phase space can be explored through magnetoresistance measurements. While the low-temperature magnetoresistance is consistent with a two-band structure, the study shows that an electronic transition at $T = 30$ K triggers a more complex Fermi surface rendering the model unusable above this temperature scale. Finally, we discuss how the analytical formulation combined with magnetoresistance experiments can be used to evaluate a given system's compliance with a two - band model.

The thesis also briefly presents thermoelectric measurements carried out on various samples using a home - built thermoelectric setup, developed during the course of my PhD work, for measuring thermopower, thermal Hall and Nernst effect in the Quantum Design Physical Property Measurement System(PPMS) .

The set up has been used to study a variety of samples, including thermopower and anomalous contribution to the Nernst effect on samples like Type I Weyl semimetal-PrAlGe, which is a very interesting system in the sense that it breaks both time and inversion symmetry and could be a potential candidate material for carrying pure spin currents. Measurements were also conducted on thermoelectric properties of the bilayer ruthenate $\text{Ca}_3\text{Ru}_2\text{O}_7$ where it was used to understand the anomalies in thermoelectric power concomitant with the change in the topology or the reconstruction of Fermi surface across a transition temperature. Recently, Anomalous Hall effect stemming from berry curvature effects in topological semimetal EuCd_2As_2 was reported. EuCd_2As_2 is hence a prime candidate material to study other exotic phenomena like anomalous/topological Nernst effect which is the thermoelectric analogue to topological Hall effect. The thermoelectric measurements carried out in this system showed the presence of an exotic topological Nernst effect stemming from berry curvature associated with Weyl nodes.

KEYWORDS: Transition Metal Oxides, Ruthenates, Mott Hubbard Insulator, Spin-Orbital excitations, Magnetoresistance, Two-bandmodel, Thermopower, Nernst Effect .

The thesis is organized as follows:

- Chapter 1 gives an overview about the mechanisms responsible for the physics of ruthenates. The chapter also gives a brief overview of the different members in the ruthenate Ruddleson Popper series
- Experimental methodology is discussed in Chapter 2. Information is given about detwinning techniques, laboratory Laue X- ray diffraction setup- used for the prealignment of the crystals, and the synchrotron beamlines, at which X - ray absorption spectroscopy (XAS) and RIXS studies were carried out. The chapter also discusses succinctly the resistivity, Hall and thermoelectric measurement set ups used for the studies presented in this thesis.
- The results of XAS and RIXS study on Ca_2RuO_4 is presented in this section .
- Chapter 4 describes the application of two-band model to the magnetoresistance data of $\text{Ca}_3\text{Ru}_2\text{O}_7$. The analytical formulation is also applied for other systems.

- Chapter 5 is the penultimate bonus chapter that discusses thermopower measurements performed on systems: PrAlGe and EuCd₂As₂ using a home - built thermoelectric probe in the PPMS.
- The main results and conclusions of this work are summarized in this last chapter.

Contents

Abstract	iii
List of Abbreviations	ix
1 Introduction	1
1.1 General overview of Layered Ruthenates	12
1.1.1 Infinite Layered compounds	12
1.1.2 Single Layered Ruthenates	14
1.1.3 Bilayer Ruthenates	16
2 Experimental Techniques	21
2.1 Spectroscopy Techniques	21
2.1.1 XAS	21
2.1.2 RIXS	24
2.1.3 RIXS Instrumentation	26
2.2 Transport Measurements	30
2.2.1 Resistivity and Hall measurements	30
2.2.2 Resistivity and Hall Measurement Set-up	36
2.3 Thermoelectric Studies	38
2.3.1 Thermopower/Seebeck and Nernst	38
2.3.2 Thermoelectric Measurement Set up	41
2.4 Magnetometry	43
2.5 Sample characterisation/Investigating Crystal Structures	46
2.5.1 Xray diffraction: Laue Method	46
2.5.2 Detwinner	48
3 RIXS study on Ca_2RuO_4	51
3.1 Introduction	51
3.2 Methods	56
3.3 Results	57
3.4 Discussion and Analysis	62

3.5	Conclusions	69
4	Magnetotransport study on $\text{Ca}_3\text{Ru}_2\text{O}_7$	71
4.1	Introduction	71
4.2	Methods	73
4.3	Results	73
4.4	Analysis and Modelling	77
4.5	Discussion	82
4.6	Conclusions	86
5	Conclusions	87
A	Thermoelectric Studies in Miscellaneous Systems	89
A.1	PrAlGe	89
A.2	EuCd ₂ As ₂	91
	Acknowledgements	95
	Curriculum Vitae	96
	Bibliography	100

List of Abbreviations

ARPES	angle-resolved photoemission spectroscopy
CDW	charge density wave
CF	crystal field
CMR	colossal magneto resistance
DC	direct current
DOS	density of states
FC	field cooled
FL	Fermi liquid
FS	Fermi surface
HH	Hubbard Hamiltonian
HTSC	High temperature super conductors
JT	Jahn-Teller
MPMS	Magnetic Property Measurement System (by QuantumDesign)
MIT	Metal Insulator Transitions
MR	Magnetoresistance
NFL	non Fermi liquid
PPMS	Physical Property Measurement System (by QuantumDesign)
QCP	quantum critical point
QPT	quantum phase transition
RIXS	Resonant Inelastic Xray Scattering
RP	Ruddleson-Popper
SANS	small angle neutron scattering
SC	superconducting
SE	superexchange
SDW	spin density wave
SOC	spin orbit coupling
SQUID	superconducting quantum interference device
TMO	transition metal oxides
TFY	total fluorescence yield
XAS	Xray Absorption Spectroscopy
ZFC	zero field cooled

List of Figures

1.1	Phase diagrams of a few representative members of the strongly correlated electron family	2
1.2	Crystal structure of Sr_2RuO_4 and La_2CuO_4	3
1.3	Ruddlesden-Popper phases of $(\text{Sr}, \text{Ca})_{n+1}\text{Ru}_n\text{O}_{3n+1}$	4
1.4	Distortions of RuO_6 octahedra	5
1.5	Sketch of the density of states and band fillings for insulator, semiconductor, semimetal, and metal.	5
1.6	A sketch of the terms in the Hubbard Hamiltonian	7
1.7	Schematic illustration of energy levels for a Mott- Hubbard insulator	8
1.8	Sketch of the nondegenerate t_{2g} and e_g levels of the d - orbitals	9
1.9	Summary of the magnetic phases in the $n = 1, 2, 3, \infty$ members of the $(\text{Sr}, \text{Ca})_{n+1}\text{Ru}_n\text{O}_{3n+1}$ series	13
1.10	Comparison of a-axis resistivity of CaRuO_3 and SrRuO_3	14
1.11	Fermi surface of Sr_2RuO_4	15
1.12	Magnetoresistance in $\text{Sr}_3\text{Ru}_2\text{O}_7$	17
1.13	Magnetoresistance and Fermi surface map of $\text{Ca}_3\text{Ru}_2\text{O}_7$	18
2.1	Schematic of incident and transmitted x - ray beam.	22
2.2	Energies of different x - ray absorption edges as a function of atomic number Z	23
2.3	Schematic representation of a Direct RIXS process.	25
2.4	Elementary excitations probed using RIXS	26
2.5	Schematic view of a conventional RIXS detection scheme	27
2.6	Simplified drawing of the SAXES	28
2.7	Example of a Raw RIXS spectrum taken on Ca_2RuO_4	28
2.8	The experimental geometry used in the RIXS measurements	29
2.9	Schematic of geometry of a combined resistivity and Hall measurement set up	34
2.10	Schematic of Four-Probe technique	37
2.11	Example of electrical contacts on a sample of $\text{Ca}_3\text{Ru}_2\text{O}_7$	38
2.12	Schematic depiction of Seebeck and Nernst effect	39

2.13	Schematic illustration of thermoelectric set up used	42
2.14	A simplified schematic setup of a SQUID magnetometer	45
2.15	Pictorial depiction of the derivation of Bragg equation	46
2.16	Measured and simulated Laue pattern of $\text{Ca}_3\text{Ru}_2\text{O}_7$	47
2.17	Images of domain distributions before and after detwinning process	48
3.1	Schematic density of states function for Sr_2RuO_4 and Ca_2RuO_4	52
3.2	Phase diagram of single layered ruthenates	53
3.3	Schematic illustration of the $4d$ electronic states of Ca_2RuO_4	54
3.4	Schematic depiction of RIXS geometry with respect to the crystal lattice of Ca_2RuO_4	57
3.5	XAS and RIXS spectra for LH polarisation at apical and planar sites in Ca_2RuO_4	58
3.6	Elastic line subtracted planar RIXS spectra for LH and LV polarisations	59
3.7	Polarization dependence of the RIXS spectra versus incident photon energy	60
3.8	Zoom in on the low energy excitations A and B of the spectra	61
3.9	The in plane momentum dependence of the RIXS spectra	62
3.10	Comparison of the experimental spectra with the calculated RIXS spectra	64
3.11	Energy spectrum of the $S = 1$ and one doublon $ d^4; n_d = 1\rangle$ at single Ru site	66
3.12	Pictorial depiction of the creation and propogation of spin orbital excitation	68
3.13	RIXS spectrum of Ca_2RuO_4 at the Ru- L_3 edge	69
4.1	Crystal structure of $\text{Ca}_3\text{Ru}_2\text{O}_7$ and Resistivity of CRO327 in the ab plane.	72
4.2	Resistivity and thermopower measurements in $\text{Ca}_3\text{Ru}_2\text{O}_7$	74
4.3	MR and Hall isotherms in $\text{Ca}_3\text{Ru}_2\text{O}_7$	75
4.4	Magnetic susceptibility and colour plot of $\frac{d\rho_{xx}}{dH}$	76
4.5	Low temperature magnetisation, resistivity and Hall isotherms in $\text{Ca}_3\text{Ru}_2\text{O}_7$	77
4.6	Solution to the two-band model	81
4.7	Schematic representation of Fermi surfaces of two carrier systems	83
4.8	Temperature evolution of the parameters α and β	85
A.1	Crystal structure and pictorial representation of location of Weyl nodes in PrAlGe	90

A.2	Hall and Nernst isotherms in PrAlGe	91
A.3	Crystal structure and schematic illustration of Weyl nodes in EuCd ₂ As ₂	92
A.4	Field dependence of topological Hall resistivity and the topological Nernst conductivity isotherms of EuCd ₂ As ₂	93

Chapter 1

Introduction

Technological milestones in the history of human civilization is often marked by the discovery or manipulation of new materials with interesting and useful properties. Condensed matter physics deals with the macroscopic and microscopic physical properties of matter. It is in particular concerned with the "condensed" phases that appear whenever the number of constituents in a system is extremely large and the interactions between the constituents are strong. One of the most striking aspect of physics is the simplicity of its fundamental laws. The primary objective of a contemporary condensed matter physicist is to search for new quantum materials and create concepts capable of understanding various new and exotic phenomena. A traditional reductionist approach to condensed matter physics attributes the macroscopic behaviour of a system to the fundamental laws governing the microscopic behaviour of its constituent elements [1-3]. However the complex behaviours of interacting systems, even within the confines of classical physics, cannot be explained by the straight forward application of a reductionist approach. P.W Anderson in his 1972 seminal article - "More is Different"- wrote that "The ability to reduce everything to simple fundamental laws does not imply the ability to start from those laws and reconstruct the universe" [3].

Transition metal oxide (TMO) systems provide an ideal platform to investigate complex behaviours arising from strong interactions among charges in the d orbitals. These strong correlations give rise to a plethora of interesting properties involving spin, lattice, charge and orbital degrees of freedom. The International Union of Pure and Applied Chemistry (IUPAC) defines transition metal as "an element whose atom has a partially filled d sub-shell, or which can give rise to cations with an incomplete d sub-shell" [4]. In the past few decades d -transition metal oxides have been in the forefront of research and represents a highly active field of condensed matter physics. Due to several competing orders, many of these systems are highly sensitive to perturbations and the strong electron correlations

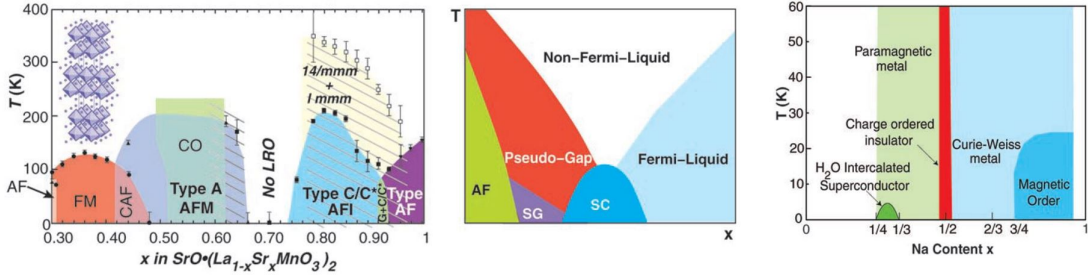


Fig. 1.1 Phase diagrams of a few representative members of the strongly correlated electron family. (a) Temperature versus hole density phase diagram of Manganites. (b) Generic phase diagram of high temperature superconductors. (c) Phase diagram of Co oxides. Taken from Ref. [2]

give rise to a broad range of intriguing phenomena including colossal magnetoresistance, high temperature superconductivity, Mott insulating states etc... [5]. These materials often exhibit complicated phase diagrams with several competing states as shown in Fig.1.1.

The understanding of these materials has challenged a condensed matter physicist's view of solids. Despite decades of research, high temperature superconductivity is still not fully understood. The spontaneous emergence of electronic nanometer-scale structures in transition metal oxides, and the existence of many competing states, are properties often associated with complex matter [2]. In such systems the properties of a few particles are not sufficient to understand the macroscopic picture when these interact and is in contradiction to the traditional reductionist hypothesis accepted by a great majority of physicists. In several transition metal oxides and other materials experimental results have found spatially inhomogeneous dominant states and this is often attributed to competition and coexistence of several physical interactions including spin, charge, lattice, and/or orbital degrees of freedom [2]. In the wake of competing orders and states in these materials, the reductionist approach is gradually superseded by emergent phenomena. The emergent phenomena refers to new properties that arise from the interactions of many particles in a complex system. It lies outside the physics of constituent particles i.e the generation of properties that do not pre-exist in a system's constituents [2, 3, 6]. TMO hence provides a fertile playground to explore emergent phenomena.

The discovery of colossal magnetoresistance (CMR) in manganites (Mn oxides), triggered an explosion of interest in these materials which led to application of fundamental phenomena like CMR in development of new technologies with practical importance [7]. Further, with the discovery of high temperature superconductivity

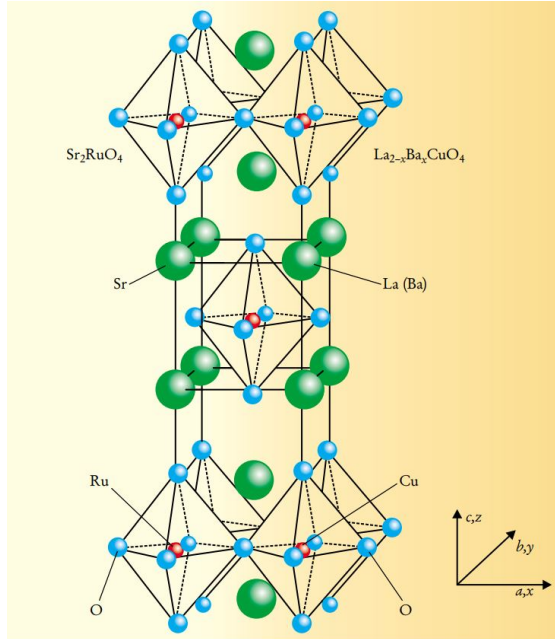


Fig. 1.2 The isostructural Sr_2RuO_4 and La_2CuO_4 has markedly different electronic properties - Sr_2RuO_4 is strongly metallic and a superconductor at low temperature, whereas La_2CuO_4 is an antiferromagnetic insulator. Taken from Ref. [9]

ity (HTSC) in LBCO ($\text{La}_{2-x}\text{Ba}_x\text{CuO}_4$) in 1986 by Alex Mueller *et al.* [8], with a record transition temperature of 30 K surpassing the expected transition temperatures of conventional superconductors of the time, resulted in an influx of new measurements and subsequent application of such fundamental phenomena in commercial developments. These exotic phenomena like CMR where a small change in magnetic field results in enormous changes in resistivity, high temperature superconductivity etc... are properties often attributed to strong electron-electron (el-el) correlations in these materials.

Apriori, due to the highly extended nature of the $4d$ orbitals compared to their $3d$ counterparts, $4d$ TMO materials were thought to have less significant el-el correlations and hence relatively less attention was paid to this class of materials. However, with the discovery of exotic superconducting pairing in a compound without copper - Sr_2RuO_4 - a layered perovskite material isostructural with $\text{La}_{2-x}\text{Ba}_x\text{CuO}_4$ (see Fig 1.2) [9] in 1994 by Maeno *et al.* [10], sparked intense interest into research of ruthenate compounds and has since triggered a burgeoning body of research work on this and related ruthenate compounds.

The term ruthenate denotes a large group of oxide materials based on ruthenium. Our discussion in this chapter and thesis would focus primarily on the Rudleson Popper (RP) series of ruthenates with the general formula $(\text{Sr}/\text{Ca})_{n+1}\text{Ru}_n\text{O}_{3n+1}$. Here ($n = 1, 2, \dots, \infty$), denotes the number of connected layers of vertex sharing

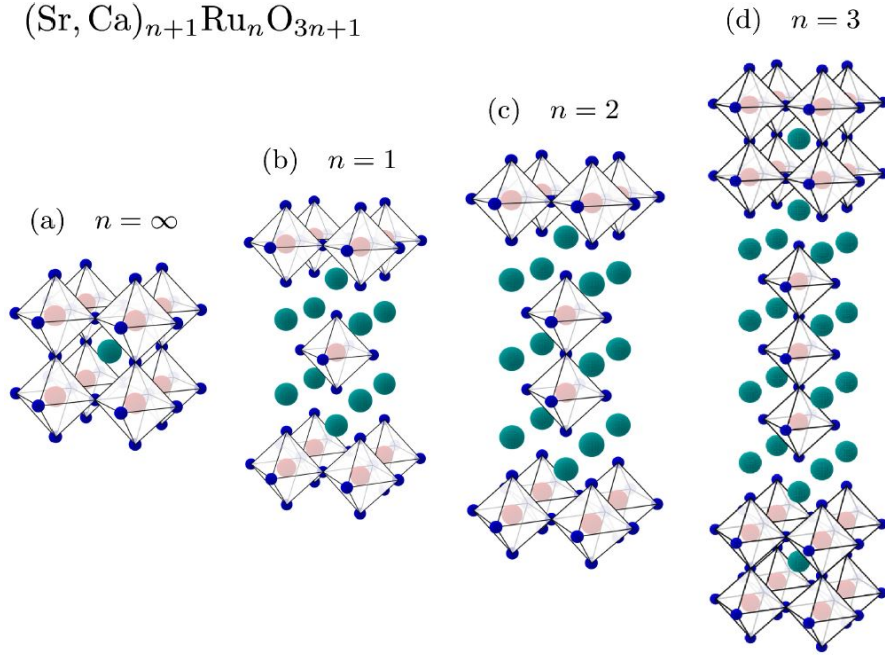


Fig. 1.3 Ruddlesden-Popper phases of $(\text{Sr}, \text{Ca})_{n+1}\text{Ru}_n\text{O}_{3n+1}$ for $n = \infty, 1, 2, 3$. The Ru atoms are shown as pink spheres at the center of the oxygen octahedra. Oxygen atoms shown in blue and Sr or Ca atoms are located between the layers. Taken from Ref. [11]

RuO_6 octahedra as shown in Fig 1.3 (with the Ru atoms located at the center of each octahedron). Ruthenates constitute the archetype of systems which shows a strong dependence of their physical properties on the number of layers. These materials exhibit a variety of unusual phenomena like metal-insulator transitions [12], unconventional superconductivity [10], possible metamagnetic texture in anti ferromagnetic state [13], existence of a Dirac semimetal state [14], colossal magneto resistance [15] to name a few. In the RP series, Ca compounds are more structurally distorted than their Sr counterparts due to the smaller ionic radius of Ca ions causing a profound impact on the magnetic and transport properties of the compounds [5]. While no rotation or tilt of RuO_6 has been reported for the Sr compounds, all Ca-compounds deviate from their Sr counterparts by a rotation and or tilt of the RuO_6 octahedra as shown in Fig 1.4. The Ca-compounds are severely distorted with the octahedra significantly tilted along an axis in the RuO_2 planes and rotated along the crystallographic c -axis direction leading to a lowered structural symmetry and unequal Ru-O bond lengths [5].

Metal Insulator Transitions

The discovery of high temperature superconductivity in cuprates and subsequent discovery of superconductivity in Sr_2RuO_4 , triggered a strong interest in

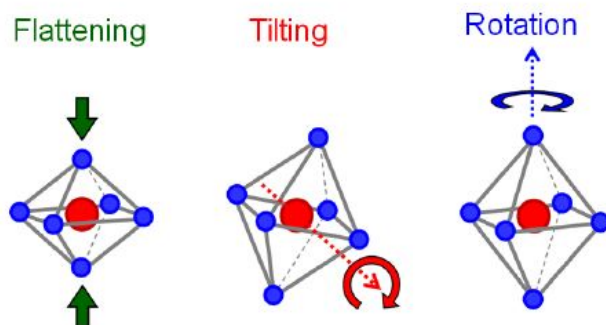


Fig. 1.4 Pictorial representation of the various distortions of RuO₆ octahedra. In Ca₂RuO₄, RuO₆ octahedra exhibit three lattice distortions - the flattening along *c* axis, tilting around an axis in the RuO₂ planes plus a rotation along the crystallographic *c* axis. Taken from Ref. [16]

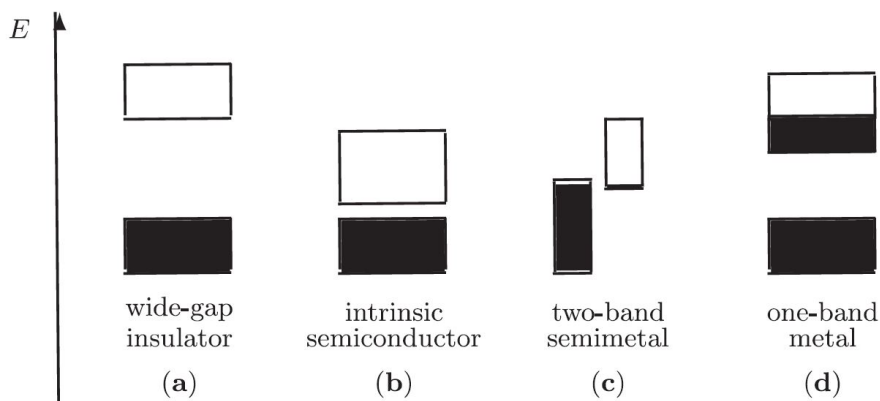


Fig. 1.5 Sketch of the density of states and band fillings for insulator, semiconductor, semimetal, and metal according to band theory; occupied energy levels at zero temperature are filled in. Taken from Ref. [17]

the physics of TMO and renewed focus on Metal-insulator transitions (MIT). MIT are observed in many condensed matter systems and are accompanied by huge resistivity changes. Here we discuss about Mott type transitions that are driven by correlation effects associated with the electron-electron interaction [7].

Band structure theory provides a very simple and successful understanding for the existence of metals and insulators. The energy bands are separated due to the influence of the periodic potential resulting in energy gaps between the bands - If the chemical potential lies between two such bands all bands are either completely filled (“valence bands”) or empty (“conduction bands”) as shown in Fig 1.5 [17].

However in 1937, in a paper by Boer and Verwey [18], attention was drawn to 3*d* TMO with partially filled *d* - electron bands which were expected to be metals but were found to be insulating. In the same year, N.F Mott along with Peirls

showed that this atypical insulating phase is the result of strong electron electron interactions in these materials and provided the theoretical framework for the study of these materials called the Mott insulators [19]. In such materials, due to the strong on-site electron correlation given by the Coulomb interaction U , the original band would be split into two bands with energy gap of U , and thus the system would be an insulator. The Mott-Hubbard model is used as an archetypal model for theoretical understanding of the electron-electron correlation effects on the metal insulator transition. The Hubbard Hamiltonian uses the simplified approach where the atoms in a solid correspond to a collection of sites each with a single level. Pauli's Principle introduces a constraint of four configurations- empty, a single up fermion, a single down fermion, or double occupation by a pair of up and down Fermions. In a solid electrons can move around and the electrons interact via a screened Coulomb interaction. This interaction strength is maximum U if the site is doubly occupied and zero if the site has only single fermion/ is empty. The simple model Hamiltonian does not take into account the interaction between the Fermions at different sites, however this can be corrected using the extended Hubbard Hamiltonian. The kinetic energy expression in the Hamiltonian describes the destruction of a fermion on one site and creation at another. This process- termed 'hopping' is governed by energy scale t - determined by the overlap of two wavefunctions on the pair of atoms. In the simplest case, hopping is considered only between the nearest atoms in the lattice [20]. Using the reasoning above, the expression for the Hubbard Hamiltonian is given as follows

$$\mathcal{H} = -t \sum_{\langle \mathbf{j}, \mathbf{i} \rangle \sigma} (C_{\mathbf{j}\sigma}^\dagger C_{\mathbf{i}\sigma} + C_{\mathbf{i}\sigma}^\dagger C_{\mathbf{j}\sigma}) + U \sum_{\mathbf{j}} n_{\mathbf{j}\uparrow} n_{\mathbf{j}\downarrow} - \mu \sum_{\mathbf{j}} (n_{\mathbf{j}\uparrow} + n_{\mathbf{j}\downarrow}) \quad (1.1)$$

The first term denotes the kinetic energy which describes the annihilation of fermion of spin σ at site \mathbf{i} and its creation at \mathbf{j} or vice versa. $\langle \mathbf{j}, \mathbf{i} \rangle$ shows that the hopping is allowed between adjacent sites and represent the itinerant nature of Fermions. The second term is the Coulomb interaction energy which represents the localised tendency of the Fermions and the third term is the chemical potential that controls filling. For the purpose of this discussion, we focus on the situation with there is one fermion per site - 'half-filling' state- as it exhibits a lot of interesting phenomena (Mott insulating behavior, anti-ferromagnetic order, etc... Fig 1.6 shows a schematic illustration of the Hubbard Hamiltonian. Hence, the parameters that determine the properties described by the Hubbard Hamiltonian is given by U - the on-site Coulomb interaction, t - bandwidth of the electrons determined by the hopping parameter 't', temperature and the doping/number of electrons.

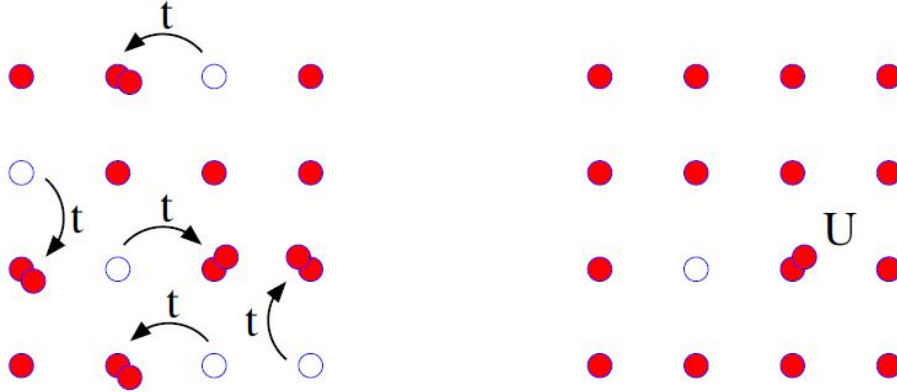


Fig. 1.6 A sketch of the terms in the Hubbard Hamiltonian. t is the hopping parameter and denotes the kinetic energy and U denotes the on-site Coulomb repulsion. Taken from Ref. [20]

The experimental study of the MIT in correlated metals has been most thorough and systematic in d -electron systems, namely, the transition metal compounds [21]. In particular, ruthenates have been shown to be a fertile ground for studying MIT by band width control [22, 23]. In the most simple description of the Mott-Hubbard model, the metal insulator transition is controlled by the magnitude of the the Coulomb interaction U and the electron bandwidth W . The extended d -shell of the $4d$ TMO's result in weaker intra atomic Coulomb interaction and this tend to drive the $4d$ TMO's towards metallic states with $U/W < 1$. A splitting between the lower and upper Hubbard bands increases as U/W increases and for a half-filled band MIT occurs at $U/W \approx 1$, where a Mott-Hubbard gap opens. See Fig 1.7

There are two routes towards Mott transition - control of electron filling/carrier doping and bandwidth control. The former refers to doping carriers into the Mott insulating state with integer filling resulting in a metallic state. The latter refers to the situation where phase transition is facilitated by increasing the ratio of bandwidth to Coulomb interaction thereby enhancing quantum fluctuations and stabilising metallic state. Among the various TMO systems where the MIT are driven by bandwidth control, the layered ruthenates $\text{Ca}_{n+1}\text{Ru}_n\text{O}_{3n+1}$ provide unique avenues for controlling MIT via dimensionality control [5, 22]. The studies by Cao *et al.* showed that the MIT temperatures in the Ca compounds gets suppressed with increasing dimensionality ($T_{MI} = 356$ K) for $n = 1$ to ($T_{MI} = 48$ K) for $n = 2$ to ($T_{MI} = 0$ K) for $n = \infty$ [5]. The larger radial extent of the d shells of transition metal cations in $4d$ - TMO in comparison to their $3d$ counterparts greatly enhances the interaction between electron and lattice resulting in d - p hybridisation in oxides which could lead to structural phase transitions. The strong distortions

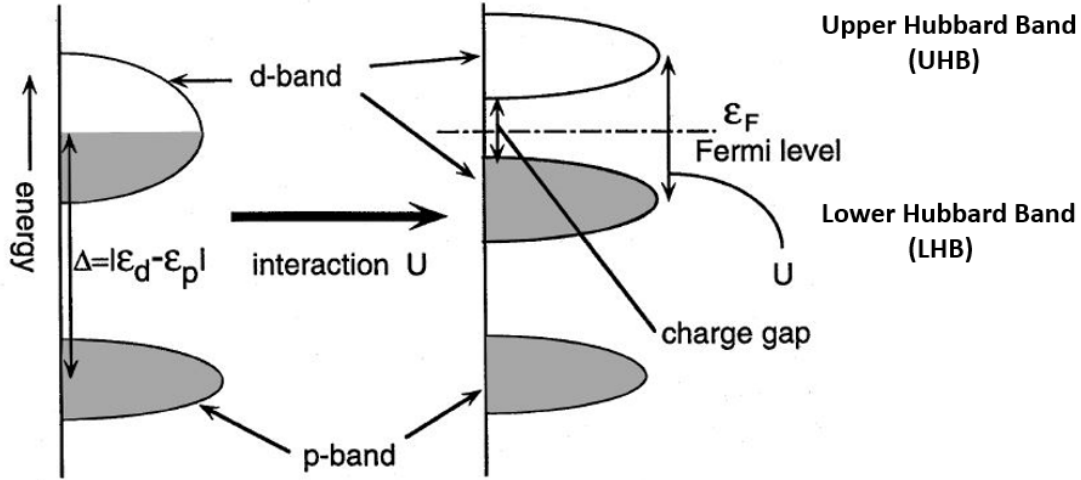


Fig. 1.7 Schematic illustration of energy levels for a Mott- Hubbard insulator where U , W and Δ represents the on-site Coulomb interaction, Bandwidth, and charge transfer energy respectively. Double occupancy costs an energy U resulting in splitting of the energy band into Upper and Lower Hubbard Bands. For small intersite interaction i.e. $U > W$, Coulomb repulsion drives half-filled band to insulating with lower band fully filled and upper band empty and opens up a Mott-Hubbard gap - U , when kinetic energy dominates i.e. $W > U$, metal - insulator transition is facilitated. Taken from Ref. [21]

of the RuO_6 octahedra in these systems however competes with this and causes a weakening of the overlap between the oxygen p orbitals and the t_{2g} states of the transition metal cation- Ru- which in turn affects the conduction bandwidth W . The increase in dimensionality increases the d - p hybridisation and bandwidth W correspondingly increases. However as dimensionality is increased, the electronic structure is less sensitive to distortions. For higher dimensionality say, $n = \infty$, CaRuO_3 the system is metallic albeit severely distorted. Hence in these systems there exist competition between the Coulomb interaction and bandwidth and small perturbations, such as pressure, change in doping, alteration in crystal structure etc... can drive the system across the metal-insulator boundary and cause significant changes in the physical properties of the system [5, 24]. Layered ruthenium oxides $(\text{Sr}/\text{Ca})_{n+1}\text{Ru}_n\text{O}_{3n+1}$ being the naturally engineered layered systems thus provides a fertile ground to study the MIT. The bandwidth W of this system can be well tuned by varying the dimensionality and the Sr/Ca ratio, giving rise to the different Mott parameter U/W [25].

Crystal Field Effect

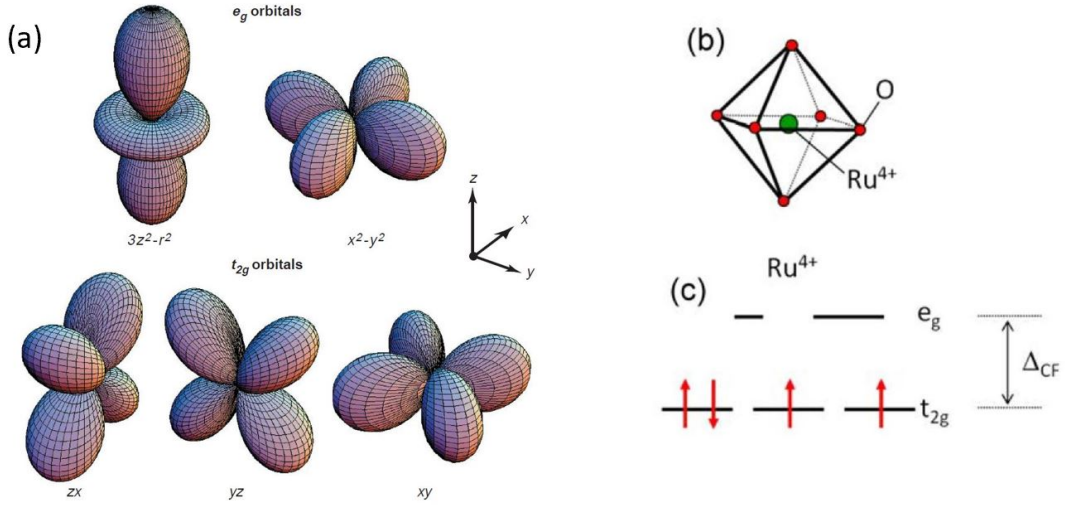


Fig. 1.8 (a) The five fold degeneracy of the d orbitals is lifted in an octahedra crystal field, with two e_g orbitals ($x^2 - y^2$ and $3z^2 - r^2$) higher in energy than the three t_{2g} orbitals (xy , yz , and zx). (b) RuO_6 octahedra. (c) Schematic depiction of the splitting of energy levels. As the crystal field splitting is higher than Hund's energy term, the electrons occupy the lower t_{2g} states leaving the e_g states empty. Taken from Ref. [7]. Taken from Ref. [26]

The electronic state of ruthenates is determined by the formal oxidation state of Ru^{4+} ions i.e. every Ru ion has four electrons in the $4d$ orbital. In a free Ru ion angular quantum number $l = 2$ and magnetic quantum number $m_l = -2, -1, 0, +1, +2$, defines the five d - orbitals available that are degenerate. As shown in Figs. 1.4 and 1.8, the transition metal (Ru) within an oxygen octahedron is surrounded by six oxygen atoms, whose electrostatic field (ligand field) lifts the degeneracy of the d -states of the Ru-ion.

The crystal field effect originates from the electronic repulsion between the negatively charged electrons of the d -orbitals of the transition metal cations and the p -orbitals from oxygen ligands. In the presence of the cubic crystal field, the above mention degeneracy is lifted. The electrons in a d -orbital that is closer to the oxygen ligands experience larger repulsion due to larger overlap between the p and d orbitals and hence have higher energy than those further away. The d -orbitals thus split in energy with three fold degenerate t_{2g} orbitals (consisting of $d_{xy}/d_{xz}/d_{yz}$ states) and two fold degenerate e_g orbitals (comprising $d_{x^2-y^2}$ and $d_{3z^2-r^2}$ states) as shown in Fig 1.8.

The energy difference between the lower lying t_{2g} states and the upper e_g states have been determined from band structure calculations to be around $\Delta = 10D_q = 4$

eV in ruthenates [7]. Due to the deformation of the Ru octahedra, the crystal field is no longer cubic but has a tetragonal or even lower symmetry resulting in a further lifting of degeneracy within the t_{2g} and e_g states with the tetragonal field splitting within the t_{2g} levels of the order of 100 meV. Furthermore, the orthorhombic distortion of the RuO_6 octahedra, reduces the crystal symmetry and adds an additional small splitting of the xz and yz orbitals. However, the orthorhombic splitting is assumed to be relatively small, so the xz and yz states are often treated as degenerate [27–29]. In the RP series of ruthenates, the larger crystal field effect (~ 4 eV) surpasses the Hund’s coupling (~ 1 eV). Hund’s Rule dictates the filling of electrons in such a way that total spin at Ru- site is maximised. Thus, the ($E_H < \Delta_{CF}$) makes it favorable for the electrons to occupy the lower t_{2g} states with two electrons of opposite spin occupying the same orbital than overcoming the $e_g - t_{2g}$ splitting Δ . This results in a low spin state with a total spin of $S = 1$ with all four electrons occupying the t_{2g} -orbitals, leaving the e_g - states empty. When there is an orbital degeneracy in a system resulting from crystal field splitting, a Jahn Teller (JT) local site distortion mechanism removes this degeneracy in order to stabilise the electronic configuration. However in the crystal, this local site distortion is opposed by forces that favors higher symmetry. Hence these type of distortions only occur at low enough temperatures where this effect is stronger such that the cooperative JT distortions can reduce the opposing elastic forces. When the orbital angular momentum is not quenched, long-range magnetic order can give rise to a cooperative JT distortion through the spin–orbit coupling $\lambda \mathbf{L} \cdot \mathbf{S}$ [30]. These cooperative JT distortions leads to an additional distortion that is superimposed on any distortion introduced by cooperative rotations of the MO_6 octahedra, where M is the transition metal ion. The orbital angular momentum is not quenched in the Ru^{4+} ions for uncompressed cubic RuO_6 octahedral configuration which leads to a competition between the c -axis compressive and expansive distortions of the RuO_6 octahedra that tends to maximise and quench the orbital momentum respectively [7]. A combined XAS and spin resolved ARPES study Mizokawa *et al.* in the ruthenate compound Ca_2RuO_4 demonstrated the interplay between spin and orbital degrees of freedom and showed the presence of strong spin orbit coupling that induces the substantial orbital angular momentum in the Ru $4d$ t_{2g} band [31].

Spin Orbit Coupling

Spin–Orbit coupling (SOC) plays a very important role in solids. The influence of SOC is determined by the ratio of the coupling (and the splitting produced by it) to the crystal field splitting. However in most of the $4d$ compounds, the strength of the crystal field splitting that causes the split between t_{2g} and e_g levels

is stronger than the spin orbit coupling - λ [32]. Although the cubic crystal field splitting is bigger than λ , the effect of Jahn Teller distortions discussed earlier, could induce further splitting in the d - levels which are comparable to splitting due to spin orbit coupling. Due to quenching of angular momentum in e_g states the effect of SO coupling is absent in these states in first order [32]. However in the half filled t_{2g} states, SO interaction plays an important role. The net orbital moment is non zero in the t_{2g} states resulting in SO coupling leading to splitting of these levels. In the low spin more than half filled case of $Ru^{4+}(d^4)$, a rather non trivial situation can exist. For such an ion the possible multiplets formed by SO coupling will have total angular momentum \mathbf{J} given by $\mathbf{J} = 0, 1, 2$ which implies that the ground state is a nonmagnetic singlet. However this is in direct contradiction to experimental results where most materials containing Ru^{4+} are magnetic [33]. This is because in such materials the crystal field is lower in symmetry than the ideal cubic field which induces a further splitting of the t_{2g} states. In the presence of a tetragonal distortion resulting in the contraction of RuO_6 octahedra, the energy levels split with d_{xy} as the lowest lying site that is doubly occupied and the higher lying states of $d_{xz/yz}$ would be singly occupied resulting in the total angular momentum to be zero. This state would thus have $\mathbf{S} = 1$ and would be magnetic if the tetragonal field splitting is larger than the SO coupling. Magnetically ordered states can also be realised in concentrated systems with strong exchange interactions between neighbouring Ru-ions and this effect is larger than the SO coupling. This is what happens in the case of Ca_2RuO_4 , where the superexchange (SE) interaction occurs through band overlap of the oxygen and Ru atoms. The strength of the interaction is set by $J_{ex} = 4t^2/U$ where the hopping term t determine the band overlap and Coulomb term U suppresses the interaction of the neighbouring ions [34]. In Mott insulators like Ca_2RuO_4 with van Vleck type TM ions- Ru^{4+} , a low spin state $\mathbf{S} = 1$ is realised, as discussed earlier, due to moderate Hund's coupling and moderately strong SOC resulting in splitting of λ between $J = 0$ singlet and $J = 1$ triplet state. The singlet-triplet splitting λ in these materials are comparable to the SE J_{ex} energy terms (of the order of 100meV) resulting in conventional Bose condensation of van Vleck excitons into a magnetic state and is similar to van-Vleck-type mechanism, where a non-magnetic ground state becomes magnetic due to an admixture of excited states in an external magnetic field [34]. The studies by Khailullin [35] showed that in perovskites this could possibly results in the emergence of excitonic magnetic order, magnons, and the so called amplitude ('Higgs') modes. Recent inelastic x - ray scattering studies and Raman scattering studies have shown the existence of Higgs mode in Ca_2RuO_4 thus providing considerable evidence for an excitonic magnetism in Ca_2RuO_4 [36, 37]. In this thesis, using RIXS at the oxygen K -edge

we provide experimental evidence for a series of excitations at energies 0.08 eV, 0.4 eV, 1.3 eV and 2.2 eV. Solving the Hamiltonian in the spin triplet subspace showed that the lowest energy levels are composed of 9 spin orbit entangled states grouped into two distinct blocks dubbed α and β (Refer Chapter 3 for more details). In this context, in the d^4 subspace with one doubly occupied orbital, singlet/triplet refers to the spin singlet/spin triplet states i.e the electrons in the doubly occupied orbital form a spin singlet while the other two electrons can be in a spin singlet or triplet state. The low energy excitation at 0.08 eV corresponds to transitions within the α manifold at Ru- site. The 0.4 eV excitation corresponds to transitions between the α and β sectors driven by spin orbit coupling and crystal field effects. The higher energy excitations are the Hund's driven singlet to triplet transitions at single Ru or two neighbouring Ru sites.

1.1 General overview of Layered Ruthenates

Fig 1.9 taken from Ref. [5] summarises the manifold of magnetic, structural and conductive phases observed in $(\text{Ca, Sr})_{n+1}\text{Ru}_n\text{O}_{3n+1}$.

1.1.1 Infinite Layered compounds

Isostructural and isoelectronic CaRuO_3 and SrRuO_3 are $n = \infty$ members (n = number of Ru–O layers/unit cell) of the Ruddlesden–Popper (RP) series. Even-though both compounds are orthorhombic, SrRuO_3 has a less distorted perovskite structure compared to CaRuO_3 . As discussed before, due to the larger crystal field effect in these materials, Hund's rule partially breaks down resulting in a low spin state with $S = 1$. Due to the smaller ionic size of Ca^{2+} in comparison to Sr^{2+} the rotation of RuO_6 octahedra is twice as large in CaRuO_3 than in its Sr counterpart, making CaRuO_3 less favorable for ferromagnetism due to a weaker exchange interaction J [38].

Although the isostructural SrRuO_3 is extensively studied and has a ferromagnetic ground state with a Curie temperature of $T_c = 160$ K, the nature of the ground state properties in CaRuO_3 still remains enigmatic with reports suggesting contrasting scenarios that the system is a strongly enhanced paramagnet or an ordered material with short range magnetic interactions-possibly spin glass like behaviour [39–42]. CaRuO_3 shows deviation from FL behaviour where a $T^{1.5}$ power law dependence on resistivity was observed in the $1.7 \text{ K} < T < 24 \text{ K}$ temperature range [38]. A comprehensive magnetic, calorimetric and electric transport property measurements on CaRuO_3 by Cao *et al.* [38] showed a divergent specific heat [$C/T \sim -\log(T)$] followed by a Schottky anomaly with decreasing T , and unusual

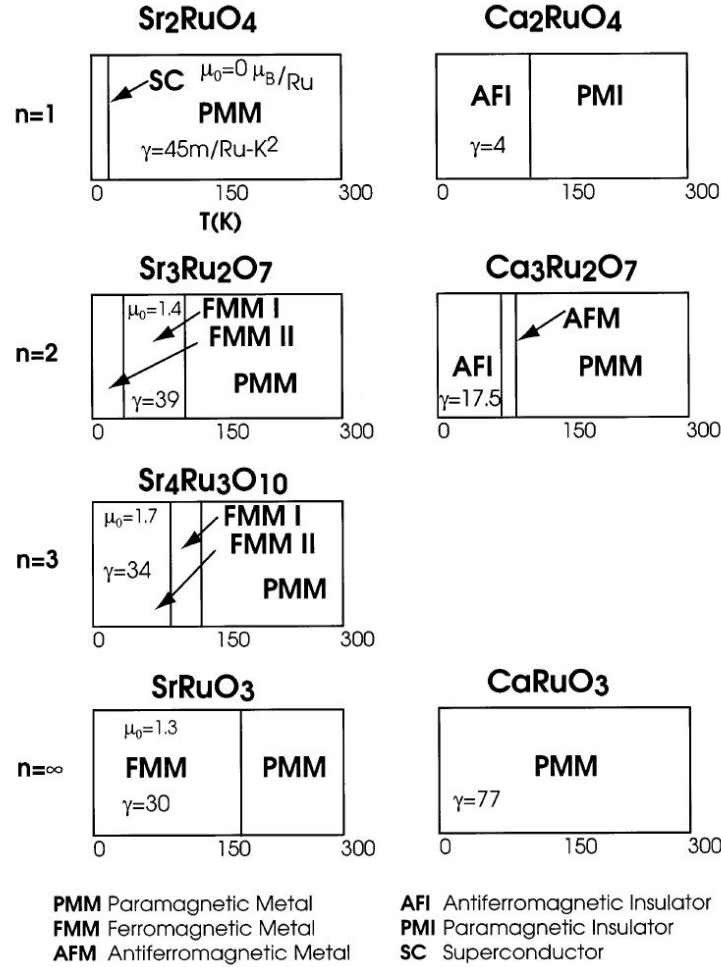


Fig. 1.9 A general phase diagram of $n = 1, 2, 3, \infty$ members of the $(\text{Sr}, \text{Ca})_{n+1}\text{Ru}_n\text{O}_{3n+1}$ series summarising the wide and complex array of magnetic phases. Taken from Ref. [5]

power law in resistivity and diverging magnetic susceptibility at low temperatures - thus ascribing the non Fermi liquid behaviour of the system to its proximity to a magnetic instability, making it an outstanding model system for studies of quantum criticality in the ruthenates [38].

SrRuO_3 is ferromagnetic below the transition temperature $T_c = 160$ K with magnetic moment of $1.4\mu_B$ at $T = 0$ K, rare for a $4d$ transition metal oxide [43]. SrRuO_3 is a Fermi liquid at low temperatures confirmed by T^2 scattering rates and Shubnikov oscillation measurements [44]. At higher temperatures, infrared conductivity measurements have shown an anomalous frequency dependence, leading to the proposal of a non-Fermi liquid metallic state [45]. High resolution ARPES measurements of the Fermi surface in the ferromagnetic (FM) state have shown the presence of Landau quasiparticles [46]. The presence of a kink in the quasipar-

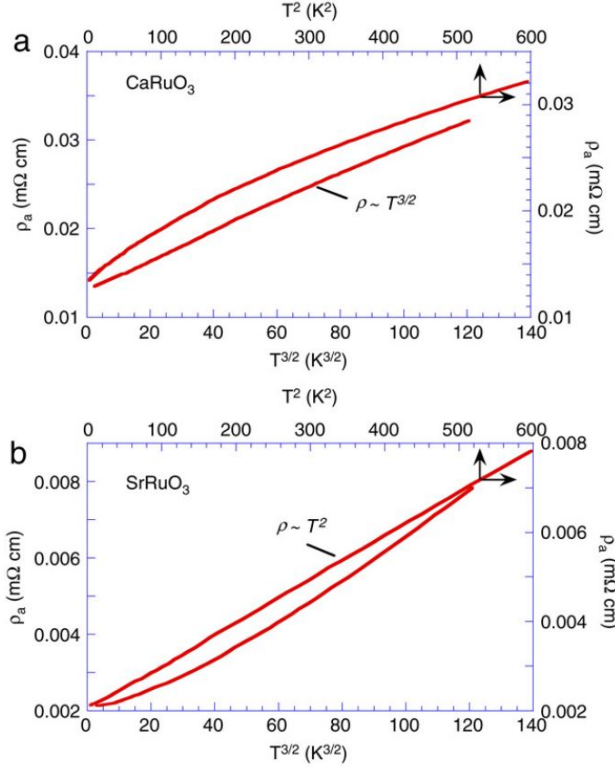


Fig. 1.10 A comparison of a-axis resistivity ρ_a of CaRuO_3 and SrRuO_3 as a function of $T^{3/2}$ and T^2 . Taken from Ref. [38]

ticle dispersion implied the role of strong electron-boson interactions that influence the effective electron masses thus explaining the large effective masses observed by transport and thermodynamic measurements in SrRuO_3 . Experimental results with first principle calculations suggested the existence of magnetic monopoles in this material [47]. Studies by Verissimo *et al.* supported the existence of spin polarised 2D electron gas in $(\text{SrTiO}_3)_5/(\text{SrRuO}_3)_1$ superlattices. [48] SrRuO_3 is a quite sought after material in oxide electronics due to its metallicity, magnetic properties and lattice match to other oxides [46]. Despite extensive studies, a comprehensive understanding of CaRuO_3 and SrRuO_3 is still lacking and challenges remain [49].

1.1.2 Single Layered Ruthenates

Single layered ruthenates Ca_2RuO_4 and Sr_2RuO_4 display a wealth of intriguing properties like Mott metal insulator transition [50, 51], unconventional superconductivity [9, 10], Hund's coupling physics [52] to name a few. As discussed before, electronically these ruthenates are characterized by the $4d-t_{2g}^4$ configuration. Due to the layered structure, the xz and yz bands are almost one dimensional, while

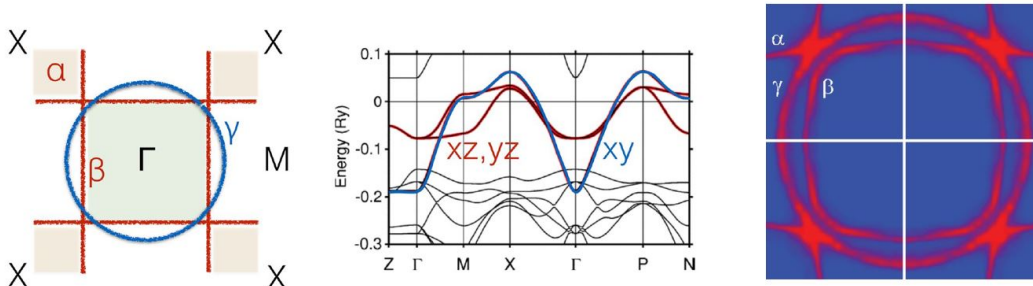


Fig. 1.11 (a) Schematic illustration of the Fermi surface of Sr_2RuO_4 . (b) Calculated LDA band structure. (c) Fermi surface measured with ARPES. Taken from References [53, 57, 59]

the xy band is two dimensional like. As a result, the xy bandwidth W_{xy} is about double the bandwidth of the xz/yz bands and these layered ruthenates are considered as strongly correlated systems [53].

Sr_2RuO_4 has tetragonal symmetry, is metallic below $T_{FL} = 30$ K and undergoes superconducting transition at 1.5 K [10]. The nature of the superconducting state is still a highly debated topic- it was initially proposed to be spin triplet type [54] - chiral p - wave [55] - however this interpretation does not perfectly explain all experiments so far [53]. The general consensus is that the enhancement of spin-orbit coupling (SOC) at the Fermi surface (FS) plays an important role in the superconductivity of Sr_2RuO_4 [53, 56]. The FS of Sr_2RuO_4 has been extensively studied using ARPES [57] and deHaas van Alphen measurements [58]. The FS comprises of two sheets dubbed α and β arising from the one dimensional xz/yz bands and sheet named γ from the 2D like xy band [53]. See Fig 1.11

With the isovalent substitution of Sr with Ca the symmetry of the crystal structure is lowered from the tetragonal $I4/mmm$ to the orthorhombic $Pbca$ space group. This material is strongly distorted with a combined rotation, and tilt of the RuO_6 octahedra. The stoichiometric compound Ca_2RuO_4 is a Mott insulator at low temperature and it turns metallic above 360 K [7]. Ca_2RuO_4 undergo AFM ordering below the Néel temperature $T_N = 110$ K. Raman and Inelastic Neutron scattering experiments in the insulating phase revealed anti ferromagnetic order with an unconventional excitation spectrum composed of soft longitudinal Higgs mode and transverse magnons with large gap [36, 37, 53, 60, 61]. All these phenomena raise new questions on the electronic properties of ruthenates.

Although the mechanism behind rendering the $2/3$ filled t_{2g} bands insulating has been credited to Mott type physics, the nature of Mott transition in Ca_2RuO_4 has been a subject of debate for decades. Different scenarios have been proposed for the orbital occupancy and no consensus has been reached on this. Here, we present

XAS and RIXS results in conjunction with theoretical calculations and show that Ca_2RuO_4 is a band Mott insulator characterised by orbitally selective coexistence of band and Mott gap. The crystal field drives the d_{xy} band insulating while mott physics happen in the $d_{xz/yz}$ bands. In this section, Sr_2RuO_4 is discussed primarily; for a detailed description of the various properties of Ca_2RuO_4 refer Section 3.1

1.1.3 Bilayer Ruthenates

The bilayer ruthenate metal $\text{Sr}_3\text{Ru}_2\text{O}_7$ belongs to an $I4/mmm$ space group and exhibits behavior consistent with proximity to a metamagnetic (i.e., magnetic field-tuned) quantum critical point. This system thus serve as a prime candidate to study quantum critical end point (QCP) and provide new vistas to learn more about experimental precision of field-tuned studies [62]. Metamagnetism is defined as a very rapid increase of magnetization, M , over a narrow region of applied field, H . Although, metamagnetism is the result of “spin-flop” or “spin-flip” spin reorientation processes in localized systems, it may also occur in itinerant systems, even those which are nonmagnetic at $H = 0$ [62]. Studies done by Grigera *et al.* showed the presence of metamagnetism in $\text{Sr}_3\text{Ru}_2\text{O}_7$ for magnetic fields oriented both in the ab plane and along the c axis [62]. For $B \parallel ab$, the transition occurs between 5 and 6 T, and for $B \parallel c$, transition occurs at approximately 7.8 T. The resistivity data is analysed with the general expression $\rho(T) = \rho_{res} + AT^\alpha$, where ρ_{res} is the resistivity due to elastic scattering at $T = 0$ and A is a temperature - independent coefficient related to a quasi - particle effective mass, and the exponent α contains valuable information about the nature of the metallic state-with Fermi liquid states characterised by the parameter value $\alpha = 2$ and the non Fermi liquids by $\alpha < 2$ [62]. Fig 1.12 shows the evolution of the α parameter. In the field-temperature contour plot, $\alpha = 2$ at low fields, reaches a value close to 1 near the metamagnetic field, and then grows again as the field is increased further [62]. Neutron Scattering experiments by Lester *et al.* [63] have shown that the application of field can induce spin density wave (SDW) order in this system which correlates strongly with the electronic nematic properties of the compound. The SDW order thus provides a natural order parameter to associate with the quantum criticality and provides a basis for understanding the associated physical properties [63].

$\text{Ca}_3\text{Ru}_2\text{O}_7$ has a non centrosymmetric crystal structure belonging to the space group $Bb2_1m$ (#36) and is one of the most versatile systems exhibiting a vast array of correlated phases of TMO. It exhibits high sensitivity to impurities exemplified by Mott-type transition with even 0.3% Ti - doping [64], a metamagnetic transition, colossal magnetoresistance and quantum oscillations in the resistivity [65, 66]. A detailed description of the electronic and physical properties of

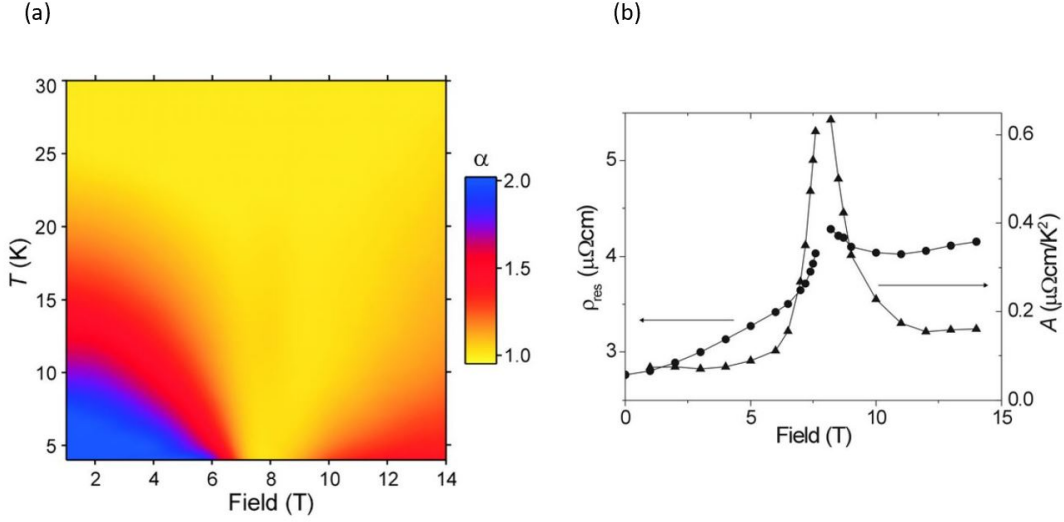


Fig. 1.12 (a) A color plot that shows the evolution of the exponent α from the expression $\rho(T) = \rho_{res} + AT^\alpha$ as a function of field and temperature in $\text{Sr}_3\text{Ru}_2\text{O}_7$. A quadratic T dependence seen at low fields evident from the value of α points towards the expected FL behaviour below 10 K. Near the metamagnetic transition at 7.8 T, a power close to 1 is seen that persists down to 4.5 K, and rises again with increase in field. (b) Residual resistivity and temperature-scaling factor A diverge at 7.9 T metamagnetic field. Taken from Ref. [62, 63]

$\text{Ca}_3\text{Ru}_2\text{O}_7$ is discussed in Section 4.1.

At high temperature $\text{Ca}_3\text{Ru}_2\text{O}_7$ is a paramagnetic metal (PM-M) and undergoes AFM ordering below $T_N = 56$ K. In this state, the Ru^{4+} spins are aligned ferromagnetically within each bilayer but the net moment cancels due to the AFM stacking of the bilayers. At $T_{MIT} = 48$ K the system goes through a metal to semimetal like transition and is associated with changes in lattice parameters. Simultaneously, an iso-structural transition leads to a compression of the unit cell along the c -direction [67].

In the semimetallic magnetic phase there have been observations of quantum oscillations indicating the presence of small electron pockets in the Fermi surface, which were subsequently found by ARPES measurements [15, 66, 68, 69]. ARPES measurements by Horio *et al.* showed a rotation symmetry broken Dirac semimetal state in $\text{Ca}_3\text{Ru}_2\text{O}_7$ which emerges in a two stage FS reconstruction. The Fermi surface was observed to be anisotropic, with small electron like pockets formed by massive Dirac Fermions in the short-axis orthorhombic zone boundary and along the long axis hole like Dirac cone resulted in a boomerang shaped Fermi surface [14]. See Fig. 1.13 Panel (b).

Recent small angle neutron scattering (SANS) studies on $\text{Ca}_3\text{Ru}_2\text{O}_7$ showed the

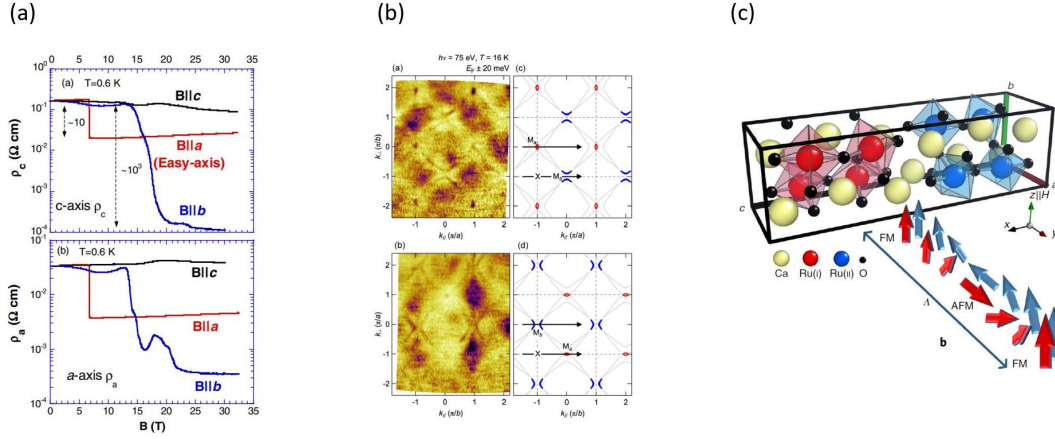


Fig. 1.13 $\text{Ca}_3\text{Ru}_2\text{O}_7$: (a) Field dependence of resistivity for applied current along a and c-axis with red, blue and black plots showing the orientation of the magnetic field applied (parallel to a, b and c-axis respectively) at 0.6K. (b) FS maps obtained at 16K that shows a small electron like Fermi pocket around the short-axis orthorhombic zone boundary point and boomerang-like features near long axis orthorhombic zone boundary point. (c) Pictorial illustration of the propagating 1D- metamagnetic texture along a-axis in $\text{Ca}_3\text{Ru}_2\text{O}_7$ with field along b-axis resulting in the oscillation of the spin configuration from FM to AFM and back to FM. Taken from References. [13–15]

presence of a spirally modulated magnetic order- termed metamagnetic texture- a field driven spin state with coexisting spin orders of different symmetries-AFM and FM. [13] Under applied magnetic field the system also showed colossal magnetoresistance (CMR) that occurs upon suppression of the spin-polarized FM state which was achieved by applying a magnetic field perpendicular to the easy magnetization axis [15, 70]. Transport and thermodynamic experiments by Cao *et al.* on this system at high fields revealed highly anisotropic behaviour that depends strongly on the magnitude and the direction of the applied magnetic field. Such an anisotropic coupling is attributed to the interplay between the lattice, spin and orbital degrees of freedom [15].

For an applied field $B \parallel a$ -axis a fully polarised spin state via metamagnetic transition was observed at 6T, while $B \parallel c$ -axis resulted in colossal magnetoresistance and for $B \parallel b$ -axis quantum oscillations could be observed. [15] Furthermore, Density functional calculations of the fermiology and magnetic properties of $\text{Ca}_3\text{Ru}_2\text{O}_7$ revealed an unusual bulk spin valve state. Spinvalve effects are usually only observed in thin film systems, in which FM layers alternate with non-magnetic buffer layers — a natural property of the layered $\text{Ca}_3\text{Ru}_2\text{O}_7$ system where the ground state consists of nearly half-metallic bilayers stacked antiferromagnetically with a weak coupling where the out of plane transport is very strongly

1.1. General overview of Layered Ruthenates

suppressed by the antiferromagnetic alignment, which can be destroyed in favor of ferromagnetism at low energy cost [71].

The enigmatic "semimetallic" like phase in $\text{Ca}_3\text{Ru}_2\text{O}_7$ and the close proximity of $\text{Ca}_3\text{Ru}_2\text{O}_7$ to Mott insulating state with extreme sensitivity to impurities makes it an ideal system to study the interplay between correlated metal physics associated with the Fermi surface and Mott physics associated with Coulomb repulsions and orbital physics [64]. The contradictory results from quantum oscillations and ARPES pointing towards the presence of small Fermi surface pockets and boomerang like arcs in the FS respectively [66, 72, 73] suggests that the electronic structure of $\text{Ca}_3\text{Ru}_2\text{O}_7$ and the symmetry breaking remain unsettled. In the recent transport measurements by Xing *et al.* [72], an anisotropy in thermopower pointed towards evidence for existence of both electron like and hole like pockets in the FS. The ARPES studies by Horio *et al.* [14] also observed the anisotropic FS, discussed earlier and showed that the system reconstructs from a strongly correlated metal into a C_2 - symmetric Dirac semimetal. Although this provided a reconciliation between the hitherto incompatible scenarios proposed by the ARPES, QO and transport measurements, the ordered state that energetically favors the C_2 - symmetric Dirac semimetal still remains elusive. In the second part of this thesis, we investigate the bilayer ruthenate- $\text{Ca}_3\text{Ru}_2\text{O}_7$ with magnetotransport measurements- to reveal its electronic structure and properties. The characteristic temperature scales identified are linked to the various reconstructions of the low energy electronic structure. An analysis scheme is formulated to model the observed magnetoresistance (MR) with two-band model for conductivity and is shown that the model works in the low field low temperature regime prior to reconstructions in the Fermi surface.

Chapter 2

Experimental Techniques

This chapter discusses the various experimental techniques that have been utilised in the studies presented in this thesis work. Here, a detailed description of the spectroscopy techniques used- namely x - ray absorption spectroscopy (XAS) and resonant inelastic xray scattering (RIXS), is given. Bulk measurements such as resistivity and Hall measurements, thermoelectricity, and magnetization that were used in studying the physical properties of the systems described in this work are presented here as well. A brief account of the home built thermoelectric set up for measuring Seebeck, Nernst and Thermal Hall effect is given. The sample preparation and characterisation using Laue diffraction and Detwinning is also briefly discussed.

2.1 Spectroscopy Techniques

2.1.1 XAS

XAS is an element - selective probe that consists of irradiating the sample with monochromatic x - rays and measuring the x - ray absorption versus x - ray energy. It by definition measures the exponential decay of a beam of photons of a given energy through a sample given by Beer's Law [74, 75]

$$I_t(t) = I_0 e^{-\mu(E)t} \quad (2.1)$$

where I_t is the transmitted intensity and $\mu(E)$ is the energy dependent x - ray absorption coefficient. (See Fig 2.1). $\mu(E)$ varies approximately as $\mu(E) \sim \frac{dZ^4}{mE^3}$, where d is the density of the target, m and Z are the atomic mass and number respectively. When the sample absorbs the incoming photon, depending on its energy, it can promote the system to an excited state or results in a photoelectron

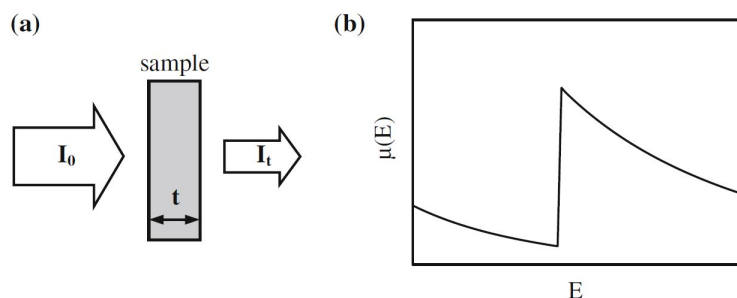


Fig. 2.1 Schematic of incident and transmitted x - ray beam. (b) absorption coefficient $\mu(E)$ versus photon energy E around an absorption edge. Taken from Ref. [74]

that is promoted to a free or continuum state which then propagates within the material and is scattered by the atoms near the absorber. Accordingly, the various regions of the spectrum (pre-edge, near edge or far from edge) contain information about the coordination geometry, oxidation state, and bond lengths of the absorbing atom. XAS encompasses x - ray absorption near edge structure (XANES) and the extended x - ray absorption fine structure (EXAFS). XANES (It is the part of the XAS spectrum developing in the range of few tens of eV around the edge.) provides more details about the electronic density of states and the coordination symmetry, while EXAFS (This region shows a slow decrease in the absorption rate versus energy, but with superimposed oscillating structures) enlightens about the radial distribution function of the surrounding atoms and their order/disorder [75].

The specific energy values at which there is sudden increase in the absorption probability, that depends mainly on the atomic number of the absorbing atom, is called an edge. As the spectra is governed by dipole selection rules, by varying the photon energy a spectrum is obtained that is proportional to an average of site-specific, unoccupied symmetry selected density of states (DOS) [75]. When the incoming photon energy is tuned to the $1s$ binding energy of an atom the spectrum will exhibit a discontinuity called the “ K - edge” created by excitations from the $1s$ state to unoccupied p -states in the conduction bands. Similarly, The absorption discontinuity is known as an “ L - edge” when the ionization is from a $2s$ or $2p$ electron. The Fig 2.2 shows an energy level diagram and the energies of various absorption edges. In our study we have used the oxygen K - edge XAS where the incoming x - ray energy around 530 eV results in the excitation of an oxygen $1s$ core electron to an empty $2p$ state.

Different techniques are employed to measure the XAS spectra which includes transmission detection, Fluorescence yield, electron yield and ion yield detection. x - ray transmission is the most direct technique to measure an oxygen K - edge XAS spectrum and it allows the quantitative detection of the x - ray absorption cross section. Thin samples are needed in this mode of detection as the attenuation of

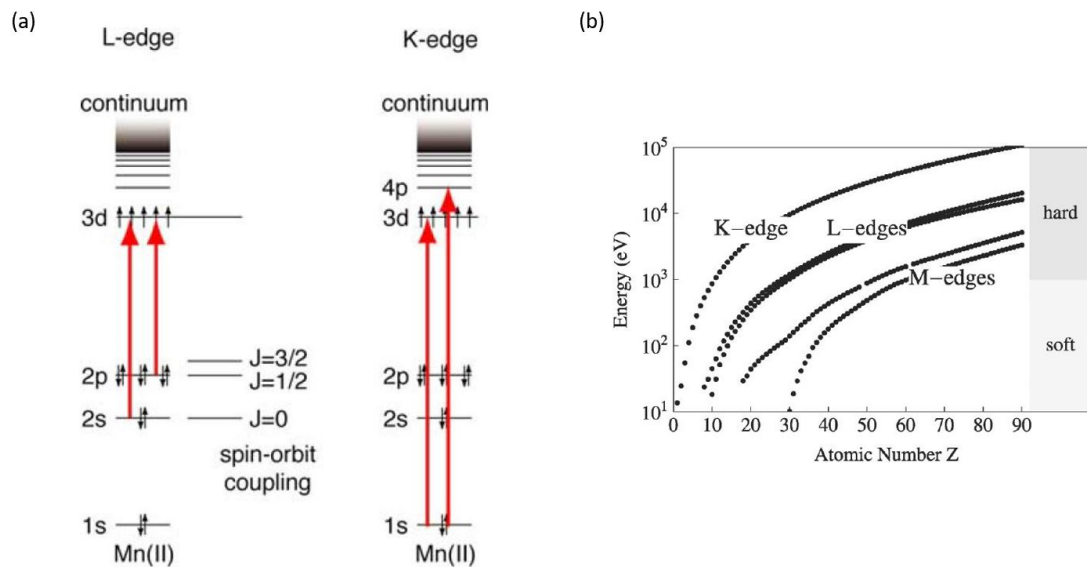


Fig. 2.2 (a) An example of an energy level diagram for L - edge transitions ($2s$ and $2p$ to $3d$) and K - edge transitions ($1s$ to $3d$ and $4p$) for Mn(II) system. Taken from Ref. [76] (b) Energies of different x - ray absorption edges as a function of atomic number Z . Taken from Ref. [77]

530 eV x - rays is only 100 nm at the oxygen K - edge of solid oxides. This makes a transmission measurement quantitatively correct for samples of homogeneous thickness [78]. The other detection methods are based on decay channels of the core-hole. After a short time of the order of 10^{-15} s, the core-hole is filled by an electron from a higher energy state. The corresponding energy difference is released mainly via fluorescence x - ray or Auger electron emission. Fluorescence yield measures the amount of x - rays that are emitted. Auger process results in the emission of electrons and the electron yield technique measures the total number of emitted electrons. In Fluorescence Yield Detection technique, the energy emitted as an x - ray when a core-hole is filled with an electron from another shell is measured. Detecting the fluorescent x - rays after radiative core-hole decay can yield a method that is proportional to the XAS spectral shape. In total fluorescence yield (TFY) detection, all emitted x - ray photons, from all elements present in the sample are detected [78]. In our experiment we have utilised the TFY detection technique. In total electron yield (TEY), electrons that escape from the sample are detected in electron analyzers. This can include the integrated signal from energy dispersive detectors or, in the case of conductive samples, the current measurement to the sample. The penetration depth of x - ray photons is larger than the escape depth of electrons, hence the TEY technique is more surface sensitive than the TFY. [78, 79]. Most XAS experiments are performed at synchrotron sources due

to the requirement of high x - ray intensities and a continuous energy spectrum. The results presented in this thesis were carried out at the ADDRESS beamline at the Swiss Light Source (SLS).

2.1.2 RIXS

XAS is the first step of the RIXS process. As discussed above, a common way to measure XAS is to study the decay products of the core hole that the x - ray has created, either by measuring the electron yield from a variety of Auger and higher - order processes or by measuring the radiative decay (fluorescence yield). The TFY corresponds approximately to the integration of all possible RIXS processes [77]. The decay of the final excited state by either emitting a photon or an electron could be recorded by utilising x - ray emission spectroscopy (XES) by an instrument with bandwidth of the order of the core hole life time broadening. The decay could be a multistep process with various intermediate steps. XES is hence a second order process which includes resonant inelastic scattering [75].

RIXS is a photon in- photon out process where the incoming photon energy is tuned to resonate with absorption edges. The resonance can greatly enhance the inelastic scattering cross section, and provides a unique way to probe charge, magnetic, and orbital degrees of freedom on selected atomic species in a crystal. This technique can measure the energy, momentum, and polarization change of both incident and scattered photons. Since the changes in energy, momentum, and polarization of the photon are transferred to intrinsic excitations of the material under study, RIXS provides information about those excitations [77].

The incoming photon energy of the x - rays are tuned to resonate with the absorption edges of the absorbing atom. For example, in a copper oxide material the incoming photon is chosen so that it resonates with the copper K , L , or M absorption edges. The copper K - edge transition $1s \rightarrow 4p$ is around 9000 eV and in the hard x - ray regime. The $L_{2,3}$ edge $2p \rightarrow 3d$ (~ 900) eV and $M_{2,3}$ edge $3p \rightarrow 3d$ (~ 80) eV are soft x - ray transitions. Alternatively, by tuning to the oxygen K edge, an electron is promoted from O $1s$ to an empty $2p$ valence state, which takes around ~ 500 eV.

After absorbing xray photon, the system is in a highly energetic, unstable intermediate state with a hole deep in the electronic core. It quickly decays, typically within 1 – 2 fs, in a number of ways, for example, via an Auger process, where an electron fills the core hole while simultaneously emitting another electron. This is a nonradiative decay channel and is not relevant for RIXS. RIXS process is instead governed by fluorescent decay, in which the empty core state is filled by an electron with the simultaneous emission of a photon. There are two different scattering mechanisms by which the energy and momentum of the emitted photon

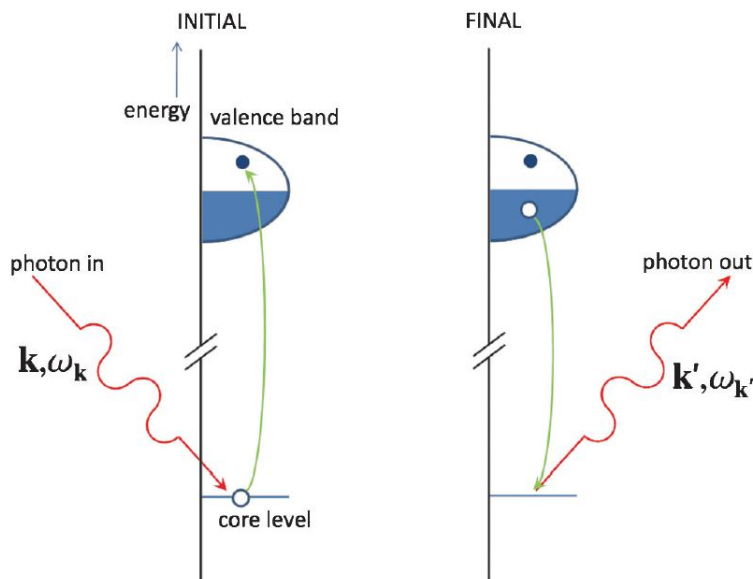


Fig. 2.3 Schematic representation of a direct RIXS process. The incoming x rays excite an electron from a deep-lying core level into the empty valence band. The empty core state is then filled by an electron from the occupied states under the emission of an x ray. Taken from Ref. [77]

can change from the incident one- namely the direct RIXS process and indirect RIXS process. For the purpose of this study we utilise the direct RIXS process, where the incoming photon promotes a core electron to an empty valence band state with the subsequent decay of an electron from a different state in the valence band and annihilation of the core hole. Fig 2.3 shows the direct RIXS process. As an electron was created in an empty valence band state and a hole in the filled valence band, final state is an electron-hole excitation, which propagate through the material, carrying momentum $\hbar(\mathbf{k}' - \mathbf{k})$ and energy $\hbar(\omega_{\mathbf{k}} - \omega_{\mathbf{k}'})$ where $\hbar\mathbf{k}$ ($\hbar\mathbf{k}'$) and $\hbar\omega_{\mathbf{k}}$ ($\hbar\omega_{\mathbf{k}'}$) are the momentum and energy of the incoming(outgoing) photon respectively. These transitions in the K edge of oxygen, for instance, involves an initial dipolar transition from core to valence state of $1s \rightarrow 2p$ followed by a succeeding transition from conduction state to fill the core hole by the decay of another electron in the $2p$ band from $2p \rightarrow 1s$. RIXS is thus an effective direct probe of the valence and conduction states.

RIXS is also an effective probe for studying and understanding a variety of intrinsic excitations in the system as the incoming photon transfers momentum and energy to the material under study. An example of various excitations that can be studied using the method is shown in Fig 2.4 [77]. A very broad class of excitations can be studied including plasmons, charge transfer excitations, crystal-field and orbital excitations, magnons and phonons.

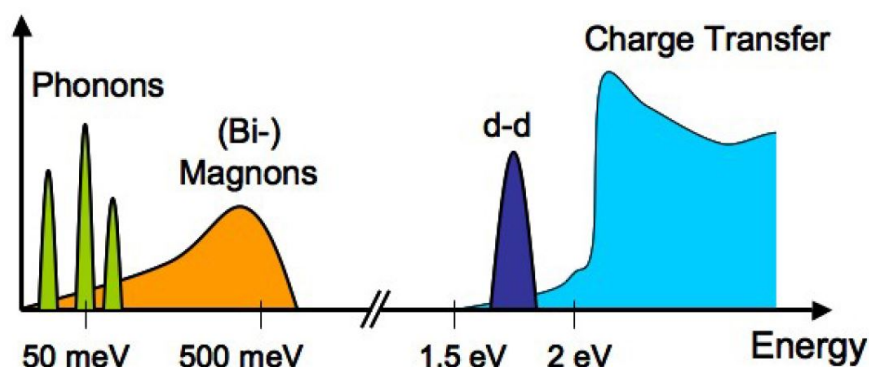


Fig. 2.4 . Elementary excitation spectrum in solids can range from plasmons and charge-transfer excitations at energies of a few eV, down to phonons at the meV scale. RIXS is a useful probe in studying the dispersion of these excitations as the impinging photon transfers both momentum and energy to the sample under consideration. Taken from Ref. [77].

2.1.3 RIXS Instrumentation

A RIXS instrument can be divided into two parts, the beam line and the spectrometer. The beam line provides a well-collimated, highly monochromatic, focused, beam onto the sample. The spectrometer, which must provide the sample environment, manipulate the scattering angles to vary the momentum transfer, collects the scattered radiation over an appropriate solid angle, and analyze the energies of scattered radiation. Hard x - ray instruments are built around Bragg crystal optics to achieve the required very high-energy resolution and uses the highly ordered crystalline lattice of Si or Ge that is comparable to the x - ray wavelengths used. For soft x - ray regime, where the long wavelengths prohibit the use of crystal optics, artificial periodic structures such as diffraction gratings are used. The lined gratings act as a series of slits and the light diffracts from these. The resolution is determined by the number of lines per millimeter. Here we discuss the instrument at the Swiss Light Source. It consists of a beam line, known as ADDRESS (Advanced Resonant Spectroscopies), and a spectrometer, known as SAXES (SuperAdvanced x - ray Emission Spectrometer). The beam line utilises a plane grating monochromator (PGM) diffraction grating with a line spacing of up to 4200 mm^{-1} , together with collimating mirrors operating in the energy range 300 – 1600 eV. The beamline delivers a high flux $> 10^{13}$ photons/second within 0.01 % bandwidth at 1 keV photon energy. The energy resolution is extremely good, with a resolving power of over 33000 at 1 keV (i.e., an energy resolution of 33 meV) [77, 80, 81].

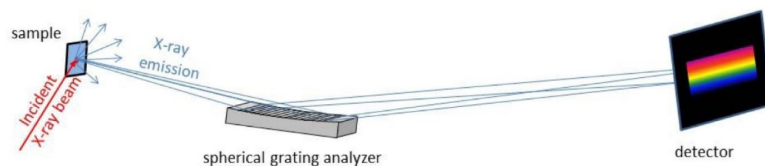


Fig. 2.5 Schematic view of a conventional RIXS detection scheme using a reflective grating with varying line spacing (VLS). Taken from Ref. [82]

The optical scheme of SAXES spectrometer is based on spherical variable line space (VLS) grating which collects the scattered radiation and disperses it onto a charge coupled device (CCD) camera (See Fig 2.5).

The overall energy resolution of the instrument is largely determined by the line spacing of the grating and the spatial resolution of the CCD camera. SAXES uses 2 different gratings, groove density of $a_0 = 3200$ lines/mm optimized for high-resolution measurements around 930 eV (Cu $L\beta$ edge) and another groove density of $a_0 = 1500$ lines/mm to cover energies from the Nitrogen K - edge at 400 eV through the Fe $L\beta$ at 720 eV, and deliver an energy resolution, $E/\Delta E$ above 10,000 at the O K edge at 530 eV [83]. The dispersed light is then allowed to propagate in vacuum until it is incident on the CCD camera. SAXES utilises a high resolution electron multiplying charge coupled device (EM-CCD) camera for RIXS. The detector system comprises of three horizontally arranged chips with 1608×1632 pixels each with pixel size of $16\mu m \times 16\mu m$ [82]. The advantage of using three chips next to each other is better statistics and therefore reduced acquisition time. Due to charge leakage between neighboring pixels, single photon signal will appear to be observed by several pixels. The camera is therefore operated at a grazing incidence 20° to match the effective pixel size to the charge distribution caused by a single photon and reduce the effective pixel size. [77, 80]. This in combination with a single photon counting algorithm further reduces the effective pixel size to about $1.37 \mu m$ [82]. The whole spectrometer (grating plus CCD) is then mounted on a large (5 m) girder, and the whole girder is able to rotate in the horizontal plane about the sample position which allows for varying the scattering angle of incoming and outgoing photons between $25^\circ - 130^\circ$ thereby facilitating the study of the dispersion of low-energy excitations as a function of momentum transfer [77] (See Fig 2.6).

Fig 2.7 shows an example of RIXS spectrum on Ca_2RuO_4 sample recorded by the detector at the high resolution ADDRESS beamline of the Swiss Light Source, which operates in the soft x - ray energy range and employs plane diffraction gratings.

In the spectrum recorded by the detector, each channel corresponds to a specific photon energy and the difference between two neighbouring channels in the oxygen

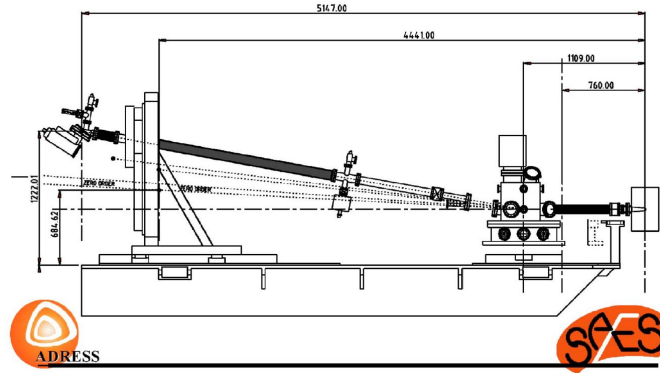


Fig. 2.6 Simplified drawing of the SAXES. The sample is at the right side. The whole spectrometer is supported by a single steel girder which can rotate around a vertical axis passing on the sample allowing for the study of transferred photon momentum dependent RIXS spectra. Taken from Ref. [80]

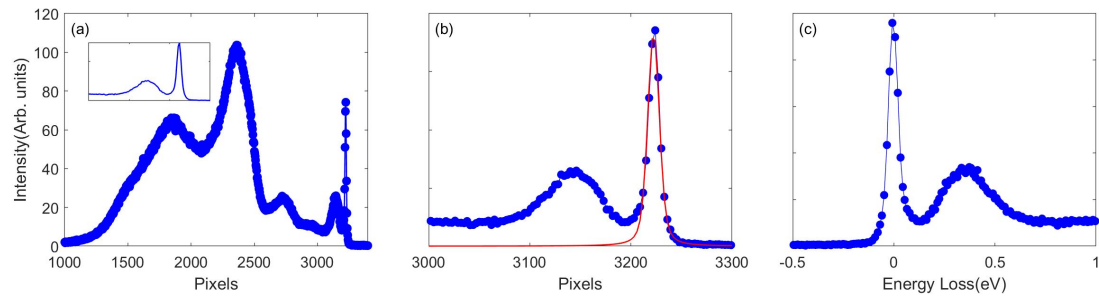


Fig. 2.7 (a) Example of a Raw RIXS spectrum taken on Ca_2RuO_4 sample detected by the CCD camera. Intensity recorded as a function of vertical pixel. The inset shows a zoom-in near the elastic region. (b) The elastic line is fitted with a Voigt function (shown in red) and the exact position of the elastic line is determined. (c) The pixels are converted to energy (In our experiment energy of the pixel is around 45 meV) and the elastic line is shifted to match the zero energy-loss position.

K - edge measurements presented in this thesis is equal to 45 meV. For elastic events, the value of the incoming photon energy is the upper limit for the detected energies. The first sharp feature from the high energy side is attributed to the elastic peak $\hbar\omega_{in} = \hbar\omega_{out}$. Here, the high energy side corresponds to higher pixel number. The elastic peak can therefore be used to set the zero energy loss in the spectrum. If the elastic peak on the sample is suppressed or there are low energy excitations partially or totally covering it, it is useful to take a reference on amorphous carbon (it is sufficient to apply some carbon tape next to the sample, at approximately the same height as the sample surface) as the width of the elastic signal recorded on the carbon tape is not affected by low energy features [79].

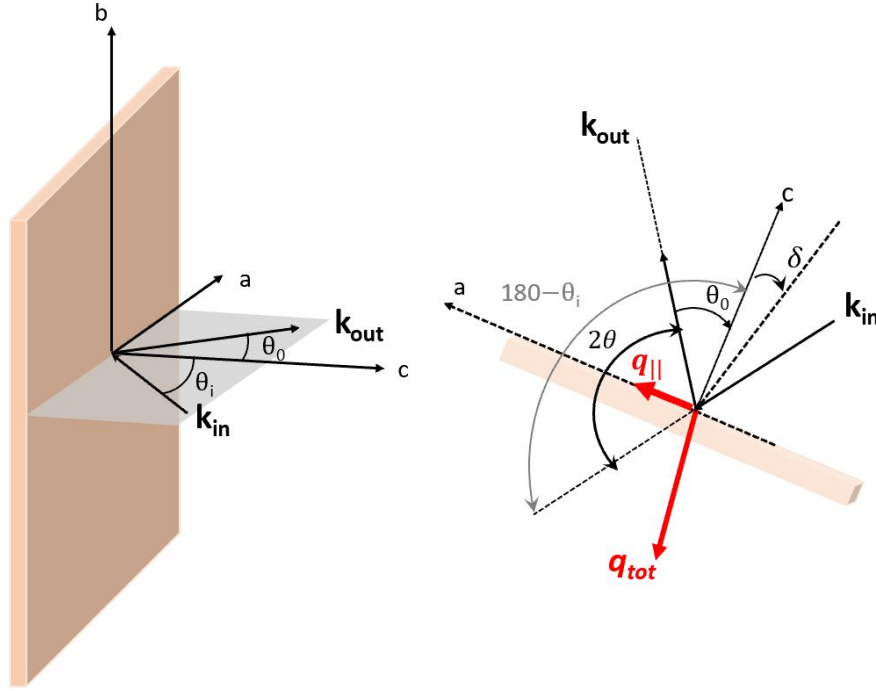


Fig. 2.8 The experimental geometry used in the measurements. For more details specific to the sample studied, refer Fig 3.4. The incoming beam makes an angle θ_i with the c -axis and the outgoing beam is collected at an angle θ_o . The scattering angle 2θ is fixed. δ is the angle between c -axis and total momentum transferred. The projection of q onto the sample ab -plane, q_{\parallel} is marked in red. δ can be varied by rotating the sample around an axis perpendicular or parallel to the scattering plane, thereby facilitating the measurement of inplane momentum dispersion in the 2D reciprocal space. The conventions used are adapted from [85]

Fig 2.8 shows a typical experimental geometry for RIXS measurements discussed in this thesis. For a detailed discussion of the measurement layout, refer Section 3.4. The conventions used have been adopted from References [84, 85]. In the experiments shown in this thesis, the in-plane momentum dispersion is measured along the Ru-O instead of the Ru-Ru direction. Therefore the reciprocal space is indexed by $\mathbf{q} = h\mathbf{a}_T + k\mathbf{a}_T + lc$, where \mathbf{a}_T and \mathbf{b}_T are the reciprocal lattice vectors pointing along the in-plane Ru-O bond as in tetragonal convention. The lattice parameters in real space are then $a_T \approx b_T \approx \sqrt{a^2 + b^2}/2$ [86]

The incoming beam impinges on the sample at an angle θ_i and the outgoing beam makes an angle θ_o with the c -axis. For the study of a two-dimensional system, the scattering angle 2θ is fixed, and the incident angle can be varied by rotating the sample holder. For our measurements a scattering angle $2\theta = 130^\circ$ has been used. The angle δ is defined as the angle between total transferred

momentum \mathbf{q}_{tot} and c - axis. The momentum of the photon \mathbf{k} is determined by the radiation used. Even though the scattering angle is fixed, changing the angle δ by changing the incidence angle allows to vary the in - plane momentum transfer \mathbf{q}_{\parallel} by rotating the sample around an axis perpendicular to the scattering plane, allowing to measure dispersing features. With this notation, the projection of the total momentum transferred onto the ab plane is $\mathbf{q}_{\parallel} = 2\mathbf{k} \sin(\theta) \sin(\delta)$, where $\mathbf{k} = \mathbf{k}_{\text{in}} \approx \mathbf{k}_{\text{out}}$. Specular condition would require the angle $\delta = 0$ and \mathbf{q}_{\parallel} in this case would be zero and the excitation at the center of the Brillouin Zone can be studied. In this way, by varying the angle δ , the evolution of a given excitation along a chosen direction of the square 2D Brillouin zone (BZ) can be studied.

The main limitation of RIXS is the energy resolution, which is determined by both the availability of tunable photon sources that provide a high enough photon flux and the availability of the instrumentation to resolve the energy of scattered photons. In addition, for soft x - ray RIXS, the reciprocal space that can be measured is usually limited to the first Brillouin zone due to the scattering geometry. However, the RIXS resolution has improved considerably over the years and currently a resolution of ~ 35 meV at Cu $L\beta$ edge can be achieved at several state-of-the-art beamlines including the ID32 at the ESRF, I21 at Diamond light source, the SIX at NSLSII, and the European Synchrotron Radiation Facility (ESRF) [87].

2.2 Transport Measurements

2.2.1 Resistivity and Hall measurements

The momentum of a free electron is related to the wave vector [88] \mathbf{k} by

$$m\mathbf{v} = \hbar\mathbf{k} \quad (2.2)$$

The force \mathbf{F} experienced by an electron of charge $-e$ in an electric field \mathbf{E} and magnetic field \mathbf{B} is given by

$$\mathbf{F} = m \frac{d\mathbf{v}}{dt} = \hbar \frac{d\mathbf{k}}{dt} = -e(\mathbf{E} + \mathbf{v} \times \mathbf{B}) \quad (2.3)$$

At a constant applied electric field that acts for a time interval t and zero magnetic field, in the absence of collisions, the fermisphere that encloses the occupied electron orbitals in \mathbf{k} space is displaced at a uniform rate given by

$$\delta\mathbf{k} = \mathbf{k}(t) - \mathbf{k}(0) = -e\mathbf{E}t/\hbar \quad (2.4)$$

Due to the collisions of the electrons with impurities, phonons, crystal imperfections etc... the displacement may be maintained at a steady state. If the collision time is given by τ then displacement in steady state given by equation 2.4 reads $\delta\mathbf{k} = \mathbf{k}(t) - \mathbf{k}(0) = -e\mathbf{E}\tau/\hbar$ and the velocity $\mathbf{v} = -e\mathbf{E}\tau/m$. In a constant electric field with n electrons of charge $q = -e$ per unit volume, the electric current density is given by the Ohm's Law

$$\mathbf{J} = nq\mathbf{v} = \frac{ne^2\tau}{m} \mathbf{E} \quad (2.5)$$

The electrical conductivity σ is given by $\mathbf{J} = \sigma\mathbf{E}$ which gives $\sigma = \frac{ne^2\tau}{m}$. The electrical resistivity is defined as

$$\rho = \sigma^{-1} = \frac{m}{ne^2\tau} \quad (2.6)$$

In electrical resistivity measurements it is often convenient to define a quantity called the residual resistivity ratio(RRR) of the sample under consideration. The electrical resistivity of most metals at room temperature is dominated by the collision of conduction electrons with lattice vibrations and at low temperatures by the collisions with impurity atoms and lattice imperfections and the net resistivity ρ is given by [88],

$$\rho = \rho_L + \rho_i \quad (2.7)$$

where ρ_L and ρ_i are caused by thermal phonons and lattice imperfections respectively. The residual resistivity $\rho_i(0)$ is the extrapolated resistivity at 0K as ρ_L vanishes in the limit $T \rightarrow 0$. The residual resistivity ratio is then defined as the ratio of its resistivity at room temperature to its residual resistivity and is hence a convenient approximate indicator of sample purity [88].

With equations 2.3 and 2.4, equation of motion for the displacement of the fermisphere of particles by $\delta\mathbf{k}$ due to a force \mathbf{F} and by collisions is given by

$$\hbar \left(\frac{d}{dt} + \frac{1}{\tau} \right) \delta\mathbf{k} = \mathbf{F} \quad (2.8)$$

This was derived for zero applied magnetic field. Now we consider the motion of the system in a uniform magnetic field \mathbf{B} . The Lorentz force acting on an electron is then given by

$$\mathbf{F} = -e(\mathbf{E} + \mathbf{v} \times \mathbf{B}) \quad (2.9)$$

Assuming the static magnetic field to be parallel to the z- direction $\mathbf{B} = (0, 0, B)$ and with $m\mathbf{v} = \hbar\delta\mathbf{k}$, the equations of motion for a charge carrier q is as follows

$$\begin{aligned} m^* \left(\frac{d}{dt} + \frac{1}{\tau} \right) v_x &= q(E_x + Bv_y) \\ m^* \left(\frac{d}{dt} + \frac{1}{\tau} \right) v_y &= q(E_y - Bv_x) \\ m^* \left(\frac{d}{dt} + \frac{1}{\tau} \right) v_z &= qE_z \end{aligned} \quad (2.10)$$

where m^* is the effective mass. The Hall effect is the electric field developed across a conductor in the direction $\mathbf{j} \times \mathbf{B}$ when a current \mathbf{J} flows across a magnetic field \mathbf{B} . See Fig 2.9. The Hall effect represents a steady state of the system in a static electric field where the time derivatives of the velocities are zero. $\frac{dv_x}{dt} = \frac{dv_y}{dt} = \frac{dv_z}{dt} = 0$. For simplicity, the electric field is assumed to be $\mathbf{E} = (E_x, E_y, 0)$; we assume that any effect is going to occur in the plane perpendicular to \mathbf{B} because of the nature of the Lorentz force.

$$\frac{m^* v_y}{\tau} = qE_y - \frac{qB\tau}{m^*} (qE_x + qv_y B) \quad (2.11)$$

Defining the cyclotron frequency $\omega_c \equiv \frac{eB}{m^*}$, the equation 2.11 is rewritten as

$$v_y (1 + \omega_c^2 \tau^2) = \frac{q\tau}{m^*} (E_y - \omega_c \tau E_x) \quad (2.12)$$

In the limit $\omega_c \tau \ll 1$, the equation is given by,

$$v_y = \frac{q\tau}{m^*} (E_y - \omega_c \tau E_x) = \frac{q\tau}{m^*} \left(E_y - \frac{qB\tau}{m^*} E_x \right) \quad (2.13)$$

For arbitrary number of charge carriers with each carrier indexed by an integer j, the j^{th} carrier type has an effective mass m_j^* , charge q_j , number density n_j and scattering rate τ_j , equation 2.13 can be rewritten as follows [88, 89]

$$v_{y,j} = \frac{q_j \tau_j}{m_j^*} \left(E_y - \frac{q_j B \tau_j}{m_j^*} E_x \right) \quad (2.14)$$

If the current cannot flow out of the rod in the y direction, the net transverse current is zero. Therefore,

$$\sum_j n_j v_{y,j} q_j = 0 \quad (2.15)$$

In the case of electrons in the conduction band (with effective mass m_{el}^* , scattering rate τ_{el} , charge q_{el} , density n_{el} and holes in the valence band (with effective mass m_h^* , scattering rate τ_h , charge q_h , density n_h), Equations 2.14 and 2.15 give,

$$\frac{n_{el}q_{el}^2\tau_{el}}{m_{el}^*}(E_y - \frac{q_{el}B\tau_{el}}{m_{el}^*}E_x) + \frac{n_hq_h^2\tau_h}{m_h^*}(E_y - \frac{q_hB\tau_h}{m_h^*}E_x) = 0 \quad (2.16)$$

$$E_y(n_{el}\mu_{el} + n_h\mu_h) = E_x(n_h\mu_h^2 - n_{el}\mu_{el}^2)B \quad (2.17)$$

where $\mu_{(el/h)} = \left| \frac{q_{(el/h)}\tau_{(el/h)}}{m_{(el/h)}^*} \right|$ are the mobilities of electron and hole respectively. With the charge $q_{el} = -e$ and $q_h = +e$

$$E_x = \frac{J_x}{\sigma} = \frac{J_x}{|e|(n_{el}\mu_{el} + n_h\mu_h)} \quad (2.18)$$

where J_x is the current density in the x- direction. Combining equations 2.16 and 2.17 we have,

$$R_H \equiv \frac{E_y}{J_x B} = \frac{1}{|e|} \frac{(n_h\mu_h^2 - n_{el}\mu_{el}^2)}{(n_{el}\mu_{el} + n_h\mu_h)^2} \quad (2.19)$$

Equations 2.15 and 2.16 show that, although no net current flows in the y direction, the currents carried in the y direction by a particular type of carrier can be non-zero. Carriers flowing in the y direction will experience a Lorentz force caused by B in the negative x direction. This back flow of carriers result in a change of resistivity E_x/j_x , thereby causing magnetoresistance and for magnetoresistance to be observed, the presence of more than one carrier type is necessary. For a simplified case, consider a metal with a simple spherical Fermi surface and isotropic, energy-independent effective mass and initially for simplicity we assume the electric field in the x-direction $\mathbf{E} = (E_x, 0, 0)$ [89]. The drift velocity $v_{D,x/y}$ experienced by electrons in such a case can be deduced from equation as follows

$$v_{D,x} = \frac{-e\tau}{m^*}[E_x + v_{D,y}B] \quad (2.20)$$

$$v_{D,y} = \frac{e\tau}{m^*}v_{D,x}B$$

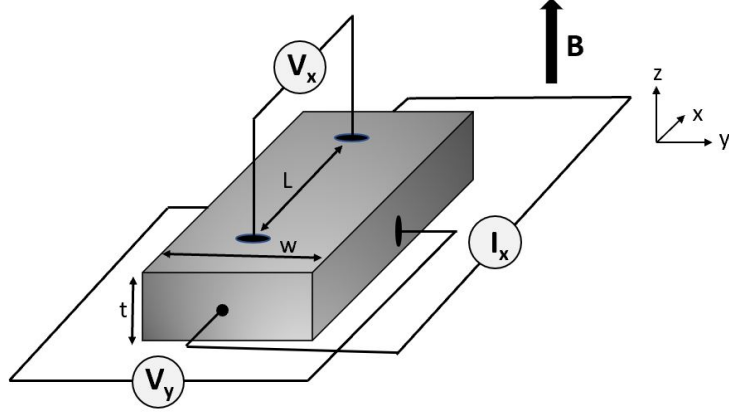


Fig. 2.9 Schematic of geometry of a combined resistivity and Hall measurement set up with magnetic field in the z -direction. The measurement records V and I , from which R can be calculated and is subsequently converted into $\rho_{xx} = \frac{RA}{L}$, where A is the cross sectional area- $A = wt$ and L is the distance between the voltage leads. Hall resistivity is calculated from $\rho_{xy} = tR_{xy}$ where t is the height of the sample. For $\text{Ca}_3\text{Ru}_2\text{O}_7$ sample we studied L, t and w were measured to be 0.015cm, 0.085cm, 0.03cm respectively.

Therefore in the presence of a magnetic field the conductivity is a tensor and the current densities $j_{x/y} = -nev_{D,x/y}$ gives

$$\begin{aligned} J_x &= \sigma_{xx} E_x, \\ J_y &= \sigma_{yx} E_x; \end{aligned} \tag{2.21}$$

$$\sigma_{xx} = \frac{\sigma_0}{1 + \omega_c^2 \tau^2}, \quad \sigma_{yx} = \frac{\sigma_0 \omega_c \tau}{1 + \omega_c^2 \tau^2}$$

Here $\sigma_0 = ne^2\tau/m^*$ is the zero-field conductivity in the Sommerfeld model [88] and $\omega_c = eB/m^*$ is the cyclotron frequency.

This shows that in the presence of an applied magnetic field the total current density no longer flows parallel to the applied electric field \mathbf{E} but has components in both x and y -directions.

From the above equations it is clear that in the limit $B \rightarrow \infty$ the conductivity scales as $\sigma_{xx} \propto B^{-1}$. In our experiments, as illustrated in Fig 2.9, the voltage drop across the contacts in x and y -directions are measured instead of the current density.

In such cases the current is forced in the x -direction, but the electric field would have components in both x and y -directions, such that $\rho_{xx} = E_x/J_x$ and

$\rho_{yx} = E_y/J_x$. The conductivity tensor is given by

$$\sigma = \begin{pmatrix} \sigma_{xx} & \sigma_{yx} \\ \sigma_{xy} & \sigma_{yy} \end{pmatrix} \quad (2.22)$$

Now considering the electric field in y-direction $\mathbf{E} = (0, E_y, 0)$, so that we have $\sigma_{xy} = -\sigma_{yx}$ and $\sigma_{yy} = -\sigma_{xx}$

$$\begin{aligned} J_x &= \sigma_{xx}E_x + \sigma_{xy}E_y \\ J_y &= \sigma_{yx}E_x + \sigma_{yy}E_y \end{aligned} \quad (2.23)$$

For Hall measurements, since there is no current flow in the y-direction, $j_y = 0$; This gives,

$$E_y = \frac{\sigma_{xy}E_x}{\sigma_{xx}} \quad (2.24)$$

Using this in equation 2.23, we have

$$J_x = \frac{\sigma_{xx}^2 + \sigma_{xy}^2}{\sigma_{xx}} E_x \quad (2.25)$$

Using this in 2nd part of equation 2.23 we have an expression for E_y given by,

$$E_y = \frac{\sigma_{xy}}{\sigma_{xx}^2 + \sigma_{xy}^2} j_x \equiv R_H B J_x \quad (2.26)$$

where R_H is the Hall coefficient.

The conductivity tensor can thus be rewritten as

$$\sigma = \begin{pmatrix} \sigma_{xx} & -\sigma_{xy} \\ \sigma_{xy} & \sigma_{xx} \end{pmatrix} = \frac{\sigma_0}{1 + \omega_c^2 \tau^2} \begin{pmatrix} 1 & \omega_c \tau \\ -\omega_c \tau & 1 \end{pmatrix} \quad (2.27)$$

where $\sigma_0 = m/ne^2\tau$. The resistivity thus obtained is as follows $\rho_{xx} = \rho_0$ and $\rho_{xy} = -B/ne$. Thus for one carrier system, no magnetoresistance is observed in the diagonal components, whereas Hall effect for single carrier is seen in the off diagonal components. Now when an arbitrary number 'j' type of carriers are considered, each type with different density, effective mass and scattering rate, the current density can be written as $\mathbf{J}_j = \sigma_{xx,j}E_x\mathbf{e}_1 + \sigma_{yx,j}E_y\mathbf{e}_2$ the subscript 'j' indicates the contribution from the j^{th} type carrier. Hence, the components of the conductivity tensor $\sigma_{xx,j}$ and $\sigma_{yx,j}$ will vary for different type of carriers resulting in \mathbf{J}_j that point in different directions. The total \mathbf{J} is given by

$$\sum_j \mathbf{J}_j = \mathbf{J} \quad (2.28)$$

When there are 2 carrier types i.e $j = 1, 2$, We have \mathbf{J}_1 and \mathbf{J}_2 that point in different directions, with the application of a magnetic field. For two carriers the electric field remains the same and the current densities as shown above add together

$$\mathbf{J} = \mathbf{J}_1 + \mathbf{J}_2 \quad (2.29)$$

The current densities can be written as

$$\begin{aligned} J_x &= [\sigma_{xx}^{(1)} + \sigma_{xx}^{(2)}]E_x + [\sigma_{xy}^{(1)} + \sigma_{xy}^{(2)}]E_y \\ J_y &= [\sigma_{xy}^{(1)} + \sigma_{xy}^{(2)}]E_x + [\sigma_{xx}^{(1)} + \sigma_{xx}^{(2)}]E_y \end{aligned} \quad (2.30)$$

Since the Hall effect is measured without current flow in the y direction, i.e. $J_y = 0$ and using the same method adopted for single carriers using Equation 2.27, we have

$$\sigma_{xx}^1 = \frac{\sigma_1}{1 + \sigma_1^2 R_1^2 B^2}, \quad \sigma_{xy}^1 = -\frac{\sigma_1^2 R_1 B}{1 + \sigma_1^2 R_1^2 B^2} \quad (2.31)$$

where $\sigma_{1/2}$ are the electrical conductivities of the two type carriers. Using these in Equations 2.25 and 2.26, we obtain the following relations for magnetoresistance and Hall resistivity in an applied field in a system of two carriers

$$\rho_{xx}(B) = \frac{(\sigma_1 + \sigma_2) + \sigma_1 \sigma_2 (\sigma_1 R_1^2 + \sigma_2 R_2^2) B^2}{(\sigma_1 + \sigma_2)^2 + \sigma_1^2 \sigma_2^2 (R_1 + R_2)^2 B^2}, \quad (2.32)$$

$$\rho_{xy}(B) = \frac{\sigma_1^2 R_1 + \sigma_2^2 R_2 + \sigma_1^2 \sigma_2^2 R_1 R_2 (R_1 + R_2) B^2}{(\sigma_1 + \sigma_2)^2 + \sigma_1^2 \sigma_2^2 (R_1 + R_2)^2 B^2} B. \quad (2.33)$$

where $R_{1/2}$ and $\sigma_{1/2}$ are the Hall coefficients and the conductivities of the carrier types (1) and (2) Hence in the two carrier case, we observe a finite magnetoresistance. This model is later used in section 4.4 to analyse the magnetoresistance data obtained for the $\text{Ca}_3\text{Ru}_2\text{O}_7$ sample.

2.2.2 Resistivity and Hall Measurement Set-up

The resistivity and Hall measurements discussed in this thesis have been performed in the Quantum Design PPMS system using the Resistivity option.

The PPMS can reach fields upto 9T and temperatures down to 1.8K. The resistivity of the specimen samples are determined using linear four probe technique. Samples for four-wire resistance measurements were mounted on standard PPMS sample pucks. Using four terminal sensing technique(Four probe method) to attach a sample to a sample puck greatly reduces the contact resistance during measurements [90].For reliable and accurate transport property measurements,

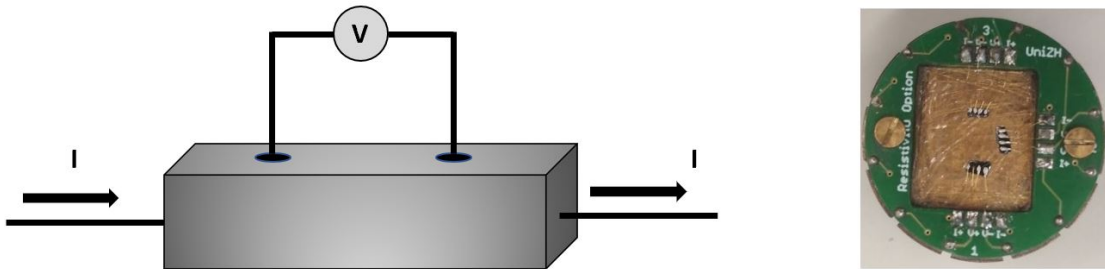


Fig. 2.10 (a) Schematic of Four-Probe technique used for resistivity measurements . Separate pairs of leads are used for current carrying and voltage sensing electrodes. This method is capable of making more accurate measurements than two terminal sensing. (b) Standard PPMS puck where samples for four-wire resistance measurements are mounted . Resistivity sample pucks have four contacts-one positive and one negative contact for current and voltage for each user bridge board channel. It has the ability to measure up to three samples to at one time.

good ohmic contact on samples is a prerequisite. Good contacts for the samples used in this thesis typically have a resistance of the order of 1Ω when measured with a multimeter. In a four-probe measurement, current is passed through a sample via two current leads, and two separate voltage leads measure the potential difference developed across the sample. See Fig 2.10.

The voltmeter has a very high impedance, so the voltage leads draw very little current. Therefore, by using the four-wire method, it is possible to know, to a high degree of certainty, both the current and the voltage drop across the sample and this inturn facilitates the calculation of the resistance with Ohm's law. Standard Resistivity sample pucks of the PPMS have four contacts- one positive and one negative contact for current and voltage for each user bridge board channel to which a sample may be wired . Up to three samples may be mounted on a Resistivity puck, so the Resistivity option can measure up to three samples at one time or as in in our case both resistivity and Hall measurements are done simultaneously on the same sample [90]. The base of the puck is conducting, so an insulating layer such as Kapton tape will be necessary for samples with conductive back sides. Electrical contact between the sample and the desired channel input pads were made via soldering or silver-painting wires on the samples discussed in this thesis. Sample was affixed on the puck on top of an insulating layer (we used cigarette paper) by means of an adhesive like GE Varnish which is a general-purpose adhesive that maintains its properties down to cryogenic temperatures. It is a reasonably good thermal conductor and an electrical insulator, ideal for mechanically anchoring samples to a puck before attempting to attach electrical leads. On the sample side, the connections were made using Silver wires glued

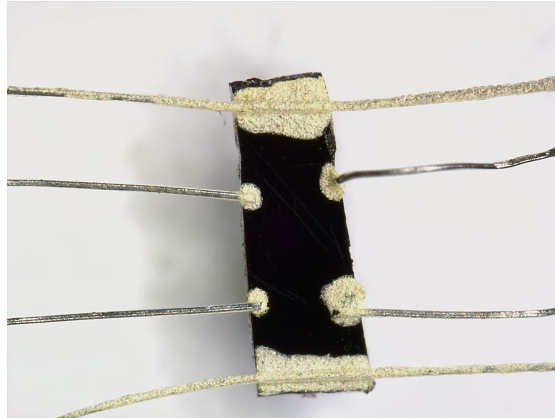


Fig. 2.11 Example of electrical contacts on a sample of $\text{Ca}_3\text{Ru}_2\text{O}_7$ for thermoelectric and resistivity measurements made using conducting DuPont 4929N silver paint and silver wires.

to the sample using Silver paste (namely DuPont 4929 N or two component Silver epoxy which requires curing above 80°C). Silver wires of diameter 0.05 mm and 0.1 mm are used in the connections on samples presented in this thesis. See Fig 2.11

The other end of the wires were soldered on the appropriate contact pad on the puck. In some cases, the contact resistance could still be high despite the room temperature curing of the silver paste, in such cases the contacts are heated in a furnace at high temperatures in an argon atmosphere which results in very low contact resistances. Another method that was adopted involved applying short high voltage pulses across the contact. This often leads to very good results. The exact process that leads to the best result on a given sample is often a process of trial and error [91].

2.3 Thermoelectric Studies

2.3.1 Thermopower/Seebeck and Nernst

Thermoelectric materials can convert waste heat to electrical energy and finding materials with large thermopower can be an ecologically friendly alternative for a sustainable energy future [92]. Identifying materials with large thermoelectric response is essential for the development of novel, next generation low energy consumption devices. The study of thermoelectric materials requires evaluation of the thermoelectric figure of merit zT at a given temperature T , given by

$$zT = S^2\sigma T/\kappa \quad (2.34)$$

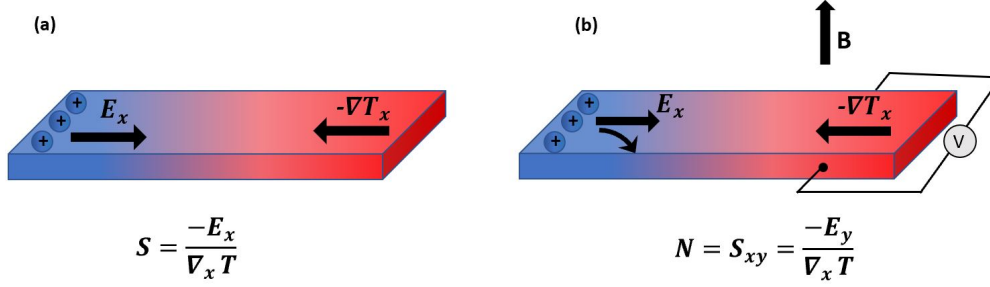


Fig. 2.12 In presence of a thermal gradient, an electric field is generated in the sample. (a) and (b) shows Seebeck(the longitudinal component of this field) and Nernst effect(transverse component) respectively

where S is the Seebeck coefficient, σ is the electrical conductivity and κ is the thermal conductivity comprising of both lattice and electrical contributions. The Seebeck coefficient is the ratio of the electric field to the thermal gradient applied to generate it See Fig 2.12 given by,

$$S = \frac{-E_x}{\nabla_x T} \quad (2.35)$$

black

The transverse counterpart to the Seebeck effect is called the Nernst effect which appears as a transverse electric field E_y in conductors subjected to a longitudinal temperature gradient ∇T (in x direction) and a perpendicular magnetic field B in z direction. See Fig 2.12

$$N = S_{xy} = \frac{-E_y}{\nabla_x T} \quad (2.36)$$

This effect as well as the longitudinal one were discovered by Nernst and Ettingshausen in a bismuth plate in 1886 [93, 94]. Associated with the current flow due to a thermal gradient in a conductor is the entropy flow per charge carrier [95, 96]. This can be expressed as follows:

$$J_s = S J_e - \kappa \nabla T / T \quad (2.37)$$

where, J_e is the charge current density, κ the thermal conductivity and ∇T the thermal gradient. In the absence of thermal gradient Seebeck coefficient is the ratio of entropy flow per charge flow. The Nernst coefficient, which is the transverse counterpart to the seebeck coefficient, is the measure of transverse entropy flow

caused by longitudinal particle flow [96].

$$E_y/\nabla_x T = J_y^s/J_x^e \quad (2.38)$$

For mobile fermionic quasi particles the core equation linking the electric and thermoelectric conductivity tensors is given by the Mott relation [97].

$$\alpha = \frac{\pi^2 k_B^2 T}{3e} \left. \frac{\partial \sigma}{\partial \epsilon} \right|_{\epsilon=\epsilon_F} \quad (2.39)$$

Hence the thermoelectric response is a measure of change in conductivity due to a shift in the chemical potential. In terms of Hall angle (defined as $\tan\theta_H = \frac{\sigma_{xy}}{\sigma_{xx}}$, where σ_{xy} and σ_{xx} are the transverse and longitudinal electrical conductivities respectively), Nernst effect can be written as follows [96]

$$N = \frac{\pi^2 k_B^2 T}{3e} \left. \frac{\partial \tan\theta_H}{\partial \epsilon} \right|_{\epsilon=\epsilon_F} \quad (2.40)$$

In the single band scenario Hall angle is equal to

$$\tan\theta_H = \omega_c \tau = \frac{eB\tau}{m^*} \quad (2.41)$$

where ω_c , τ and m^* are the cyclotron frequency, scattering time and the effective mass respectively, and the Nernst coefficient can hence be written as follows

$$\nu = N/B = \frac{\pi^2 k_B^2 T}{3m^*} \left. \frac{\partial \tan\theta_H}{\partial \epsilon} \right|_{\epsilon=\epsilon_F} \quad (2.42)$$

In the simplest approximation, where the change in chemical potential leaves the Hall angle unchanged, the Nernst response of the system is zero. In one band model it would lead to a vanishing nernst signal. However in two-band model where both electron and hole like carriers are present this would still lead to a finite nernst response [96]. When the Hall angle is energy dependent, in first approximation $\left. \frac{\partial \tan\theta_H}{\partial \epsilon} \right|_{\epsilon=\epsilon_F}$ can be replaced by $\frac{\tan\theta_H}{\epsilon_F}$ and expressing the Hall angle in terms of mobility we have,

$$\frac{\tan\theta_H}{B} = \mu = \frac{e\tau}{m^*} = \frac{e\hbar k_F}{l_e} \quad (2.43)$$

where k_F is the Fermi wavevector and l_e is the carrier mean free path. With these modifications the Nernst coefficient can be expressed as

$$\nu = \frac{\pi^2 k_B^2 T}{3e\epsilon_F} \mu \quad (2.44)$$

At $T \ll T_F$, the Seebeck coefficient of a metallic system is related to the Fermi temperature through this equation:

$$S = \frac{\pi^2 k_B T}{2eT_F} \mu \quad (2.45)$$

This is valid for free electron gas and is similar to the relation between specific heat γ of the free electron gas and the Fermi temperature [96]

$$\gamma = \frac{\pi^2 k_B T}{2T_F} n \quad (2.46)$$

where n is the molar density.

2.3.2 Thermoelectric Measurement Set up

For the thermoelectric data presented in this thesis, measurements were carried out with the aid of a homebuilt insert for Seebeck and Nernst measurements in the Quantum Design PPMS. The set up has been used to study Seebeck and Nernst effects in a variety of samples namely $\text{Ca}_3\text{Ru}_2\text{O}_7$ (Refer Section 4.3 for more information), PrAlGe , and EuCd_2As_2 (Refer Chapter 5). Thermopower and anomalous contribution to the Nernst effect were studied on the Type I Weyl semimetal- PrAlGe , which is a very interesting system in the sense that it breaks both time and inversion symmetry and is a potential candidate material for carrying pure spin currents. [98]. The Weyl nodes are generated by inversion symmetry breaking and the ferromagnetism in this system shifts the Weyl nodes in k -space and hence breaks the time reversal symmetry [99]. The Berry curvature in these systems acts as an intrinsic field and hence unusual transport properties like a finite transverse thermoelectric response even in the absence of external field, dubbed Anomalous Nernst effect, is observed in the system. Anomalous Hall effect is another transverse property that can be used to probe the topological nature of charge carriers in this system and has been done recently by Destraz *et al.* [98]. Recent studies have shown the existence of Weyl nodes close to Fermi energy level in EuCd_2As_2 (ECA) system with an applied field. Anomalous transport measurements in these materials have gained traction in recent years. Anomalous Hall

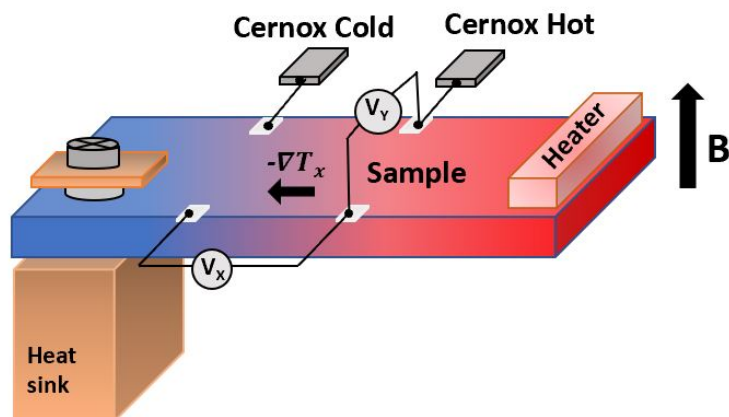


Fig. 2.13 Schematic illustration of the set up used for measuring the thermoelectric coefficients in the custom made probe. Temperature gradient is established by means of a linear pattern high resistance gage. Calibrated cernox chip sensors that measure the temperatures at the cold and hot end of the sample are depicted as cernox cold and hot respectively. V_x and V_y represents the longitudinal (Seebeck) and transverse (Nernst) voltage developed across the sample .

effect was predicted and experimentally realised in this system by J.R. Soh *et al.* [100]. EuCd_2As_2 is hence an ideal system to study the thermoelectric counterpart the Anomalous Nernst effect experimentally. Here, we have done, using our in-house built nernst set up, a study of the anomalous nernst effect in this system. A home built custom made insert in physical property measurement system was used to monitor the thermoelectric tensors in these samples. The schematic of the experimental set up is shown in the figure (Fig 2.13).

The temperature gradient across the sample is established using a linear pattern high resistance gage (5000Ω). The sample was attached on one end to a copper block (which serves as a heat sink) with a mechanical clamp (for better thermal contact), and the other end where the heater wire is attached is left free. The gradient established across the sample was maintained at 2 – 3% of the base temperature. Calibrated Cernox chip sensors were used to measure the temperature at the cold and hot end and hence the gradient established across the sample. The temperature of the sample was determined by taking the average of the temperatures at the hot and cold sides. The temperatures of the hot and cold ends of the sample were measured by continuously monitoring the resistance of the thermometers with Lakeshore temperature controller. The resistance is then converted to temperature by using a Labview program that has the calibration file for the thermometers. All the data acquisition programs were written in Labview. The

current to create the desired thermal gradient across the sample was applied with Keithley precision current source and the longitudinal and transverse voltage that develop across the sample were measured with Keithley 2182 nanovoltmeters used in conjunction with home built nanaovolt amplifiers. Cryogenic wires of Phosphor bronze from Lake Shore were used in the voltage leads that run from the sample inside the PPMS to the voltmeters at room temperature in order to minimise the heat leak as these wires have much lower thermal conductivity than normal copper wires. The wires were thermalized by winding them around parts of the probe that have a strong thermal link with the helium bath [101]. Contact misalignments are a potential cause of cross contamination between Nernst and Seebeck signals. If the transverse voltage contacts are not in perfect alignment, the transverse contacts will measure a fraction of the transverse field plus a fraction of the longitudinal field, and as a result a Seebeck component could appear in the raw Nernst data. Postacquisition data processing can compensate for the contamination of the transverse Nernst effect by the longitudinal Seebeck effect by symmetrisation of the data set. The seebeck thermopower is an even function of field and the nernst is an odd function of field. This allows for an easy way to eliminate the effects of contact misalignments, by symmetrizing the data: only the odd in-field components of the Nernst coefficient and the even in-field components of the Seebeck coefficients are kept. This is achieved by measuring the nernst signals at positive and negative field polarity. In order to remove any thermoelectric power contribution due to the misalignment of the contacts half the difference of the two polarities are taken [101, 102].

All the thermoelectric experiments are carried out in the Physical Property Measurement System, which can go down to a temperature of 1.8 K and reach field upto 9 T, at the University of Zurich. The required samples were obtained from our various collaborators. The bilayer ruthenate sample $\text{Ca}_3\text{Ru}_2\text{O}_7$ was obtained from our collaborator Antonio Vecchione at CNR-SPIN, University of Salerno, Italy, and the samples of the ferromagnetic Weyl semimetals were provided by our collaborators-Jonathan White, Pascal Pupal, and Ekaterina Pomjakushina at Paul Scherrer Institute, Switzerland.

2.4 Magnetometry

Magnetometry, refers to measurement of the magnetization M or the magnetic moment m of a sample. The magnetisation M of a homogeneous sample of volume V is given by $M = m/V$, where m is the magnetic moment of the sample. Magnetisation is hence often expressed in terms of emu/cm^3 . $1emu = 10^{-3}Am^2$. The results can also be expressed in $\mu_B/atom$, where μ_B is the Bohr magneton. The

number of atoms in the specimen in this case is at first determined as $atoms/cm^3$, and emu/cm^3 then gives $emu/atom$ which then is converted to $\mu_B/atom$ using $1\mu_B = 9.274 \times 10^{-21}$ emu [103].

The results presented in this thesis have been measured using lab-based magnetometry, namely, the superconducting quantum interference device (SQUID) magnetometer. SQUID magnetometers measure the magnetization of a specimen as a function of magnetic field and/or temperature. Here for the measurements presented, we have made use of the commercial Quantum Design SQUID magnetometer. The QD MPMS utilizes a superconducting magnet (a solenoid of superconducting wire) to subject samples to magnetic fields up to 7 Tesla (70 kOe) and provides temperature control of samples from 400 K down to 1.8 K achieved using liquid Helium [104].

SQUID magnetometers allow for the measurement of magnetic properties of small experimental samples over a broad range of temperatures and magnetic fields. In the work presented in this thesis, two types of measurements have been performed using the SQUID magnetometer namely- the variation of magnetic moment of sample with respect to temperature $M(T)$ in presence of magnetic field and the study of field dependence of magnetic moment $M(H)$ at constant temperature [103, 104]. The temperature dependence measurements can be performed under Zero field cooled (ZFC) or field cooled (FC) protocols. In the zero field cooling, no field is applied while the sample is cooled through the ordering temperature. In the field cooled process the sample is cooled through the ordering temperature in the presence of an applied field. These studies are useful in understanding the crucial role of magnetic anisotropy in the system that could cause a difference between the field cooled and zero field cooled values of magnetization. [105, 106].

The working principle of SQUID magnetometers are based on the Josephson effect and flux quantisation. A Josephson junction is comprised of two superconducting layers separated through an insulating layer. The laws of quantum physics dictate the magnetic flux through the ring to be quantized. This in turn results in a current flow through the ring to adjust the flux to an allowed value [88]. A change in flux from the external source is thus always reflected by a change in the voltage that is measured at the SQUID. This is the principle by which a SQUID translates a flux into a voltage. The working principle of SQUID can be based on DC(Direct Current) or AC(alternating current) Josephson effect and are termed DC SQUID and RF SQUID respectively. Here we have employed the DC SQUID magnetometry which has two Josephson junctions in parallel in a superconducting loop. To improve the overall sensitivity and noise rejection, reciprocating sample measurement option(RSO) was used which features small amplitude and periodic displacement of a sample inside the MPMS second order gradiometer. The move-

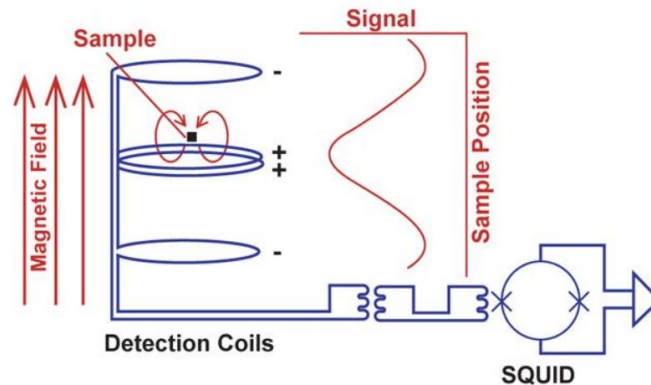


Fig. 2.14 A simplified schematic setup of a SQUID magnetometer. The sample is moved through the detection coils and the response of the coil is analysed to determine the sample position. Current is induced in the detection coils in response to magnetic field disturbances and is a function of the sample position. The approximate shape of this function is also shown. The current in the detection coils is inductively coupled to the instrument's SQUID, which serves as an extremely sensitive current-to-voltage converter. Taken from Ref [104].

ment of the sample results in an oscillating AC signal that is detected by the SQUID sensor. With the reciprocating sample technique, sensitivities of 10^{-8} emu can be achieved.

For measuring the magnetic moments the samples are mounted on quartz or brass or clear drinking straw sample holders using (GE) 7031 varnish. For accurate magnetic moment measurements, the magnetic signature of the sample holder before mounting the sample is measured. Once the sample moment is measured the background signal of the sample holder is subtracted from the sample measurement. SQUID magnetometers usually detect the change of magnetic flux created by mechanically moving the sample through a superconducting pick-up coil which is converted to a voltage. Before starting the measurements the sample is centered within the detector coils See fig 2.14 [104].

Sample is moved through the detection coils and the coil response is analysed to locate the sample. For samples with small moments, a magnetic moment $> 1 \times 10^{-7}$ emu is induced in the sample by applying a magnetic field. The sample has to be ideally located in the center of the pickup coils, inductively coupling to the magnetic field and generating a current as it moves through the coil. shown in Fig 2.14

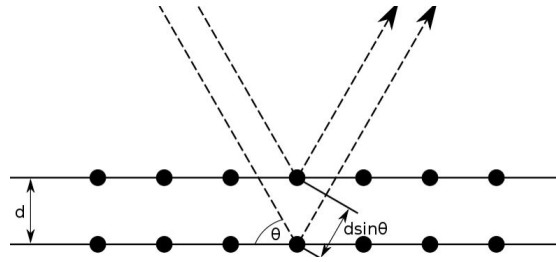


Fig. 2.15 Pictorial depiction of the derivation of Bragg equation $2d \sin(\theta) = n\lambda$. d is the spacing between the parallel atomic planes. Taken from Ref. [88]

2.5 Sample characterisation/Investigating Crystal Structures

2.5.1 X-ray diffraction: Laue Method

In condensed matter experiments, a prerequisite step in studying the physical properties of a single crystal sample of interest is determining its crystal structure and orientation. Here we employ the Laue diffraction technique and spot analysis to determine the crystal orientation. A simple explanation for diffracted beams from a crystal was presented by W.L Bragg.

When radiation, with a wavelength comparable to atomic spacings, is scattered in a specular fashion (angle of incidence equal to the angle of reflection) from parallel planes of atoms in a crystal, the diffracted beams are found when there is constructive interference. When the planes are spaced ' d ' distance apart, the path difference for rays reflected from adjacent planes is given by $2d \sin \theta$ and constructive interference occurs when the path difference is an integral number ' n ' of wavelength λ , given by the Bragg Law (See Fig 2.15)

$$2d \sin \theta = n\lambda \quad (2.47)$$

A generalised condition for the possible x - ray reflections is given by the Laue rule,

$$\Delta \mathbf{k} = \mathbf{G} \quad (2.48)$$

where $\Delta \mathbf{k}$ measures the change in wave vector and is called the scattering vector given by $\Delta \mathbf{k} = \mathbf{k}' - \mathbf{k}$, where \mathbf{k} and \mathbf{k}' are the wavevectors of the incoming and outgoing beams respectively. \mathbf{G} is a reciprocal lattice vector given by $\mathbf{G} = n_1 \mathbf{b}_1 + n_2 \mathbf{b}_2 + n_3 \mathbf{b}_3$ where $n_i, i = 1, 2, 3$ are integers and $\mathbf{b}_1, \mathbf{b}_2, \mathbf{b}_3$ are the primitive

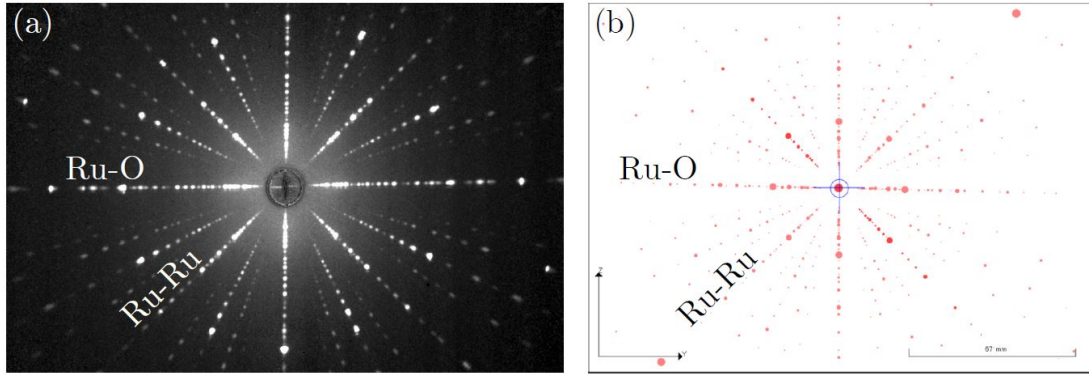


Fig. 2.16 (a) Measured Laue pattern of $\text{Ca}_3\text{Ru}_2\text{O}_7$. (b) Corresponding simulated Laue pattern using PSL viewer software used to distinguish the Ru-O and Ru-Ru directions. Taken from Ref. [107, 108]

vectors of the reciprocal lattice. An equivalent description of the result expressed in Equation 2.48 is given by the Laue conditions [88],

$$\begin{aligned}
 \mathbf{a}_1 \cdot \Delta \mathbf{k} &= 2\pi n_1 \\
 \mathbf{a}_2 \cdot \Delta \mathbf{k} &= 2\pi n_2 \\
 \mathbf{a}_3 \cdot \Delta \mathbf{k} &= 2\pi n_3
 \end{aligned} \tag{2.49}$$

where \mathbf{a}_i , $i = 1, 2, 3$ are the primitive vectors of the crystal lattice. Each of the three Laue conditions can be geometrically interpreted in the picture of Laue cones. For constructive interference to occur, the scattering vector must satisfy all the three equations; i.e it must lie in the common line of intersection of the three cones [88].

A Laue experimental set up consists of an x - ray source that is comprised of a Tungsten target on which electrons impinge, two cameras used for the alignment, a detection screen composed of a scintillating material and CCD chips, a manipulator and sample holder which are used in order to align the sample with the beam spot and to manipulate its orientation. The collimated x - rays from the tube pass the detector through a centered hole and gets scattered by the sample. The diffraction image is taken by the detector in back scattering geometry. A typical Laue experiment involves the positioning of the sample on the goniometer, adjusting the x - ray beam and data acquisition and data analysis. Fig 2.16 shows a representative Laue pattern obtained in a sample of $\text{Ca}_3\text{Ru}_2\text{O}_7$.

The symmetry of the Laue pattern corresponds to the symmetry of the crystal, and directions of the crystal axes are determined by the symmetry axes of the Laue pattern. The Laue pattern of a crystal oriented along a high symmetry axis enables the identification of symmetry and all the spots. Here the sample is aligned with the c - axis parallel to the x - ray beam. The Laue spots will lie on a series of

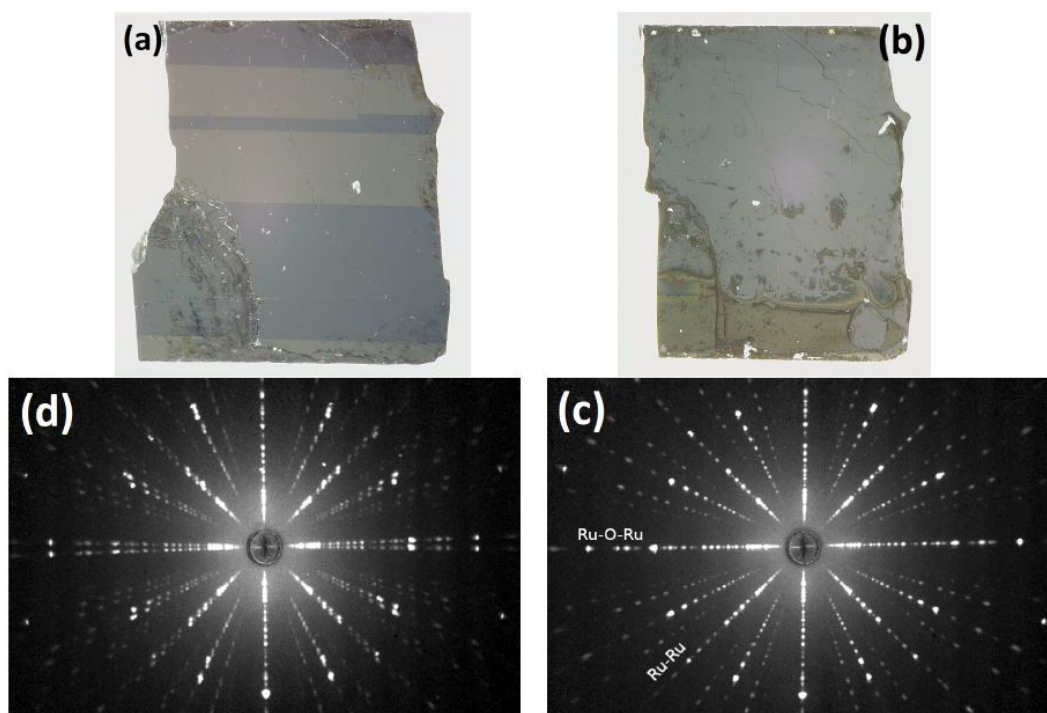


Fig. 2.17 (a) and (b) shows the polarised light image of the crystal sample $\text{Ca}_3\text{Ru}_2\text{O}_7$, that shows a clear change in domain distribution before and after the uniaxial pressure induced detwinning process. (d) and (c) shows the associated Laue pattern. Taken from Ref. [107]

lines passing through the point where the x-ray beam crossed the photograph and the lines form a symmetric pattern. To have the sample orientation in other high symmetry directions, PSL viewer software can be used to simulate the expected patterns for a given space group (shown in Fig 2.16 (b)). The sample is then rotated until agreement between the calculated and observed patterns is obtained. The Laue diffraction pattern shown in the figure can also be used to distinguish the Ru-O direction and the Ru-Ru directions by comparing the angles between lines. The horizontal and vertical directions correspond to the Ru-O directions, while the diagonals correspond to the Ru-Ru directions.

2.5.2 Detwinning

Twinning in a crystal refers to a phenomena where different domains join together in a crystal with axes close to each other resulting in an aggregate bulk crystal constituting of internal single crystals in various different configurations. Twinning is an important factor that hinders understanding of various physical properties of the crystal, its crystal structure determination etc... The anisotropy in resistivity

is an important measurement probe that helps in understanding the presence of broken rotational symmetries and the nature and origin of phase transitions that causes the effect. Hence the motivation to study detwinned crystals is of prime importance to study in detail the properties along crystallographic a or b directions. The mono - domain sample $\text{Ca}_3\text{Ru}_2\text{O}_7$ discussed in this thesis was prepared by detwinning achieved through thermomechanical means. The multidomain crystals were subjected to uniaxial pressure with the simultaneous application of heat causing the domains that are unfavorably arranged to be absorbed by favorably arranged ones [109]. The process of detwinning was observed through a polarising light microscope (PLM) in situ and the samples before and after the detwinning process were characterised using Laue diffraction [107, 110]. The Figs 2.17 (a) and (d) shows the PLM image of the domains before detwinning process and the associated Laue pattern.

The twinned crystal sample is placed between the ceramic holders of the detwinner in a nitrogen atmosphere. A modified solder iron which serves as a heating element is used to heat the sample to high temperature (around 495°C). Pressure was progressively applied while simultaneously observing the domains under polarised light. With an applied pressure of around 100 MPa, it was observed that one set of predominant domain population was achieved and the crystal was successfully detwinned. The sample was then cooled down without pressure to room temperature and Laue photograph was taken and compared to the twinned pattern as shown in Figs 2.17 (b) and (c). The measurements of in plane resistivity were then performed on the detwinned crystals using standard four probe method.

Chapter 3

RIXS study on Ca_2RuO_4

3.1 Introduction

The quasi 2-dimensional Mott transition system $\text{Ca}_{2-x}\text{Sr}_x\text{RuO}_4$ displays a rich array of interesting properties, including unconventional superconductivity, Hund's coupling physics [52], series of electronic, structure and magnetic transitions including paramagnetic metal, antiferromagnetic insulator, and paramagnetic insulator phases [111, 112] and has been the subject of intense studies for more than two decades [111].

With the discovery of superconductivity in cuprates, there has been a spur of interest in understanding the Mott-Hubbard metal insulator transition in these quasi 2D systems. In the simplest picture the metal - insulator transition depends on the ratio between the onsite Coulomb interaction U and the one-electron bandwidth, W . Increase in the U/W ratio facilitates a splitting between the upper and lower Hubbard bands with $U/W = 1$ resulting in a Mott-Hubbard band gap [24]. Fig 3.1 shows the schematic density of states function for the metallic Sr_2RuO_4 and the Mott insulating Ca_2RuO_4 .

A priori, due to the highly extended d shells of $4d$ and $5d$ transition metal cations in transition metal oxides (TMO), a weaker intra atomic Coulomb interaction and hence less correlation effects are to be expected in comparison to the $3d$ - TMO. In the Mott-Hubbard picture this points towards a metallic behaviour. However the large radial extension of the orbitals also results in a robust interaction between the Ru orbitals and the nearest neighbour oxygen orbitals which results in crystal structures that are distorted from the ideal case of the K_2NiF_4 type. The M-O-M bond angle in such cases is less than the ideal 180° and generally implies an insulating type behaviour due to narrowing d - electron bandwidth resulting in localisation and enhanced correlation effects. Thus in these systems there exists a delicate balance between two mechanisms - one which favors an itin-

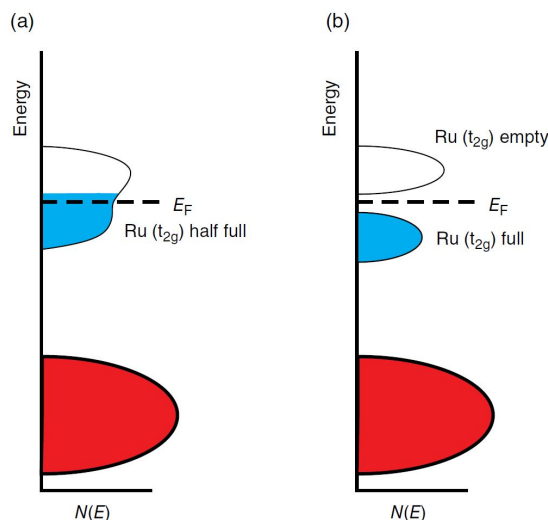


Fig. 3.1 Schematic density of states function for (a) metallic Sr_2RuO_4 and (b) the Mott insulator Ca_2RuO_4 . The Fermi level, which lies within the t_{2g} band in Sr_2RuO_4 , is now situated in the band gap in Ca_2RuO_4 resulting in an insulating ground state. Taken from Ref. [113]

erant and the other a localised physics. As a result these materials lie precariously on the boundary between metal- insulator transitions and slight perturbations like change in crystal structure, doping etc... can cause pronounced changes in physical properties [50, 114, 115].

The single - layered ruthenates exhibits a rich and complicated phase diagram as shown in Fig 3.2 [2, 111] with the isovalent substitution of Ca with Sr resulting in a systematic modification of crystal structure due to their different ionic radii, leading to a dramatic variation and evolution of properties from an antiferromagnetic insulating state to a superconducting state. The $x = 2$ end member – Sr_2RuO_4 is the poster child for unconventional superconductivity and $x = 0$ end member – Ca_2RuO_4 (Ca214) is an antiferromagnetic insulator which turns metallic at $T = 356$ K [7].

Among the layered ruthenates, Ca214 has gained a lot of attention due to its complicated electronic structure. Ca214 has a crystal structure derived from K_2NiF_4 type and belongs to the orthorhombic spacegroup - $Pbca$ with lattice parameters $a = 5.4097 \text{ \AA}$, $b = 5.4924 \text{ \AA}$ and $c = 11.9613 \text{ \AA}$ [7, 115]. The layered perovskite structure comprises of RuO layers stacked together with corner sharing RuO_6 octahedra. Compared to Sr_2RuO_4 , the structure is severely distorted due to the small ionic radius of Ca^{2+} , with rotation of the RuO_6 octahedra around the crystallographic c axis and a tilt around an axis in the RuO_2 plane [7]. Ca214 undergoes a paramagnetic metal insulator transition from a high temperature tetragonal near metallic phase to a low temperature orthorhombic Mott insulating phase

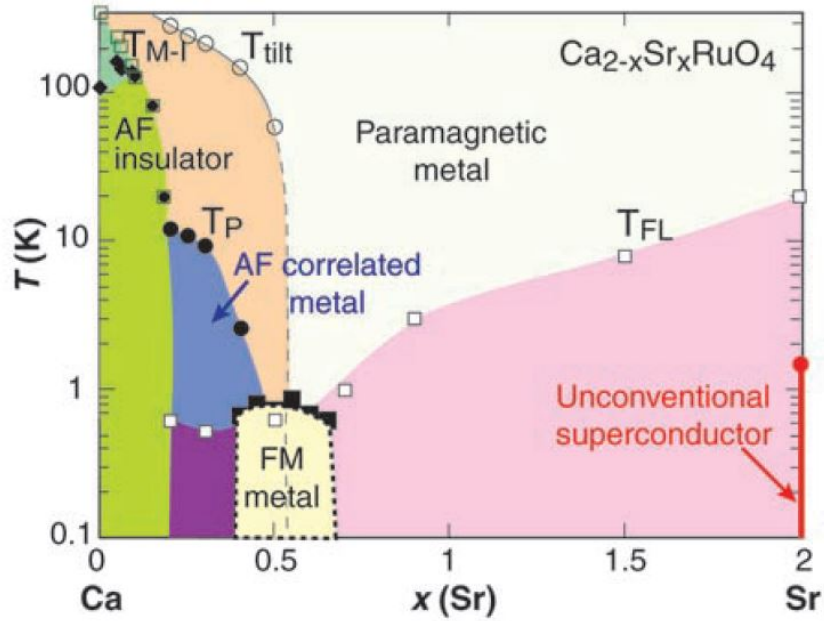


Fig. 3.2 Phase diagram of single layered ruthenates. The $x = 0$ endmember is an insulator which turns metallic at 356 K and the $x = 2$ endmember exhibits superconductivity below 1.5 K . Taken from Ref. [2]

at $T_{MI} = 360$ K which is accompanied by structural distortions and a reduction in the c - axis lattice parameter at $T_s = 356$ K with the long and short axes structures dubbed as $L-Pbca$ and $S-Pbca$ respectively [50]. Antiferromagnetic Néel ordering sets below temperature $T_N = 110$ K. Ca214 is a Mott- hubbard type insulator where the antiferromagnetic ordering sets in at a temperature $T_N (= 110$ K) $\ll T_{MI} (= 356$ K). This is an archetype of a metal insulator transition that is coupled to structural transition and not driven by AFM exchange interactions.

The low energy electronic properties of the layered Ca_2RuO_4 system is determined by its formal oxidation state of +4 - i.e the the number of electrons every Ru ion has in the $4d$ shell. The tetragonal crystal field effect, which is stronger in the $4d$ TMO's owing to the larger extension of the $4d$ shell as discussed before, splits the initial degeneracy of the Ru $4d$ orbitals into a low energy t_{2g} triplet and a high energy e_g doublet. With the effect of crystal field splitting larger than Hund's coupling, a low spin state is resulted and thus the filling of the lower lying t_{2g} states precedes that of the higher energy e_g doublet states, resulting in a two-third filled t_{2g} triplet ground state ($t_{2g}^4 e_g^0$ electronic configuration). With the localised $4d$ electrons, the Ca214 is an ideal for studying the interplay between spin and orbital degrees of freedom thereby providing new routes towards understanding their role in the unconventional superconductivity observed in the layered ruthenates.

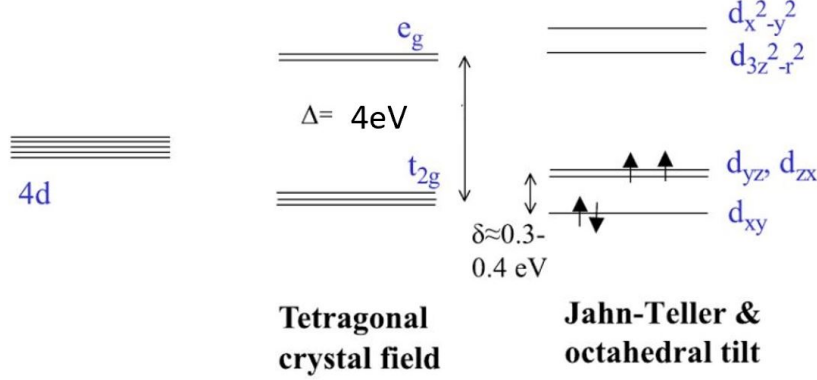


Fig. 3.3 Schematic illustration of the $4d$ electronic states of Ca_2RuO_4 . The initial degeneracy is lifted due to crystal field splitting resulting in lower t_{2g} and upper e_g bands and then the distortions of the RuO_6 octahedra further splits the t_{2g} states. Taken from Ref. [7]

Band structure calculations have estimated the energy difference between the triplet and the doublet sector to be around 4 meV. The Jahn Teller like distortion and the titling of the RuO_6 octahedra results in an additional splitting of the t_{2g} states with the d_{xy} states slightly lower in energy than the $d_{xz/yz}$ states (0.3 – 0.4) eV, [7, 116] a schematic depiction of which is shown in Fig 3.3.

Although the metal insulator transition in the system has been attributed to strong correlations and Mott type mechanism, several conflicting scenarios have been proposed regarding the nature of this transition and orbital occupancy in various works. [27, 117–119]. In one of the scenarios presented- called the Orbital Selective Mott Transition (OSMT) - it was suggested that the OSMT takes place in the narrower nearly one dimensional $d_{xz/yz}$ orbitals where the electrons undergo a Mott transition and become localised whereas electrons in the wider two dimensional d_{xy} are itinerant and the electronic band remains metallic [120]. In the second case, a single Mott transition was predicted which showed that the combination of crystal field splitting and on-site Coulomb interactions leads to complete filling of the d_{xy} band and a Mott transition in the half-filled $d_{xz/yz}$ bands. These were challenged by LDA+U study which proposed yet another scenario where it was predicted that the spin coupling enhanced by Coulomb interaction leads to the insulating phase. ARPES studies also showed conflicting results with the data from Neupane *et al.* [117] pointing towards an orbital selective picture in the $x = 0.2$ single - layered system of $\text{Ca}_{1.8}\text{Sr}_{0.2}\text{RuO}_4$ while other ARPES experiments reported by [121] showed three metallic bands and no OSMT. LDA and DMFT by Pavarini *et al.* [27] showed that the transition is driven by change in crystal

structure from L - $Pbca$ to S - $Pbca$ that reduces the bandwidth. This leads to an enhanced crystal field splitting with no orbital ordering in the metallic phase and with the complete filling of the lower energy orbital d_{xy} in the insulating phase S - $Pbca$. ARPES measurements by Sutter *et al.* [52] for the insulating phase are in agreement with the above mentioned LDA, DMFT calculations. The results were interpreted in favor of a band-Mott insulating ground state driven by Hund's coupling. The band-Mott scenario is triggered by a crystal field that renders the d_{xy} orbital band insulating with the half filled $d_{xz/yz}$ bands undergoing Mott transition driven by Coulomb interaction. The recent work by Zhang *et al.* [112] using LDA+DMFT approach confirmed that the Mott transition is indeed driven by the structural change from L - $Pbca$ to S - $Pbca$, where the magnetic ordering and Coulomb interaction play a role in determining the size of the gap in the xy orbitally ordered S - $Pbca$ insulating phase. The rich and myriad phenomenology of Ca214 is thus attributed to the interplay between various energy scales - the Coulomb interaction U , Hund's coupling J_H , crystal field splitting δ and spin-orbit coupling λ .

In this chapter a high resolution oxygen K - edge RIXS study of the antiferromagnetic Mott insulating state of Ca214 is presented. The possibility to detect Ru- d orbitals through the oxygen K - edge is utilised here and the light polarization analysis of XAS and RIXS spectra provides direct characterization the Mott-active ruthenium orbitals. The results obtained strongly support the band - Mott scenario discussed before. Applying high resolution RIXS, we report for the first time a dispersive low energy excitation of entangled orbital and spin degrees of freedom. A set of low energy excitations at 80 meV and 400 meV and higher energy excitations at 1.3 and 2.2 eV has been observed in our study. The high energy excitations are closely linked to Hund's energy scale and the low-energy electronic excitations of Ca_2RuO_4 have been interpreted using the theoretical framework proposed by Kim *et al.* [122]. This study by Kim *et al.* derived general expression for the RIXS crosssection for magnetic insulators in which both spin and orbital degrees of freedom are active and reside in the orbitals of t_{2g} symmetry in the strong spin orbit coupling limit. Similar studies using ARPES, optical conductivity, and x - ray absorption spectroscopy (XAS) and first - principles band calculations have been done in $5d$ TMO - Sr_2IrO_4 and manifestation of a Mott ground state defined by an effective angular momentum $J_{eff} = 1/2$ under a strong SOC and large crystal field effects have been reported [123] For Ca_2RuO_4 , with modest spin-orbit coupling strength, studies of the spin excitations have been interpreted as evidence for a similar composite $J_{eff} = 1$ quasiparticle. Our theoretical analysis reveals how this collective orbital excitation is intimately linked to the spin-excitation (including the Higgs) modes reported in the inelastic neutron

scattering and Raman studies [36, 37]. Both spin and orbital excitations originate from the same composite spin - orbit entangled quasiparticle. Our results provides a unification of the band-Mott insulator scenario and the Higg mode picture of Ca_2RuO_4 . Conceptually, this classifies Ca_2RuO_4 as a unique orbitally entangled Mott insulator.

However, in our measurements, the full manifold of the low-lying spinorbital excitations of Ca_2RuO_4 was not observed as direct L -edge RIXS was not available for high-resolution measurements during the time of this study. The recent studies using $\text{Ru-}L_3$ edge on Ca_2RuO_4 [61] has reported various excitations in the system: magnetic excitations at 50 meV consistent with the INS and Raman studies, SOC driven excitations at 320 meV in reasonable agreement with our work, Hund's driven excitations at 750 and 1000 meV- which likely due to lower intensities, appeared in our measurement as a broader peak around 1.3 eV and at higher energies around 2-4 eV the excitations from t_{2g} to higher e_g states.

3.2 Methods

High quality single crystals of Ca_2RuO_4 were grown by floating zone techniques [124, 125]. Crystals were aligned ex-situ using x - ray Laue technique and cleaved in-situ using top-post method. XAS and RIXS measurements were carried out at the ADDRESS beamline of the Swiss Light Source(SLS) at Paul Scherrer Institute. Before the low energy excitation spectrum can be measured by RIXS, XAS study - an element specific technique is carried out that consists of irradiating the sample with x - rays and measuring the absorption. Here, the energy of the incoming photon beam is tuned to an absorption edge. In this measurement the incident photon energy is tuned to resonate with the oxygen K - edge.(~530eV)

The experimental scattering geometry is schematically depicted in Fig 3.4 (a). A fixed angle of 130° was used between incident and scattered light. Given the quasi 2D nature of Ca_2RuO_4 system, only the planar component of the momentum $Q_{\parallel} = (h, k)$ involved in the RIXS process is considered. The in-plane momentum is varied by controlling the incident photon angle θ as shown in Fig 3.4. The reciprocal space is indexed in tetragonal notation. Grazing and normal incidence conditions refer to $\theta \approx 90^\circ$ and 0° respectively. The absorption spectra was taken in total fluorescence yield mode. Linear Vertical (LV) and Linear Horizontal (LH) polarisations are used to probe the oxygen K - edge at which an energy resolution of 29meV (half width at half maximum) was obtained. Elastic scattering throughout this work has been modelled by Voigt line shape allowing subtraction of this component. The presented data has been collected at $T = 16$ K unless otherwise specified.

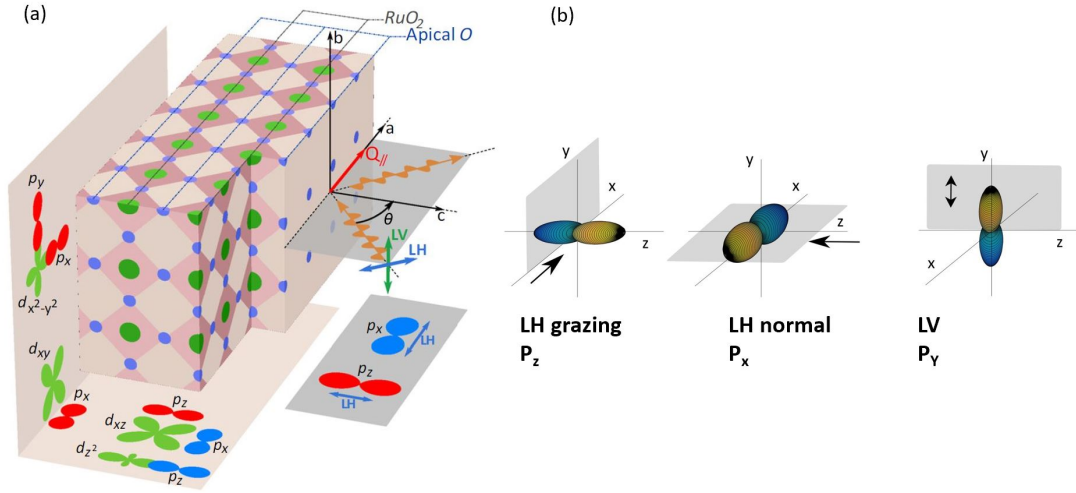


Fig. 3.4 Schematic depiction of RIXS geometry with respect to the crystal lattice of Ca_2RuO_4 . Ruthenium and oxygen sites are shown with filled green and blue circles respectively. The variable incident angle θ is defined with respect to the RuO_2 and apical oxygen planes. Using LV and LH polarized light, for different θ , sensitivity to either oxygen p_x , p_y , or p_z orbitals can be achieved. These oxygen orbitals in turn hybridize with different unoccupied t_{2g} and e_g states on the ruthenium site. (b) Schematic illustration of activation of different O- p orbitals by varying the polarisation and incident angle. With LH, grazing condition $\theta = 90^\circ$ results in the promotion of core hole from oxygen- $1s$ to $2p_z$ valence state. Similarly for LH normal incidence $\theta = 0^\circ$ the p_x orbital is activated and the LV polarisation results in the activation of p_y orbital.

3.3 Results

Here, the results on the combined XAS and RIXS study on Ca_2RuO_4 are presented.

The incident light polarisation $\vec{\varepsilon}$ is varied from horizontal LH with $\vec{\varepsilon} \parallel ac$ plane to vertical LV with $\vec{\varepsilon} \parallel b$ -axis. Due to the dipole selection rules, LH polarisation induces oxygen $1s \rightarrow \text{O } 2p_{x/z}$ excitations and the the LV induces exclusively Oxygen $1s \rightarrow \text{O } 2p_y$ transitions. Thus by changing the polarisation of the incident light from horizontal to vertical different orbital symmetries are probed [126] as shown in Fig 3.4 (b).

Fig 3.5(a) shows XAS spectra recorded with LH photon polarisation for near grazing and normal incidence conditions. A linear background is subtracted by fitting the flat region at energies lower than 528 eV and the spectra is then normalized using the high energy region. A good agreement is obtained with previous works when there is an overlap in temperature, light polarisation and incident light conditions. [31, 126, 127].

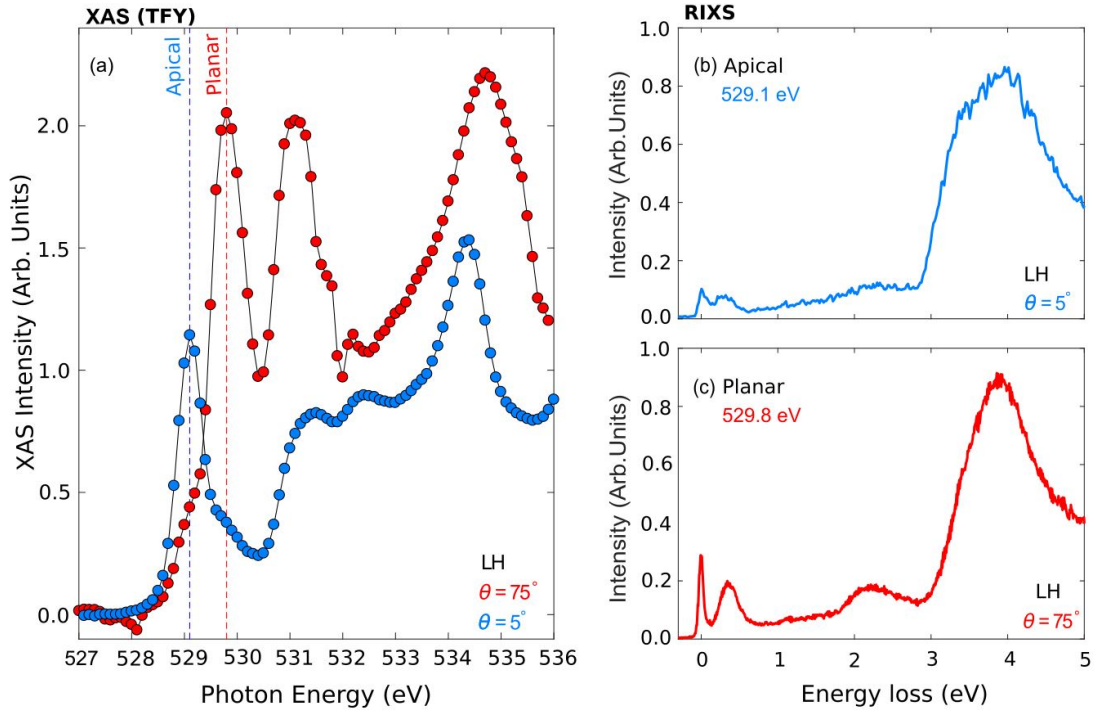


Fig. 3.5 (a) Background-subtracted x - ray absorption spectra recorded with linear horizontal light for near grazing and normal incident light conditions with settings that optimize either the apical or planar oxygen K - edge resonances as indicated by the dashed vertical lines. Panels (b) and (c) display representative RIXS spectra measured at the planar and apical oxygen K edges for LH polarisation.

In the fig 3.5 (a), the spectral features in the range 528 – 530 eV and from 530 – 536 eV are assigned to the transitions from O $1s$ core level to the O- $2p$ level that hybridise with Ru- $4d$ t_{2g} and e_g orbitals respectively and these assignments are supported by the band structure calculations for RuO_2 that has shown that the crystal field splitting between t_{2g} and e_g orbitals to be around 4 eV. [31, 126, 128, 129]. In the t_{2g} derived region pronounced angular dependence can be seen in the spectral features at 529.2 and 529.8 eV. Various previous studies have reported that the apical oxygen XAS peak is lower in energy than the in-plane one due to a difference in their core level binding energies- with apical resonance at energies less than the planar [128, 130], hence we can assign the features at 529.2 eV and 529.8 eV to transitions at the apical and planar oxygen sites, respectively. Once the absorption spectrum is recorded, the energy of the incident photon beam is set to an absorption edge (planar/apical) and RIXS measurements are performed.

Panels (b) and (c) of Figure 3.5 shows representative RIXS spectra with LH polarisation at apical and planar sites recorded at grazing and normal incidence. The spectra exhibit several excitations including the elastic scattering at zero

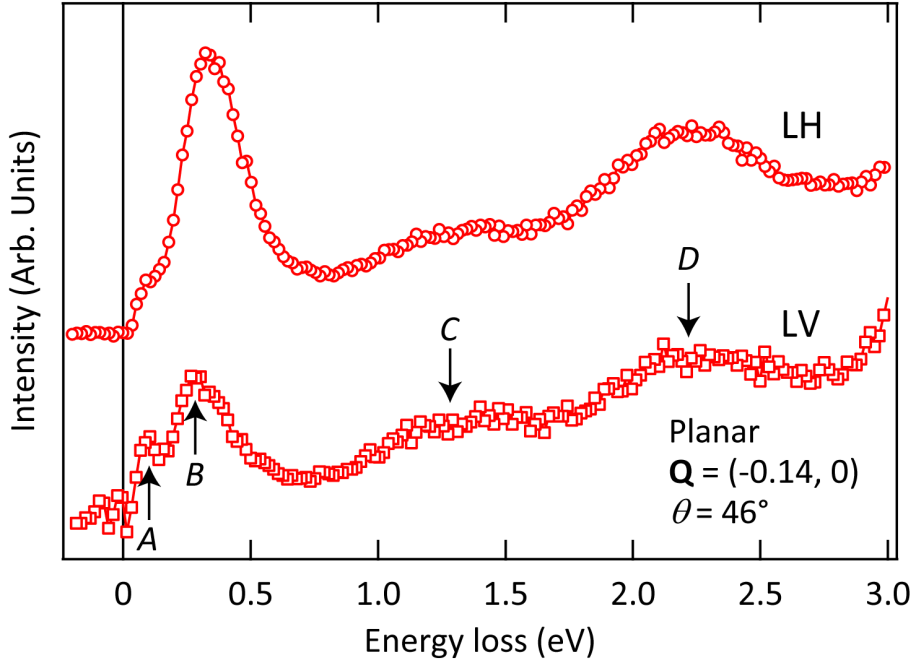


Fig. 3.6 Planar RIXS spectra, with elastic scattering subtracted and recorded with LH and LV light polarization for incident angle (momentum transfer) as indicated. Vertical arrows indicate the four excitations labeled A, B, C, and D. For clarity, the spectra are given an arbitrary vertical shift.

energy loss position and the dd excitations at 3–5 eV. The Fig 3.6 shows the RIXS spectra with planar oxygen resonance recorded with LH and LV polarisations for a representative incident angle. Four distinct excitations labelled A,B,C and D are seen with approximate energy losses of 0.08 eV, 0.4 eV, 1.3 eV and 2.2 eV respectively.

The excitation dubbed B observed at 0.4 eV is consistent with the previously reported study done by Fatuzzo *et al.* [129]. The amplitude of these excitations are strongly incident light angle and polarisation dependent. As seen in the panels (b) and (c) of Fig 3.5 and (c) and (d) panels of Fig 3.7, these matrix elements are different on the apical and planar resonance. Hence all four excitations are not necessarily clearly visible in a single spectrum.

From Fig 3.7, at first glance, one can see that the excitations dubbed - B and D are the most intense and prominent features of the spectra. These excitations show a distinct and pronounced dependence on polarisation for grazing incidence condition which can be seen in panels (c) and (d). Furthermore, one can see that with LH polarisation on the planar oxygen K - edge resonance these excitations are

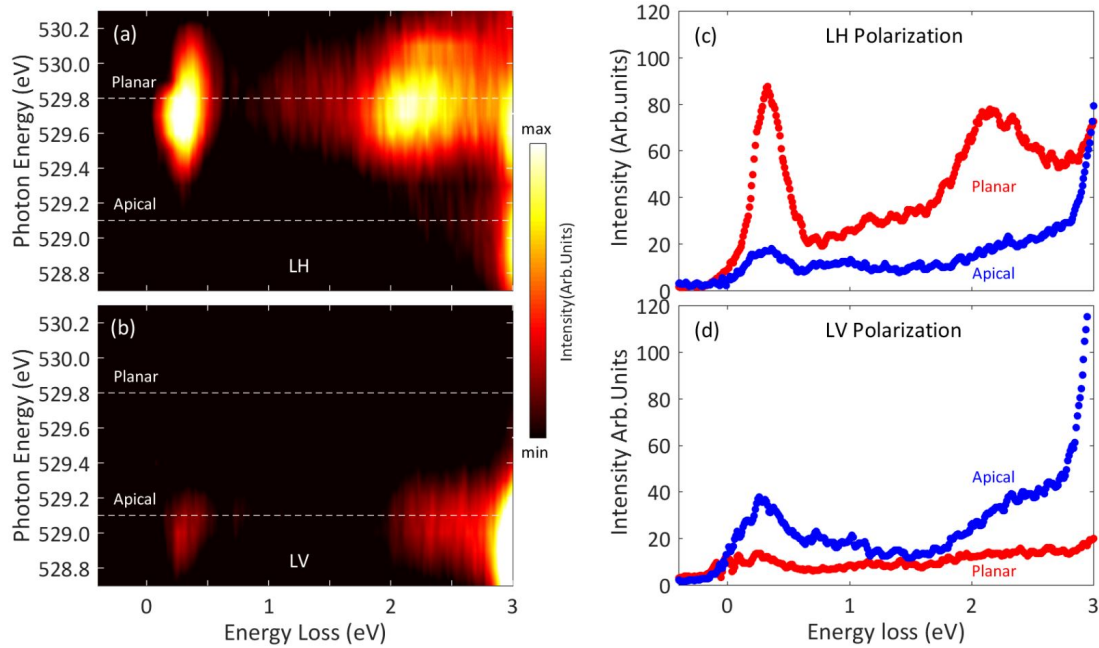


Fig. 3.7 Polarization dependence of the RIXS spectra versus incident photon energy. Panels (a,b) show RIXS response, in a false color map, as a function of energy loss and incident photon energy of LH and LV light polarization for the grazing incidence condition, as indicated. Horizontal dashed lines show the positions of the apical and planar resonances obtained from XAS. Panels (c,d) shows the RIXS spectra, with the elastic response subtracted, at the apical (blue lines) and planar (red lines) oxygen resonances for the respective light polarizations.

quite intense, but with varying the polarisation from LH to LV they are virtually "switched off". For the apical resonance an opposite dependence on polarisation is observed- with the excitations more prominent with LV and "switched off" for LH condition.

Fig 3.8 (a) shows a zoom in on the low energy excitations A and B recorded with LH and LV polarisation at a representative angle between normal incidence and grazing condition. Several preliminary observations can be drawn from this. The excitation dubbed A is more visible with LV polarisation. Under LH polarisation, the A excitation is barely resolvable but appears clearly in the LV polarisation condition for planar resonance. For apical condition, shown in Fig 3.8 (b), the peak A is visible in both LH and LV channels. The linewidth of excitation A is much smaller than peak B. The peak maximum and the line shape of the B excitation is strongly dependent on light polarisation as seen in Fig 3.8 (a). The peak C is more visible with LV polarisation as is evident from Fig 3.6. The D excitation shows an opposite trend where it is more pronounced in the grazing incidence LH

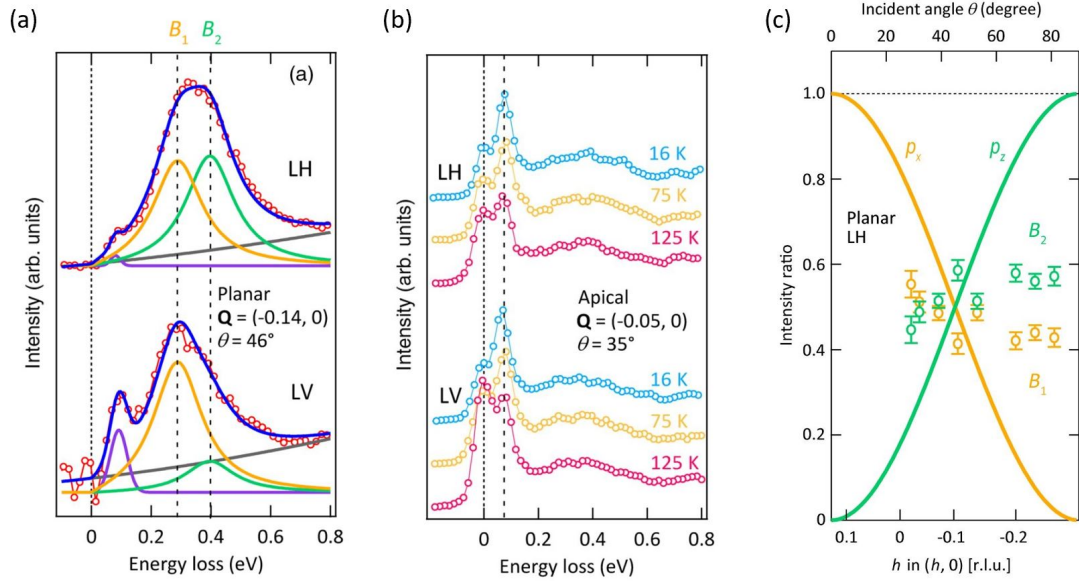


Fig. 3.8 (a) A zoom in on the low energy excitations of the spectra. Solid blue lines are a four-component fit, including a smoothly growing background (gray lines—second-order polynomial form), the 80-meV excitation (purple line—Gaussian line shape), and two modes with damped harmonic oscillator line shape [131–133] labelled B_1 (yellow) and B_2 (green) for the excitation at 400 meV. The peak position and width of the internal sectors B_1 and B_2 are presumed to be identical for LV and LH polarization. Peak amplitudes are left as open fit parameters irrespectively of light polarization. (b) Temperature evolution of RIXS spectra for apical resonance recorded with LH and LV polarization as indicated. The dashed lines are guides to the eye. (c) Peak amplitudes of the assumed internal modes of the B excitation - B_1 (yellow) and B_2 (green) extracted from fits (with fixed peak widths and positions). Corresponding solid cosine squared lines indicate, for LH polarisation, the expected coupling to the p_x and p_z oxygen orbitals.

polarisation and weaker in the LV channel. The temperature dependence of the A and B excitations (Fig 3.8 (b)) shows that they persist in to the high temperature paramagnetic phase.

The momentum dependence — along the $(h, 0)$ (Ru-O bond) direction-of the planar spectra recorded with LH polarization is shown in Fig 3.9 (a). The peak maximum position, extracted from fitting the derivative of the spectra, reveals a weak momentum dependence for the B excitation, consistent with its propogating/dispersive nature. The extracted momentum dispersion of the B excitation is reported in Fig 3.9 (b) with a minimum at the zone center. In contrast, the A excitation showed no discernible dispersion within the applied energy resolution. For completeness, the RIXS data are compared with the amplitude spin excitation mode reported by INS [36]

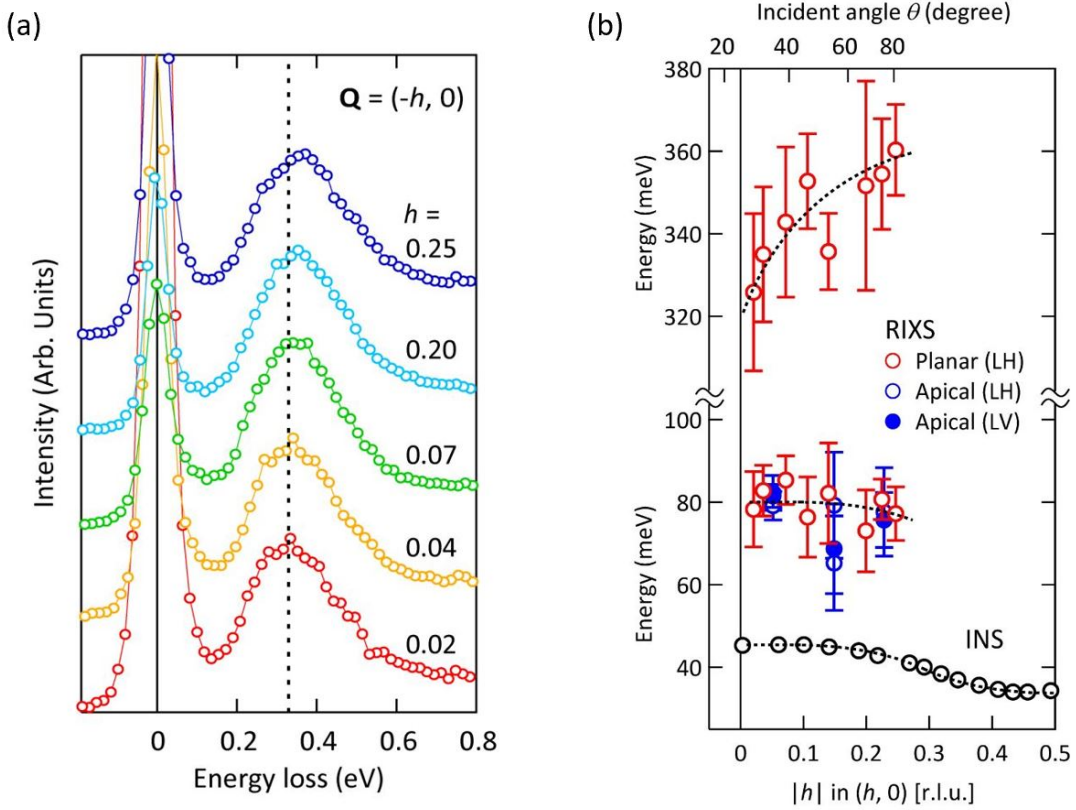


Fig. 3.9 (a) The in plane momentum dependence of the RIXS spectra at planar resonance recorded with LH polarisation. The dashed lines are guides to the eye. (b) Extracted dispersion along the $Q = (h, 0)$ direction of the A and B excitations in meV. The dispersion is defined by the peak maxima, which in the case of the B excitation, is derived from a derivative of the spectra. Error bars indicate standard deviations 3σ and σ for the A and B, respectively. Comparison to the spin excitation branch observed by neutron scattering (reproduced from [36]) along the same direction is also shown. Dashed lines are guides to the eye.

3.4 Discussion and Analysis

As discussed before, several studies have been done and different theoretical models have been proposed to understand the nature of Mott insulating state in Ca_2RuO_4 . Some of these models have proposed that the crystal fields drive the d_{xy} states insulating and the Mott physics is induced on the resulting half-filled $d_{xz/yz}$ bands [27, 112, 118]. ARPES study on the paramagnetic Mott insulating state also supports this combined band-Mott scenario [52]. Our XAS and RIXS spectra strongly support the scenario of complete orbital polarisation with almost fully occupied d_{xy} orbital. As the XAS process involves - a core electron being excited to an empty state, it is a probe of the unoccupied part of the electronic

structure of the system [134]. When the d_{xy} orbital is almost completely filled, it is inaccessible to the XAS process. Therefore d_{xz} and d_{yz} are the main active t_{2g} states available for absorption. Our XAS results shown in Fig 3.5 are in perfect accordance with this picture. With the aid of the schematic shown in Fig 3.4 panel (b), one can understand how different orbital selectivity can be achieved by varying the polarisations of the impinging photon. This allows to select the oxygen site (planar/ apical) at which the promotion of $1s$ core electron to a $2p$ valence state occur which in - turn affects their hybridisation with Ru $4d$ orbitals at the different oxygen sites. For example near the grazing incident condition using LH polariza-tion, the core electron is promoted to the p_z oxygen orbital that, at the planar site, hybridizes with Ru- $d_{xz/yz}$. Indeed, a pronounced response can be observed at the planar oxygen K - edge resonance while the apical oxygen contribution is strongly suppressed. With the same polarisation, when the incident angle is changed from grazing to normal condition, the oxygen p_x orbital is activated which hybridises with Ru- d_{xy} orbital at planar site and d_{xz} at the apical site. Correspondingly the XAS response shows a prominent peak at the apical resonance. Our XAS results thus suggest that the unoccupied t_{2g} sites have predominant $d_{xz/yz}$ character. The intensities of the RIXS spectra shows same trend as the XAS response (Fig 3.7). The excitations B and D are more pronounced in the grazing incidence condition for LH polarisation at the planar oxygen resonance where the oxygen hybridisation with the Ru $d_{xz/yz}$ orbitals are optimised. This leads to the conclusion that these excitations are intimately linked to the unoccupied $d_{xz/yz}$ states. The A excitation in contrast can be seen on both apical and planar resonances with both LH and LV polarisation (Figs 3.8 (a), (b)) which suggests that the orbital character of this excitation involves a mixture of d_{xy} and $d_{xz/yz}$ states.

To gain insight into the origin of the various features observed in the spectra, the polarisation dependent RIXS intensity at the oxygen K - edge is calculated by considering the cross section associated with the transition from the oxygen core $1s$ to $2p_k$ ($k = x, y, z$) level within the fast collision approximation [77, 135]. The generic amplitude of the cross section is expressed as

$$A(p_k) = \sum_{j \in O_p} \sum_{m, \sigma} \left| \langle m | p_{j,k,\sigma} p_{j,k,\sigma}^\dagger | 0 \rangle \right|^2 \delta[\omega - (E_m - E_0)] \quad (3.1)$$

where $p_{j,k,\sigma}^\dagger$ creates an electron with spin σ in the $2p_k$ orbital (where $k=x,y,z$) at the oxygen site j (planar/apical) and E_m and E_0 are the energies of the excited states $\langle m |$ and the ground state $|0\rangle$ respectively. To discuss the spectra presented in Fig 3.7, computation of RIXS crosssection of a Ru-O-Ru cluster is considered for which the spectra is determined by the exact diagonalisation of the Hamilto-

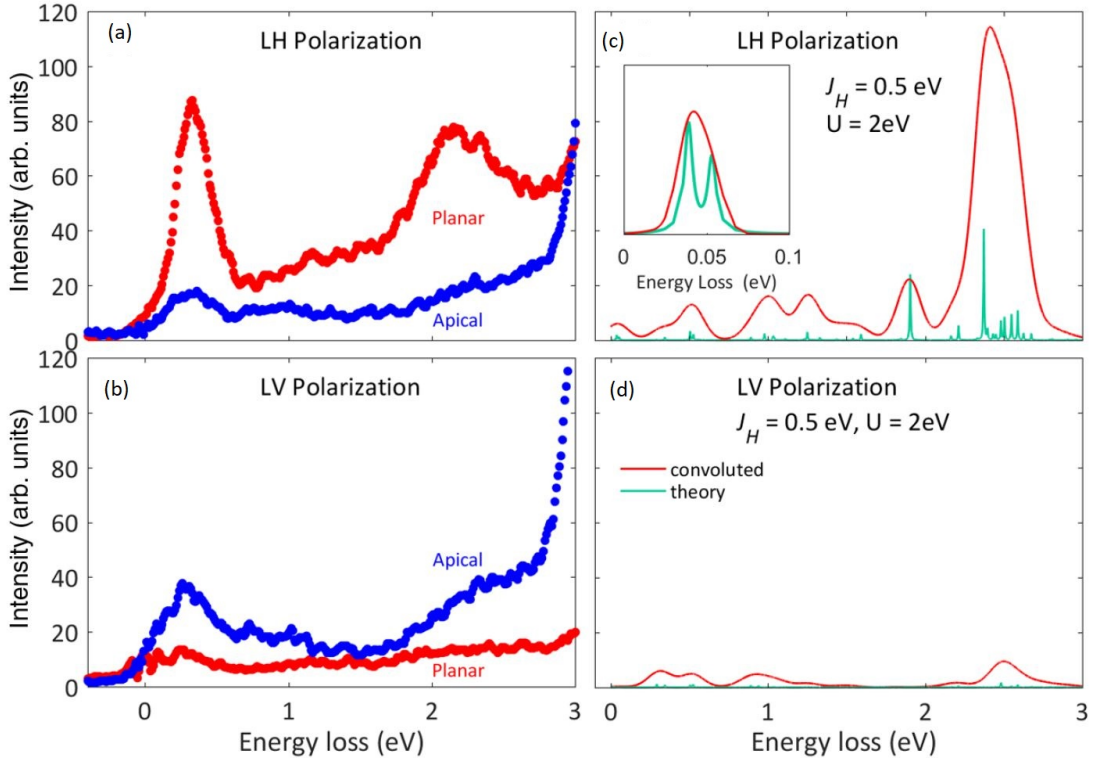


Fig. 3.10 Comparison of the experimental spectra shown in Fig 3.7 with the calculated RIXS spectra (panels(c)and (d)) for the planar site with respect to linear horizontal and vertical light polarization (see text for a detailed explanation of the model). Green lines indicate the expected excitations, and the solid red line is obtained by Gaussian convolution to mimic instrumental resolution. A standard deviation of $\sigma = 70$ meV was applied whereas $\sigma = 7$ meV was used for the inset, which displays a zoom on the lowest excitations at around 40 meV.

nian [136]. The local ruthenium Hamiltonian consists of three terms - (1) The spin orbit coupling λ , (2) total Coulomb interaction for the t_{2g} electrons which is expanded into intra orbital Coulomb interaction U and inter orbital electron-electron interaction set by $U - 5J_H/2$ where J_H is the Hund's coupling term. For a rotationally symmetric system the pair hopping term and the Hund's coupling are both of strength J_H , (3) tetragonal crystal field potential δ between the t_{2g} orbitals. To evaluate the model, material specific values $\delta = 0.3$ eV, $\lambda = 0.075$ eV, $U = 2$ eV and $J_H = 0.5$ eV are used [31, 129, 137]. These values are similar to those used in the DMFT calculations in the ARPES study by Sutter *et al.* [52]. The ratio of $\delta/2\lambda = 2$ is comparable to the values used in the inelastic neutron scattering study by Jain *et al.* [36].

Fig 3.10, panels (c) and (d) show the calculated RIXS spectra for planar oxygen sites for horizontal and vertical polarisations. The aim is to understand the

nature of the intermediate and high energy excitations in the experimental RIXS spectra vis-a-vis the role played by Coulomb interaction and Hund's coupling. Although qualitatively the model is not very sensitive to the exact set of parameters and the ratio of spectral weight between the low and high energy excitations for horizontal polarization is different from the data, the results presented in Fig 3.10 qualitatively reproduce the experimental spectra. In particular, the excitation at about 2.2 eV as well as the polarization dependence of the spectral weight. The spectra exhibits clear features at about 1 eV and 2 eV and these correspond to singlet to triplet transitions occurring at a single ruthenium site or at two neighbouring ruthenium sites set by energies $\sim 2J_H$ and $4J_H$ respectively. This provides an explanation for the possible origin of the observed C and D excitations in the experimental spectra. When Ru-O-Ru bond is considered, the configuration $d^5 - 2p^2 - d^3$ represent the lowest energy intermediate states that enter spin orbital exchange processes when the total number of doubly occupied orbitals at the Ru site are held fixed. The configurations of the type $d^6 - 2p^0$ and $d^5 - 2p^1$ represent the higher energy states [136].

To elucidate the nature of the low energy excitations, we focus on the d^4 electronic configuration at a single local Ru site. With 4 electrons in the Ru^{4+} state that fill the t_{2g} subspace, the local Ru configurations can be denoted as $|d^4; n_d = 1\rangle$ and $|d^4; n_d = 2\rangle$ where n_d denotes the number of doubly occupied orbitals- dubbed "doublons". In the $n_d = 2$ subspace, the states are doubly occupied and the electrons pair to form spin singlet configuration. In the $n_d = 1$ subspace the electrons in the doubly occupied site forms a singlet while the other 2 electrons can be in spin singlet/ triplet states. The eigen states of the local ruthenium Hamiltonian projected on the spin triplet subspace represent the low energy excitations within the $|d^4; n_d = 1\rangle$ sector.

Fig 3.11 (a) shows the evolution of the energy eigen values for the material specific value of tetragonal crystal field splitting $\delta = 0.3\text{eV}$ as a function of spin orbit coupling λ . The sector is made of 9 spin orbit entangled states grouped into two blocks . Based on the energy diagram, for vanishing spin orbit coupling i.e $\lambda = 0$, the blocks are three fold and six fold degenerate respectively. As seen in the energy spectrum, the 6-fold degenerate excitation sector (dubbed β) with a doublon in $d_{xz/yz}$ orbitals is separated from the ground state three fold degenerate sector (dubbed α) with the doublon in the d_{xy} orbital by an energy set by the crystal field splitting $\delta = 0.3$ eV. A Finite spin orbit coupling lifts the degeneracy of the sectors by introducing a splitting of about λ^2/δ and 2λ respectively and it mixes the orbitalcharacter of the doublon state and can be seen schematically depicted in Fig 3.11 (b).

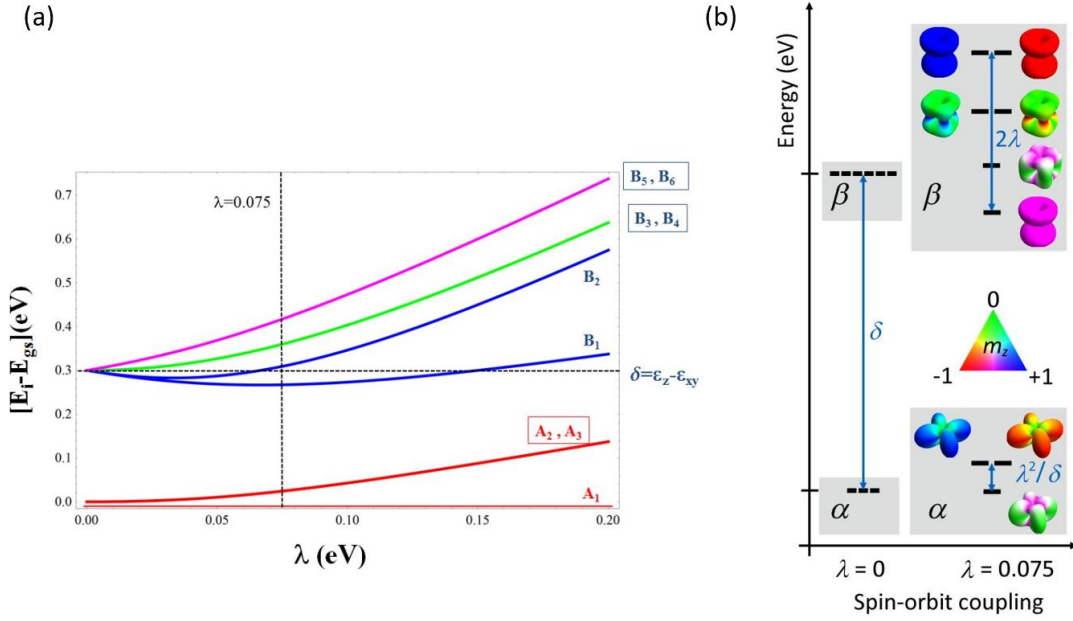


Fig. 3.11 (a) Energy spectrum of the $S = 1$ and one doublon $|d^4; n_d = 1\rangle$ of the local ruthenium Hamiltonian projected on the spin triplet subspace as a function of SO coupling λ , for a representative value of the tetragonal crystal field splitting $\delta = 0.3$ eV. The sector of the lowest energy levels are made of 9 spin orbit entangled states which are grouped into 2 distinct blocks. Taken from Ref. [136]. (b) Schematics of low-lying energy levels of an interacting model for a single ruthenium site for spin-orbit coupling λ set to zero (left) and to the material specific value of 0.075eV (right). With d^4 configuration, one of the $d_{xy/xz/yz}$ orbital is doubly occupied, and the other two singly occupied electrons are in a spin-triplet state. The degeneracies of the two sectors denoted by α and β are lifted by a finite spin-orbit coupling. The character of the doubly occupied orbital is displayed along with a color scale indicating the directional dependence of the total spin m_z moment.

The transitions within the α manifold at the Ruthenium site give rise to excitations around 50 meV range which has been studied using INS studies by Jain *et al.* [36] (reproduced in Fig 3.9 (b)). Raman scattering studies by Souliou *et al.* [37] revealed two excitations around 80 meV and associated them with two-Higgs and two-magnon scattering modes. The A excitation present in our spectra can hence be attributed to an excitation of magnetic origin. The calculated RIXS spectra (shown in Fig 3.10 panels (c) and (d)) show distinct excitations in the energy range at about ~ 40 meV. It can be assigned to the amplitude and phase excitations arising from the effective $J_{eff} = 1$ configurations in the α sector. Our cluster analysis, by construction, does not allow us to obtain multiple amplitude excitations associated with the interacting $J_{eff} = 1$. However, a two-scattering

mode (i.e., near 80 meV) is, in principle, expected and would emerge in a larger cluster calculation, eventually considering the RIXS cross section at the oxygen K edge beyond the fast collision approximation. The predicted 40 meV magnetic mode, observed by neutron scattering, should, in principle, also enter into the RIXS cross section. Although, it is not observed in our experiment because of the finite energy resolution, recent RIXS studied on the Ru L_3 -edge showed the presence of these magnetic excitations at around 50 meV consistent with the neutron and Raman scattering results [61].

The calculated spectra also shows a set of excitations in the range ~ 0.3 eV to 0.6 eV which arise from transitions between the α and β sectors at the Ru site depending only on the crystal field splitting and spin-orbit coupling. The low energy peak B observed at around ~ 400 meV in our RIXS spectra hence corresponds to a spin-orbit excitation. A recent RIXS study [61] has also observed this low energy spin-orbit driven excitation around 320 meV in reasonable agreement with this work. The broadness of the B excitation and its light polarisation dependence is interpreted as a consequence of the internal structure of the β sector. The Fig 3.8 (a) shows how the B peak can be fitted with two internal levels labelled B_1 and B_2 whose line widths and peak positions are kept fixed while peak amplitude is left as an open parameter. The fits thus describe the observed momentum and polarisation dependence. The internal peaks as shown in Fig 3.8 (a) show a drastic variation in amplitude with change in polarisation for a fixed incident angle (momentum transfer) which points towards the internal orbital structure of the B excitation. This broad peak observed in our RIXS study shows a marked difference to the sharp peak observed in the RIXS study on Sr_2IrO_4 , which was attributed to the presence of a propagating excitonic quasi particle in this strongly spin orbit coupled Mott insulator [138].

Matrix element effects can modulate the intrinsic intensities of the spectra depending on the experimental geometry, light polarisation and photon energy. The internal structure of the B excitation raises the need to clarify that this effect does not stem from matrix element effects.

When the incident photon angle—hence the momentum transfer—is varied with the same polarisation (here LH) as discussed before, it results in a switch between the different p orbitals of the oxygen (p_x and p_z for normal and grazing respectively). Fig 3.8 (c) shows the expected sensitivity to the p_z and p_x oxygen orbitals and the fitted peak amplitudes of the B_1 and B_2 internal levels. As they vary only weakly with momentum, the matrix element effect can be crossed out as a plausible explanation for the observed dispersion. We thus conclude that the dispersion

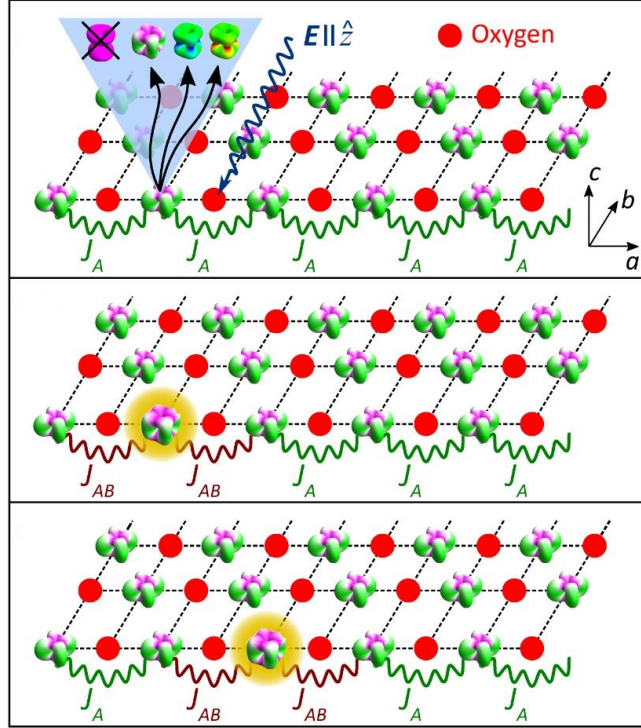


Fig. 3.12 Schematic of an oxygen K - edge RIXS process creating a local excitation between the α and β sectors and its subsequent propagation by second order exchange processes. The nearest-neighbor exchange couplings are denoted as J_A between sites in the α sector and J_{AB} between α and β sectors.

is intrinsic, which in turn indicates the itinerant nature of this sector.

The nature of the low energy excitations are hence related to the one doublon triplet states at a single Ru site in the α , β sector and as previously concluded, the RIXS process allows to have an excitation of B character at the Ru site. When charge hopping between ruthenium-ruthenium via oxygen sites are reinstated these local spin-orbit excitations can propagate via second order exchange processes with configuration $d^5 - d^3$ of the Ru- d orbitals of the neighbouring sites, schematically illustrated in Fig 3.12.

Within second-order perturbation theory, using the Ru-Ru hopping parameter, $t \sim 0.3$ eV from [27] an estimate of the band width of the spin orbit excitation is obtained in the range of ~ 30 - 40 meV at characteristic parameters defined earlier - $\lambda = 75$ meV, $U = 2.2$ eV, and $J_H = 0.4$ eV. It is furthermore expected that excitations in the α sector exhibit a weaker dispersion due to the smaller exchange amplitude between the $J_{eff} = 1$ modes. Our model thus qualitatively accounts for the fact that the B excitation disperses about 30 meV over half a zone, whereas

the A excitation, according to inelastic neutron scattering [36] as shown in Fig 3.9 (b), disperses no more than 20 meV over the entire zone.

3.5 Conclusions

To summarise, a comprehensive oxygen K - edge RIXS study has been carried out in the AFM phase of the Mott insulator Ca_2RuO_4 . The strong polarisation dependence of the signal evident in the XAS and consequently in the RIXS spectra has been interpreted as a direct manifestation of a band- Mott insulating nature of Ca_2RuO_4 . The varying polarisation and incident angle has been shown to activate different $O-p$ orbitals that hybridises primarily with $\text{Ru-}t_{2g}$ states $d_{xz/yz}$. The dispersive excitations observed at ~ 400 meV is shown to be driven by spin-orbit coupling. The spin-orbit coupling is also relevant for activating the high-energy (about 2.2 eV) nondispersive excitations by the RIXS process, achieved by local conversion of triplet into singlet states. For realistic values of crystal fields, Hund's coupling J_H , Coulomb interaction U , and SOC, all salient features of the RIXS spectra were captured with minimal theoretical modeling. Our results demonstrate that Ca_2RuO_4 is a Mott insulator with a paradigmatic competition between SOC and crystal-field energy scales. Combining RIXS data and theoretical modelling, we have unveiled how spin-orbital entangled excitations manifest within a spin-orbit-coupled band-Mott insulator. The recent study on Ca_2RuO_4 by Gretarsson *et al.* [61] using $\text{Ru-}L_3$ edge RIXS, have shown the presence of a peak at around 50 meV of magnetic origin attributed to transverse magnons and Higgs mode consistent with the Raman and INS studies [36, 37] (See Figure 3.13).

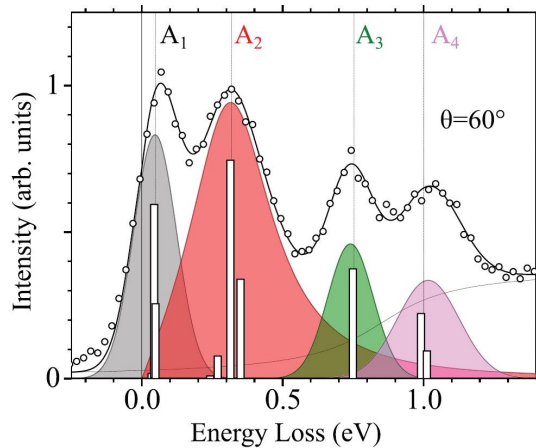


Fig. 3.13 RIXS spectrum of Ca_2RuO_4 at the $\text{Ru-}L_3$ edge (2838.5 eV) taken at $\theta = 60^\circ$ shows a four component spectral feature in the energy range between 0 to 1 eV. The fit shows features at energies 50meV, 320 meV, 750 meV and 1000meV. Taken from Ref: [61]

This study also detected the presence of Hund's rule driven spin state transitions at 0.75 eV and 1 eV which were not seen in our results, but which appeared rather as a broad peak at around 1.3 eV. Due to insufficient energy resolution these low energy modes could not be individually resolved. For future studies, it would be of great interest to further resolve the internal structure of the low-energy excitations. As synchrotrons are being upgraded for diffraction limited experiments, flux and resolution at the oxygen K edge will improve. In particular, enhanced energy resolution, in combination with the light polarization analysis put forward here, would allow us to study important information on different orbital characters of these excitations. With gains in energy resolution, the RIXS technique will enter further into the spin-excitation sector.

The results of this chapter have been published in: .Das, L., *et al.*. "Spin-Orbital Excitations in Ca_2RuO_4 Revealed by Resonant Inelastic x - ray Scattering." *Physical Review X* 8.1(2018) : 011048

Chapter 4

Magnetotransport study on $\text{Ca}_3\text{Ru}_2\text{O}_7$

4.1 Introduction

$\text{Ca}_3\text{Ru}_2\text{O}_7$ (CRO 327) is the $n = 2$ bilayer member of the Ruddleson-Popper series $\text{Ca}_{n+1}\text{Ru}_n\text{O}_{3n+1}$ [7]. It exhibits signature of metallic and semi-metallic phases and hosts a vast array of exotic properties including colossal magnetoresistance [15, 68, 139], Shubnikov-dehaas oscillations [15, 66, 140], spin valve effect [141], metamagnetic transition etc. The system also has been recently shown to have topological Hall effect stemming from non collinear spin structures [13].

The bilayer crystallises in the perovskite-like (shown in Fig 4.1) non - centrosymmetric orthorhombic polar-structure and belongs to the space group $Bb2_1m$ with $a = 0.5396$ nm, $b = 0.5545$ nm, and $c = 1.961$ nm. [67] The crystal structure, similar to its fellow members in the RP series, is distorted and the intriguing physical properties stem from the distortions and the tilting and rotation of the RuO octahedra. [7]

In zero magnetic field, the system undergoes a transition from paramagnetic metallic state to antiferromagnetic metallic state at Néel transition temperature $T_N = 56$ K defined as AFM-a state with ferromagnetic bilayers stacked antiferromagnetically along the crystallographic c axis with magnetic moments along a -axis. This is followed by a Mott like transition at 48 K with dramatic decrease in conductivity which is accompanied by a shortening of the c - axis lattice parameter. The magnetic moments now reorient along b - axis and the state is dubbed as AFM-b state. On cooling down the system further, the in-plane resistivity becomes metallic and the system regains the Fermi liquid behavior below 30 K. [67, 72] Recent ARPES measurements have shown that the $\text{Ca}_3\text{Ru}_2\text{O}_7$ is an electronically

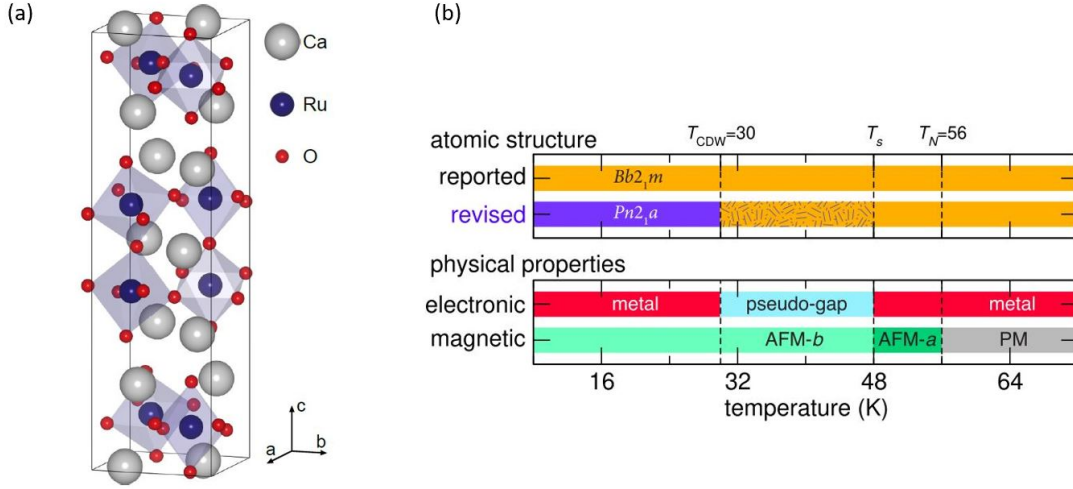


Fig. 4.1 (a) Crystal structure of $\text{Ca}_3\text{Ru}_2\text{O}_7$. Taken from Ref. [142]. (b) Low temperature phase diagram of CRO327. This study by Puggioni *et al.* assigned a charge (spin) density wave transition to $T_{CDW} = 30$ K, along with broken translational symmetry from ($Bb2_1m \rightarrow Pn2_1a$). Taken from Ref. [143]

driven Dirac semi metal at low temperature and has an anisotropic Fermi surface with small electron like pockets along the short a -axis and boomerang shaped Fermi surface sheets along long b -axis [14]. The system was shown to undergo a two phase reconstruction of the Fermi surface concomitant with the characteristic temperatures discussed above- at $T_s = 48$ K the electronic reconstruction appears and the system settles into low temperature structure below $T^* = 30$ K. The understanding of electronic structure of the CRO 327 system by various studies including the ARPES study mentioned above, the Quantum oscillation study by Kikugawa *et al.* [66] and transport measurements [72] have established the presence of both electron and hole pockets and a partial gap opening in the Fermi surface.

Ambipolar transport – combination of electron and hole carriers – is a commonly occurring theme in condensed matter physics and crucial in defining the transport properties of semimetals [144]. The evidence of both electron and hole like bands in CRO 327 at low temperatures enable us to analyse the results of our low temperature, low field magnetotransport measurements by utilising a two-band Drude model for conductivity. The model is then used as a prelude towards a more generalised analytical scheme for application to several other two-band systems.

With this study, we express ratio of carrier densities in terms of two dimensionless parameters dubbed α and β and variation of these quantities in the (α, β) phase space is used to seamlessly connect the compensated and monocarrier dominated regimes. If the densities of the carriers are known from ARPES or Quantum

Oscillation measurements, α and β can be determined from magnetotransport measurements.

In the following sections, a systematic study of magnetotransport measurements in the semimetallic phase of CRO 327 system has been done and a simple generalised analysis scheme involving (α, β) has been proposed as an easy and robust check for a system's compliance or the lack thereof with a two-band model.

4.2 Methods

High quality single crystals were grown by floating zone techniques [124, 125]. The crystals were detwinned, by pressing along an orthorhombic axis, using a thermo-mechanical detwinning device [110]. This is achieved by heating the sample to high temperature and progressively applying pressure while simultaneously observing the disappearance of multiple domains through a polarized microscope. The c -axis of the samples were determined by using Laue x - ray diffraction technique . The longitudinal resistivity, Hall, magnetization and thermal transport measurements were carried out using Four probe technique in the the Quantum Design Magnetic Property Measurement system and Physical Property Measurement System with magnetic field H applied along the crystallographic c -axis. Current and temperature gradient were applied along the orthorhombic b - axis (the longer lattice parameter) . Thermopower and Nernst measurements were done with the aid of a home built insert for the PPMS. The temperature gradient was created by using linear pattern high resistance strain gauge as a heater device and the gradient was held fixed about 2-3% of the base temperature. Calibrated Cernox thermometer chips at the hot and cold end of the sample were used to measure the gradient established. The current to create the desired thermal gradient across the sample was applied with Keithley precision current source and the longitudinal and transverse voltage that develop across the sample were measured with Keithley nanovoltmeters used in conjunction with home built nanaovolt amplifiers.

4.3 Results

Here we report the magnetotransport and thermoelectric measurements on the detwinned single crystal of $\text{Ca}_3\text{Ru}_2\text{O}_7$ with current applied parallel to b - axis and field along crystallographic c - axis. The information obtained from these measurements are then used as a starting point to probe the (α, β) phase space. The zero field longitudinal resistivity as a function of temperature is plotted in Fig 4.2 (a).

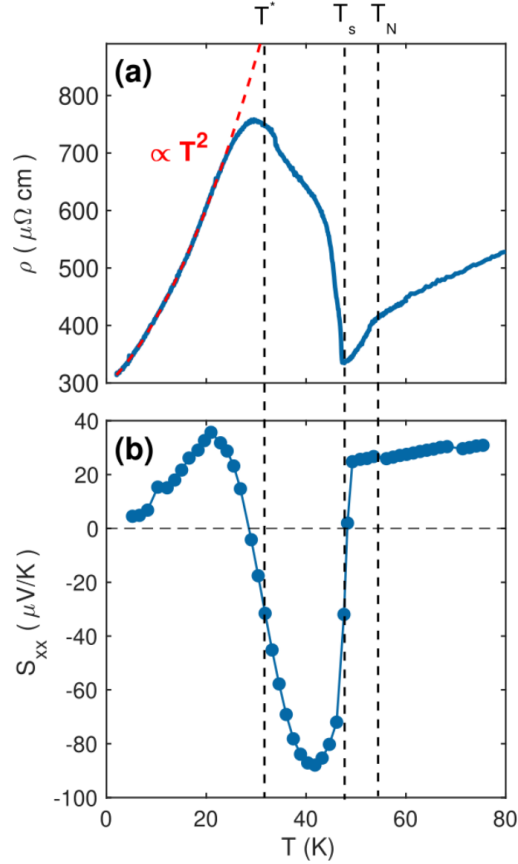


Fig. 4.2 (a) Resistivity ρ_{xx} as function of temperature T measured for zero field. The vertical dashed lines indicate the onset of AFM-a and AFM-b phases indicated by $T_N = 56$ K and $T_s = 48$ K respectively. (b) Zero field thermopower with $\nabla T \parallel b$

The resistivity curve shows signatures of the relevant transitions in the system. Three temperatures can be identified at first glance, as indicated in Fig 4.2 (a). At high temperatures the behavior is metallic. At $T_N = 56$ K the curve shows a sharp downward kink indicating the Néel transition from paramagnetic metal to an antiferromagnetic metal state dubbed AFM-a with magnetic moments aligned along the crystallographic a - axis. On further cooling at $T_s = 48$ K a structural transition occurs where the conductivity drops drastically. This is associated with a first order phase transition where the crystal structure remains unchanged, but has a compression of c axis lattice parameter and the reorientation of moments along the b axis – a state dubbed as AFM-b state [141]. At around 30 K another transition can be seen in the resistivity curve, which has been in a recent ARPES study, attributed to a concomitant Fermi surface reconstruction in the system [14]. Below 30 K, the system regains the metallic state and the resistiv-

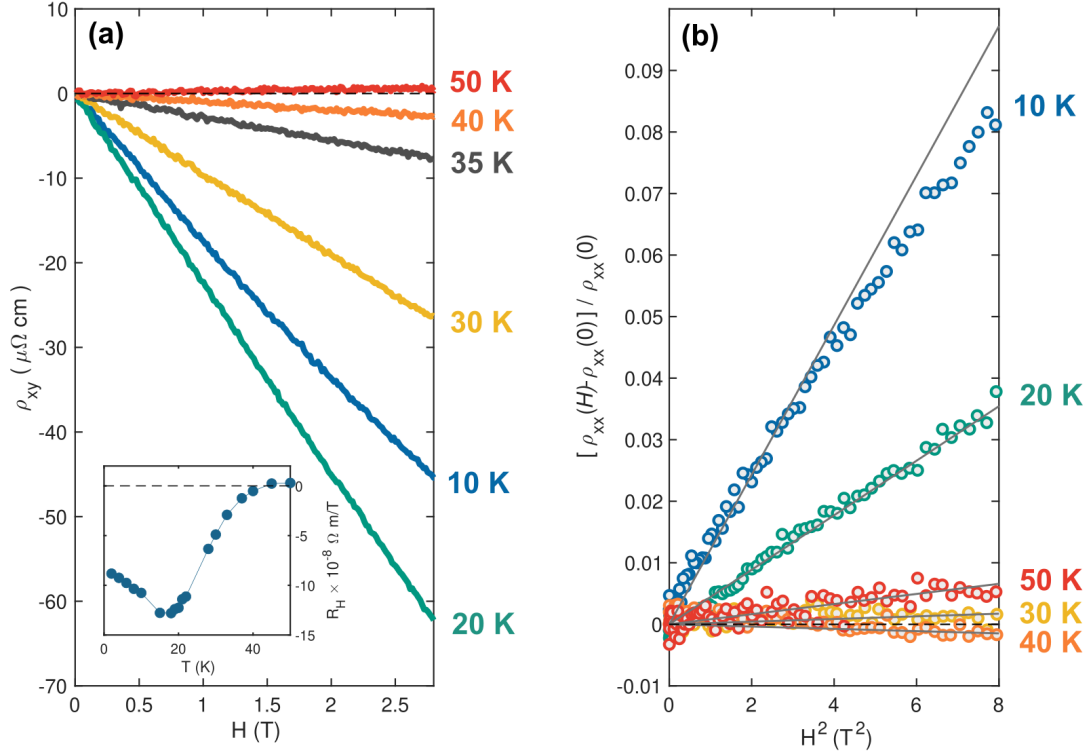


Fig. 4.3 (a) Hall isotherms versus field at some representative temperatures as indicated. Inset shows the low field Hall coefficient $R_H = \rho_{xy}/H$ (b) Magnetoresistance $(\rho_{xx}(H) - \rho_{xx}(0))/\rho_{xx}(0)$, as a function of H^2 for temperatures as indicated. Gray solid lines are linear fits.

ity correspondingly shows T^2 behavior characteristic of FL. Fig 4.2 (b) shows the thermopower measurement along b -axis and it closely follows the resistivity curve with the different characteristic temperatures clearly visible. Though the Néel transition cannot be seen in the thermopower curve, the structural transition at $T_s = 48$ K is signalled by a sharp sign change of seebeck coefficient. At 30 K there is another change in the sign from negative to positive of the Seebeck coefficient. These results are consistent with the results obtained by Xing *et al.* [72]

Fig 4.3 (a) shows the Hall isotherms for temperatures indicated and is consistent with the previous reports [72] with the Hall resistivity showing negative values for $T < T_s$. The magnetoresistance data plotted as $(\rho_{xx}(H) - \rho_{xx}(0))/\rho_{xx}(0)$ versus H^2 is shown in Fig 4.3 (b) at various representative temperatures. The low temperature MR and the calculated mobility, $\Delta\rho(H)/\rho(0) = (\mu H)^2$, which gives $\mu = 0.1T^{-1}$ agrees with the previous studies [66, 72]. The temperature dependence of the magnetoresistance shows an intriguing behavior (shown as a colorplot in Fig 4.4 (a)) with the field derivative of resistivity given by $(d\rho_{xx}/dH)$ exhibiting

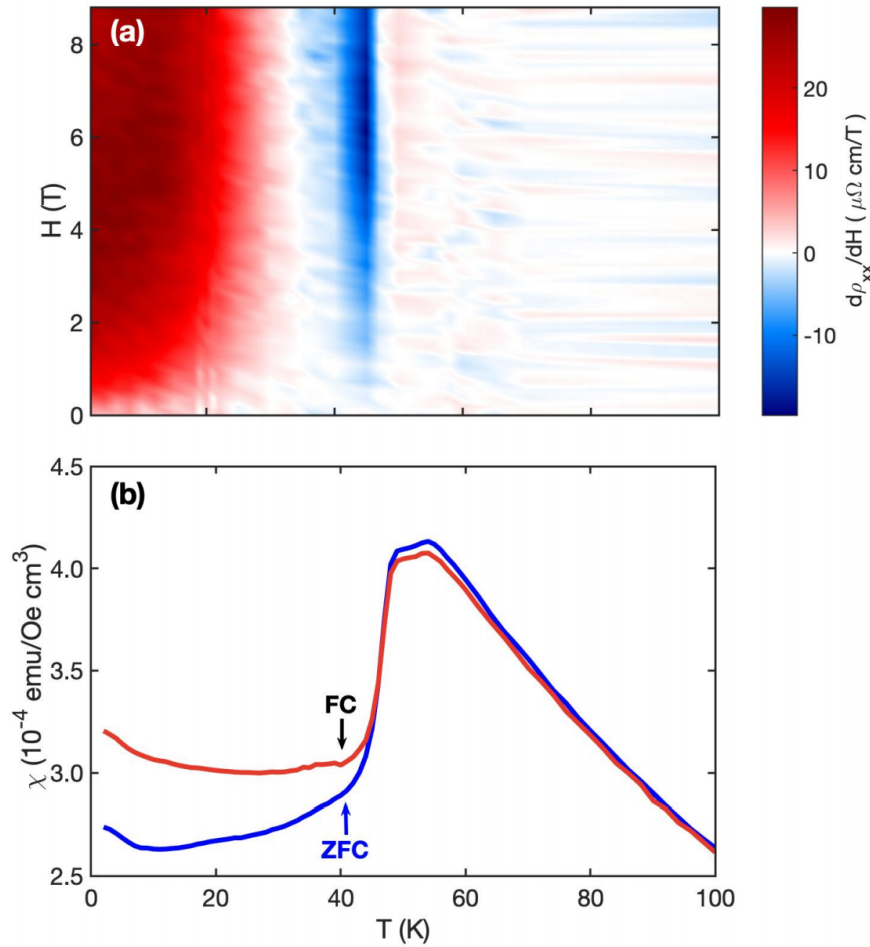


Fig. 4.4 (a) Magnetic field derivative of resistivity, $\frac{d\rho_{xx}}{dH}$ plotted as a function of field and temperature. Red(Blue) color indicates positive(negative)magnetoresistance. (b) Susceptibility measurement in an applied field of 5 K Oe in field cooled and zero field cooled condition. The bifurcation below 48 K could point towards the existence of ferromagnetic correlations in the system.

small and positive values for $T > T_s$, whereas in the $30 \text{ K} < T < T_s$ range it turns negative before turning to large positive values in the $T \rightarrow 0$ limit. There seems to exist a clear correlation between the onset of the negative magnetoresistance and the history dependent magnetic susceptibility measurements as shown in Fig 4.4 (b).

Low temperature Hall and Magnetisation isotherms show different responses to the applied field. Fig 4.5(a) shows the magnetisation in the field that shows a linear trend whereas the Hall resistivity displays a non linear field dependence at higher fields, indicating that these quantities are not directly coupled. Linear behaviour of the magnetisation in the temperature range of interest rule out the

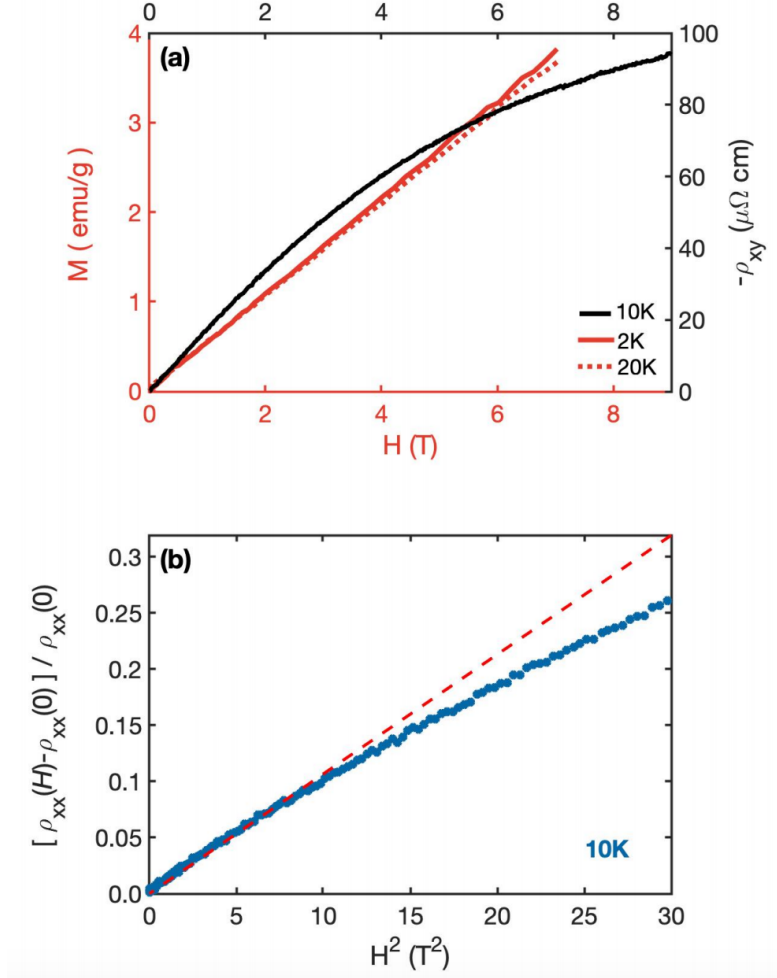


Fig. 4.5 Low temperature magnetisation, resistivity and Hall isotherms. (a) Hall and magnetisation isotherms plotted as a function of magnetic field H for temperatures as indicated. (b) MR isotherm at 10 K as a function of H^2 . The dashed red line represents the two-carrier model including higher order terms in H^2

possibility of anomalous contributions to the total Hall response [13]. Also, though the resistivity ρ_{xx} exhibits linear behavior w.r.t H^2 in the low field regime, significant deviations from this trend can be seen at higher fields as shown in Fig 4.5 (b).

4.4 Analysis and Modelling

The low – temperature, low – field behavior of the bilayer ruthenate, as discussed above, is characteristic of a metal with two Fermi surface sheets of different curvature and two dominant charge carriers [145]. To construct a framework for discussing and analysing the results obtained from magnetotransport measure-

ments we employ a simple two carrier Drude model with the assumption of field independent electron and hole carrier densities and mobilities.

$$\rho_{xx}(H) = \frac{(\sigma_h + \sigma_e) + \sigma_h\sigma_e(\sigma_h R_h^2 + \sigma_e |R_e|^2)H^2}{(\sigma_h + \sigma_e)^2 + \sigma_h^2\sigma_e^2(R_h - |R_e|)^2 H^2}, \quad (4.1)$$

$$\rho_{xy}(H) = \frac{\sigma_h^2 R_h - \sigma_e^2 |R_e| - \sigma_h^2\sigma_e^2 R_h |R_e| (R_h - |R_e|)H^2}{(\sigma_h + \sigma_e)^2 + \sigma_h^2\sigma_e^2(R_h - |R_e|)^2 H^2} H. \quad (4.2)$$

The model has four parameters $\sigma_{e/(h)}$ and $R_{e/(h)}$ that denotes the electron(or hole) conductivities and Hall coefficients respectively, given by

$$\begin{aligned} \sigma_i &= n_i e \mu_i \\ R_i &= \frac{1}{n e} \end{aligned} \quad (4.3)$$

where μ_i is the mobility of the electron(hole) carriers and e is the electronic charge. Here one emphasize that the validity of the formulation relies on the assumptions of no change in carrier properties and no field induced Fermi surface changes in the region of interest. Analysing two equations with four unknown parameters is constraining and here we make a few simplifying assumptions. In zero field,

$$\rho_{xx}(H = 0) = \frac{1}{(\sigma_h + \sigma_e)} \equiv \frac{1}{\sigma}, \quad (4.4)$$

For simplicity, we assume the electron carrier density from previous ARPES and Quantum Oscillation measurements [14, 66]. The problem now reduces to 2 unknown parameters. To simplify further we express $\rho_{xx}(H)$ and $\rho_{xy}(H)$ to the lowest order in magnitude in H .

$$\lim_{H \rightarrow 0} \rho_{xx}(H) = \frac{1}{\sigma} + \frac{\sigma_h\sigma_e[\sigma_h R_h + \sigma_e |R_e|]^2 H^2}{\sigma^3} \equiv \sigma^{-1} + C H^2 \quad (4.5)$$

where

$$C = \frac{\sigma_h\sigma_e[\sigma_h R_h + \sigma_e |R_e|]^2}{\sigma^3} \quad (4.6)$$

The quantity C can be easily determined from the slope of the magnetoresistance versus H^2 plot as shown in figure 4.3(b) for a representative low temperature data set.

$$\lim_{H \rightarrow 0} \frac{\rho_{xy}(H)}{H} \equiv R_H = \frac{[\sigma_h^2 R_h - \sigma_e^2 |R_e|]}{\sigma^2} \quad (4.7)$$

Now we have reduced the problem to two equations with two unknowns - σ_h and R_h .

Equation 4.6 is then refashioned and R_h is written in terms of C , σ and σ_h given by

$$R_h = \sqrt{\frac{C\sigma^3}{\sigma_h^3(\sigma - \sigma_h)}} - \frac{(\sigma - \sigma_h)R_e}{\sigma_h} \quad (4.8)$$

where $\sigma - \sigma_h \equiv \sigma_e$.

Similarly from Equation 4.6 R_h is now expressed in terms of other known parameters namely R_H , σ and R_e given by,

$$R_h = \frac{[R_H\sigma^2 + (\sigma - \sigma_h)^2|R_e|]}{\sigma_h^2} \quad (4.9)$$

Equating Equations 4.8 and 4.9 we have an expression with σ_h as the only unknown parameter,

$$\frac{[R_H\sigma^2 + |R_e|(\sigma - \sigma_h)^2]}{\sigma_h^2} + \frac{(\sigma - \sigma_h)|R_e|}{\sigma_h} - \sqrt{\frac{C\sigma^3}{(\sigma - \sigma_h)\sigma_h^3}} = 0 \quad (4.10)$$

Solving equation 4.10 in Mathematica yields analytical expression for σ_h in terms of known parameters C , σ , R_H , and R_e . Considering the real solution we have σ_h given by

$$\sigma_h = \frac{1}{6|R_e|^2} \left[[2\sigma|R_e|(3|R_e| + 2R_H)] + \frac{[2 \times 2^{1/3}\sigma|R_e|^2(\sigma R_H^2 - 3C)]}{(D1 + D2)^{1/3}} + 2^{2/3}[(D1 + D2)^{1/3}] \right]$$

$$D1 = -\sigma^2|R_e|^3(2\sigma R_H^3 + 9C(3|R_e| + 2R_H))$$

$$D2 = 3\sqrt{3}\sqrt{C\sigma^3|R_e|^6[4\sigma^2 R_H^3(|R_e| + R_H) + C\sigma(27|R_e|^2 + 36|R_e|R_H + 8R_H^2) + 4C^2]} \quad (4.11)$$

Although the equation 4.11 looks quite complicated it can be easily reduced to a compact form in terms of two dimensionless parameters α and β given by

$$\begin{aligned} \frac{\sigma_h}{\sigma} &= A_1 + \frac{A_2}{[A_3 + A_4]^{1/3}} + \frac{1}{3 \times 2^{1/3}}[A_3 + A_4]^{1/3} \\ &= \mathcal{F}(\alpha, \beta) \end{aligned} \quad (4.12)$$

with A_i 's defined as follows

$$\begin{aligned}
 A_1 &= 1 + \frac{2}{3}\alpha, \\
 A_2 &= \frac{\sqrt[3]{2}}{3}(\alpha^2 - \beta), \\
 A_3 &= -[2\alpha^3 + 3\beta(2\alpha + 3)], \\
 A_4 &= \sqrt{3}\beta\sqrt{\frac{4\beta}{3} + \frac{12\alpha^3(1 + \alpha)}{\beta} + (27 + 36\alpha + 8\alpha^2)}
 \end{aligned} \tag{4.13}$$

where the dimensionless parameters are defined as $\alpha \equiv \frac{R_H}{|R_e|}$ and $\beta \equiv \frac{3C}{\sigma R_e^2}$

With $\frac{\sigma_h}{\sigma} = \mathcal{F}(\alpha, \beta)$, and using the relation $\alpha = \frac{R_H}{|R_e|}$ and equation 4.7 one can find a similar expression for the ratios of the Hall coefficients of electron and hole carriers given by

$$\begin{aligned}
 \frac{R_h}{R_e} &= \frac{\alpha + [1 - \mathcal{F}(\alpha, \beta)]^2}{[\mathcal{F}(\alpha, \beta)]^2} \\
 &= \mathcal{G}(\alpha, \beta) \\
 &= \frac{n_e}{n_h}
 \end{aligned} \tag{4.14}$$

where $n_{e/h}$ are the electron/ hole carrier density.

Similarly, the mobility ratios can be expressed as

$$\frac{\mu_h}{\mu_e} = \mathcal{G}(\alpha, \beta) \left[\frac{\mathcal{F}(\alpha, \beta)}{1 - \mathcal{F}(\alpha, \beta)} \right] \tag{4.15}$$

Hence using these formulations we have described the ratio of carrier densities, conductivities and mobilities within the phase space of the two dimensionless parameters α and β . The solutions to the two-band model for conductivity ratios carrier density ratios and mobility ratios can be seen in Figs 4.6 (a), (b) and (c).

The parameter $\alpha = \frac{R_H}{|R_e|}$ is more intuitive and relevant in our discussion as it defines the domain of the region of interest. Within the framework of the electron-hole two-band model, α varies from $-1 \leq \alpha < \infty$ (with the range defined by whether the conductivity is dominated by electrons or holes). $\alpha \approx -1$ defines the electron dominated regime in conductivity, where as $|\alpha| \approx 0$ describes the compensated regime with comparable contributions from electron and hole carriers to the conductivity. Next we discuss the properties of our solutions.

To have a better grasp of the function $\mathcal{F}(\alpha, \beta)$ given by Equation 4.12 we find the

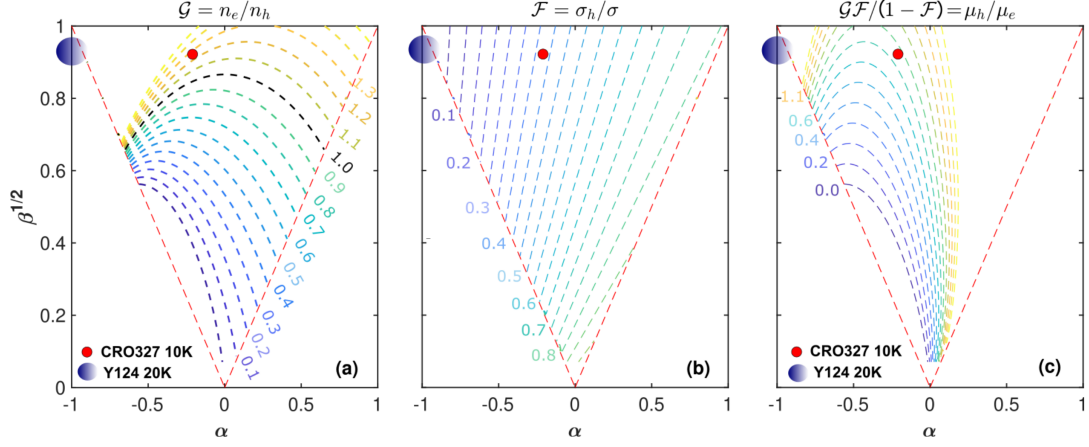


Fig. 4.6 Solution to the two-band model. (a) and (b) (c) Carrier density ratio n_e/n_h conductivity ratio σ_h/σ , and mobility ratio μ_h/μ_e versus the dimensionless parameters α and $\sqrt{\beta}$. Dashed lines are contours of the respective quantities. Solution are found for $\beta > \alpha^2$. The $n_e/n_h = 1$ contour line, given by $\beta = 3(1-\alpha^2)/4$ indicate the border between hole and electron "doped" regimes. The parameter space around $\beta = \alpha = 1$ represents the $n_e \gg n_h$ regime whereas $n_e \ll n_h$ is found for $\beta, \alpha \rightarrow 0$. A system obeying the Luttingers sum rule, will be staying on a fixed $n_e/n_h = 1$ contour line.

range where the solutions are real and feasible in the domain $-1 \leq \alpha < \infty$ and $\beta \geq 0$ (as the MR is positive within the scope of the model) given by the condition

$$A_3 + A_4 > 0 \quad (4.16)$$

Solving this we have solutions to the two-band model possible only when

$$\begin{aligned} \beta &> \alpha^2 \\ \implies \frac{C}{\sigma R_H^2} &> 1/3 \end{aligned} \quad (4.17)$$

Since we have the condition described by all measurable quantities – C , σ and R_H – independent of our initial assumption of R_e , this provides a quick and direct applicability test for a system's compliance with a two-band model.

As long as the carrier density ratios remain constant ($n_e + n_h = n_e(1 + \mathcal{G}^{-1}) = \text{Constant}$), the system stays on constant curved (α, β) trajectories (See fig 4.6 (a)). Deviations from the trajectories implies a change in filling, possible reconstruction of the Fermi surface, possible emergence of multiband structures or that the two-band model is too simplistic an approach to explain the obtained results.

In the most simple case when a system is assumed to lie on the $n_e/n_e = 1$ contour

line (or equivalently $R_h = R_e$), the equations 4.6 and 4.7 can be rewritten as follows

$$\begin{aligned} R_H &= \frac{R_e(\sigma_h - \sigma_e)}{\sigma} \\ C &= \frac{R_e^2 \sigma_h \sigma_e}{\sigma} \end{aligned} \quad (4.18)$$

Using these in $\alpha = \frac{R_H}{R_e}$ and $\beta = \frac{3C}{\sigma R_e^2}$, we have for the $\frac{n_e}{n_h} = 1$ contour line $\beta = \frac{3(1 - \alpha^2)}{4}$ which provides us with another solution property. If a system is known to be hole doped, i.e $n_h > n_e$ we have the boundaries defined as follows

$$\begin{aligned} \beta &< \frac{3(1 - \alpha^2)}{4} \\ |\alpha| &< \sqrt{\frac{3}{7}} \end{aligned} \quad (4.19)$$

4.5 Discussion

With the formulation, boundary conditions, solution properties and criterias established in the previous section, we can now check for the applicability of our analysis scheme, for the sample we have measured and samples taken from other studies/references, to look for agreement with a two-band model .

Recent ARPES data suggest that $\text{Ca}_3\text{Ru}_2\text{O}_7$ is a semimetal at low temperatures with one electron pocket and two identical hole pockets.

Fig 4.7 (b) shows a pictorial depiction of the Fermi surface of $\text{Ca}_3\text{Ru}_2\text{O}_7$ at $T < 30$ K [14]. The electron pocket, corresponds to a carrier density of $n_e = 7.8 \times 10^{24} \text{m}^{-3}$ and is consistent with dominant quantum oscillation frequency in the study by Kikugawa *et al.* [66]. From this the electron Hall coefficient can be calculated with $R_e = -1/en_e$. Using our low field magnetoresistance data at a representative temperature of 10 K, and substituting these values in equations 4.12 and 4.14 we have $\alpha = -0.21$, $\beta = 0.8$, $\frac{\sigma_h}{\sigma} = 0.36$, $\frac{R_h}{R_e} = 1.26$, $\frac{\mu_e}{\mu_h} = 1.6$.

The estimates for α and β position our system in the "sweet spot" within the dimensionless phase space (postion of $\text{Ca}_3\text{Ru}_2\text{O}_7$ within the phase space is indicated by red sphere in Fig 4.6). Our conclusion – the majority carriers being electrons – is consistent with the low temperature ARPES derived Fermi surface. Also, the implication of our results that the electrons are more mobile than the holes is consistent with the quantum oscillation study where the largest oscillation amplitude is found for the frequency corresponding to the electron pocket in the ARPES

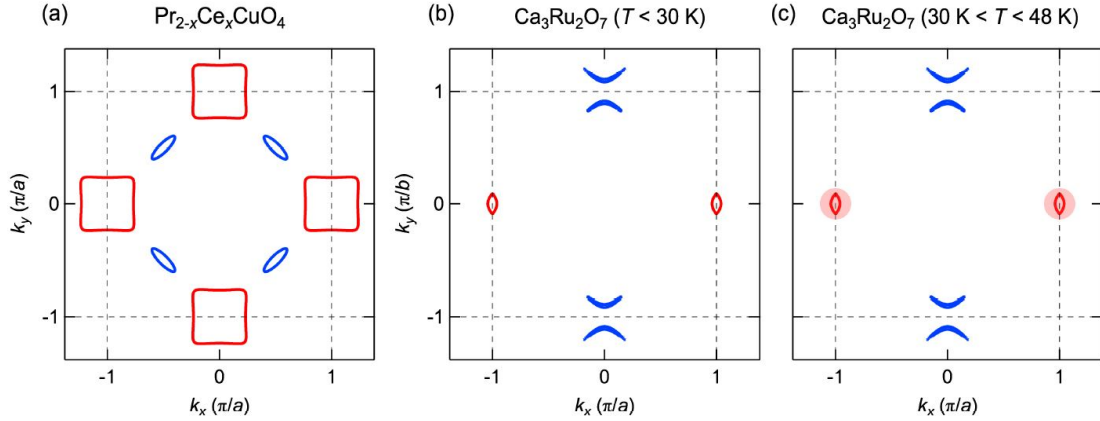


Fig. 4.7 Schematic representation of Fermi surfaces of two carrier systems. The blue and red structures represent hole like and electron like pockets respectively. (a) The Fermi surface in PCCO after folding/reconstruction around the anti-ferromagnetic zone boundary. (b) and (c) Evolution of Fermi surface with temperature in $\text{Ca}_3\text{Ru}_2\text{O}_7$. ARPES studies point towards a complex structure of the electron like pocket. Adapted from reference [14]

measurement.

The analytic formulation presented here combined with magnetotransport measurements can be applied to several other systems. In the next section we discuss its application to cuprate superconductors $\text{Pr}_{1.86}\text{Cr}_{0.14}\text{CuO}_{4\pm\delta}$ (PCCO) and $\text{YBa}_2\text{Cu}_4\text{O}_8$.

Let us consider the underdoped systems of $\text{YBa}_2\text{Cu}_3\text{O}_y$ with $y = 6.51$, $y = 6.67$ and $\text{YBa}_2\text{Cu}_4\text{O}_8$ [146, 147]. Since the system is hole doped, we have, $n_h > n_e$. Calculating the parameter α from the Hall measurements, we have $\alpha \approx -1$, this is a direct contradiction to our previously established condition for hole doped systems given by equation 4.19. Similarly, calculation of β positions the system in the $n_e \gg n_h$ region where $\sigma_h \rightarrow 0$ (see Fig 4.6). An explanation for this apparent contradiction and the breakdown of the model has been attributed to a FS reconstruction in the system due to a charge density wave order, resulting in a complex multi band structure outside the bounds of our two-band model. The Hall effect measurements have shown that the system has negative Hall coefficient, R_H , in the normal state at low temperature and is estimated from quantum oscillation measurements to be around $-29\text{mm}^3/\text{C}$. Our easy and direct test point towards the possibility of the system having electron pockets in the Fermi surface. Eventhough the material is hole doped the mobilities of the electron like parts are strong enough to outweigh the contribution from the hole like parts resulting in a negative Hall coefficient. As band structure calculations within the Local Density Approximation (LDA) do not support the presence of electron like pockets, it was

pointed out that there could be a reconstruction of the Fermi surface due to the onset of a charge wave density phase.

In the electron doped compound of $\text{Pr}_{1.86}\text{Cr}_{0.14}\text{CuO}_{4\pm\delta}$ [148], quantum oscillation measurements revealed the presence of small hole like pocket in the Fermi surface (See Fig 4.7 (a)). Since the system is electron doped, $n_e > n_h$ is to be expected. From Hall effect measurements however R_H is positive at low temperatures and exhibits sign change that point towards multiband behavior. ARPES experiments have shown the possibility of a reconstructed Fermi surface with two hole like and one electron like pocket around the reduced AFM Brillouin zone. The size of the hole pocket estimated from the dominant frequency in the quantum oscillation experiments has been approximated to be about 1% of the Brillouin zone. The Hall effect measurements however estimates it to be around 33%. The contribution from the much larger electron pockets are absent in the oscillation frequency. Since here we have $R_h \gg R_e$, $\alpha \ll 1$ and evaluation of the MR yields $\beta \approx 0.03$ less than $\frac{3(1 - \alpha^2)}{4}$. The system is thus compatible with a two – band model.

From the above discussions we have shown that the model and the analysis scheme presented here sensibly describe the magnetotransport measurements. However it has certain drawbacks. Even in the low temperature regime, $2 \text{ K} < T < 30 \text{ K}$, the dimensionless parameters α and β varies with temperature inconsistent with a constant n_e/n_h contour (See Fig. 4.8).

The observation of negative magnetoresistance is another feature that the model cannot account for (Fig 4.4). Also the formulation cannot explain the pronounced deviation of the ρ_{xx} , ρ_{xy} data from the model at higher field regime (shown in Fig 4.5). The apparent failure of the model can be attributed to the following reasons. For a semimetal with electron like and hole like Fermi surface, the magnetoresistance scales as $\frac{\delta\rho}{\rho_0} = \langle\mu_m^2\rangle B^2$ where $\mu_m = \sqrt{\mu_e\mu_h}$ [144]. In semimetals like graphite and bismuth large magnetoresistance is seen which scales as $\mu_e\mu_h B^2$ and is attributed to the balanced hole- electron condition i.e $n_e = n_h$ [149–151]. As long as the resonance is maintained the MR and Hall isotherms increases linearly without saturation. However in semimetals even a slight deviation from perfect compensation i.e $\mathcal{G} \neq 1$ will cause the MR to eventually saturate in the high field regime [151] As shown in Figs 4.5 (a) and (b) we observe saturation trend for the MR and Hall resistivity isotherm as higher field strength. Since we have $\mathcal{G} \approx 1$ in our system, the saturation effect we see cannot be explained within the scope of the two–band model. In general the deviation from linear behaviour could correspond to non- trivial contributions- anomalous or topological to the Hall resistivity. The anomalous contribution could be the result of intrinsic or

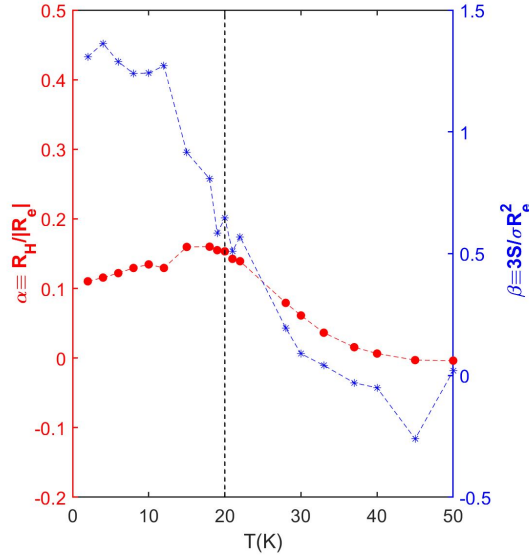


Fig. 4.8 The variation of the dimensionless parameters α (shown in red) and β (shown in blue) with respect to temperature inconsistent with a constant n_e/n_h contour pointing towards the possibility of a T dependent carrier density even below the FS reconstruction temperatures.

extrinsic scattering mechanisms [13]. In our magnetisation data shown in the same panel it can be seen that it scales perfectly with field. Hence ferromagnetism as a possible source of the saturating Hall resistivity can be excluded. So we can conclude that the underlying assumption that the mobility is field independent is not true in the $B > 4T$ regime. Another possible cause for the inconsistency of the model could be that the carrier density ratios are in fact temperature dependent. Recent density-functional-theory (DFT) calculations [143] suggest a strong coupling between detailed lattice structure and a temperature dependent Coulomb interaction. Early neutron diffraction experiments demonstrated temperature dependence of ruthenium-oxygen bond angles [67]. It is therefore not inconceivable that the chemical potential and even the low-energy electronic structure is temperature dependent. Recent ARPES studies [13, 14] has shown that the Fermi surface undergoes a two stage reconstruction with characteristic temperature scales at $T^* = 30$ K and $T_s = 48$ K. Since the negative magnetoresistance is found in the same temperature range it is very likely linked to the intermediately reconstructed complex Fermi surface and cannot be described within the confines of our model. The temperature dependence of the susceptibility (see Fig 4.4(b)) shows a cusp at T_s below which the magnetisation is history dependent and the zero field cooled and the field cooled curves bifurcate. This could correspond to a spin glass like transition in the system [98]. In a disordered magnetic system there could exist regions of magnetically ordered state even when the bulk is still magnetically

disordered [152, 153]. For our present case, it can be described as a coexistence of both antiferromagnetic and ferromagnetic fluctuations in the system. Recent small angle neutron studies have shown metamagnetism and the existence of a mixed state—where antiferromagnetism and ferromagnetism coexists at a jump like transition in the magnetic phase diagram in the bilayer $\text{Ca}_3\text{Ru}_2\text{O}_7$ [13]. In the presence of ferromagnetic contributions, a negative magnetoresistance due to electron- spin scattering can thus be observed as the applied field increases the effective field on the localised spins thereby suppressing their fluctuations resulting in an overall reduction in resistivity [154]. The ferromagnetic correlations in the system can hence describe the negative magnetoresistance in the $30\text{K} < T < 48\text{K}$ range of temperature. The negative magnetoresistance is therefore likely linked both to the electronic structure and the ferromagnetic properties that emerge in $\text{Ca}_3\text{Ru}_2\text{O}_7$.

4.6 Conclusions

Magnetoresistance measurements were carried out in the bilayer ruthenate - $\text{Ca}_3\text{Ru}_2\text{O}_7$. Three characteristic temperature scales were identified which are intimately linked to the accompanying Fermi surface reconstruction in the system. For $T < 30\text{K}$, the system shows positive magnetoresistance, in the temperature range $30\text{K} < T < 48\text{K}$ there is a cross over from positive to negative slope in the MR and for $T > 50\text{K}$ weak positive MR can be seen. We formulated a generalised scheme for analysing the low temperature, low field magnetotransport data within the framework of a two-band model. Though the model captures nicely the experimental results in the low field and low temperature regime, it is rendered unusable in the higher field and temperature regions. The limitation of the model includes its inability to explain the negative slope in magnetoresistance in the $30\text{K} < T < 48\text{K}$. Also, due to the temperature modulated two stage Fermi surface reconstruction in the system, volume of the region enclosed by the Fermi surface and with that the carrier density ratio is temperature dependent which violates the assumption on which the model is developed. This in combination with the ferromagnetic fluctuations generates the complicated behavior of magnetoresistance in $\text{Ca}_3\text{Ru}_2\text{O}_7$.

Chapter 5

Conclusions

In summary, O-*K* edge RIXS study of the single layered ruthenate system – Ca_2RuO_4 and electrical and thermoelectric measurements on the bilayer ruthenate – $\text{Ca}_3\text{Ru}_2\text{O}_7$ have been carried out. In the Ca214 system, using XAS and RIXS studies new insights were obtained supported by theoretical modelling. There it was shown that the Mott insulating transition driven by the change in structure from long to short *c* - axis, drives the lower energy d_{xy} orbital to band insulating or fully filled state while the $d_{xz/yz}$ bands go Mott insulating. Four excitations dubbed A,B,C and D were identified at energies 80 meV, 400 meV, 1.3 eV and 2.2 eV respectively that showed strong dependence on incident light polarisation. The dispersive low energy excitation at 400 meV is interpreted as a strong spin orbit coupling driven transition within the spin-triplet sector. This was also reproduced in a later work by Gretarsson *et al.* [61] where this transition was interpreted as a spin orbit driven $\mathbf{J} = \mathbf{0} \rightarrow \mathbf{J} = \mathbf{2}$ excitation at 0.4 eV. The excitation at 80 meV is of magnetic origin consistent with two magnon modes and Higgs mode reported in the recent Raman and neutron scattering studies [36, 37]. The higher energy excitations are Hund’s rule driven excitations corresponding to transitions from spin-triplet to spin-singlet states at Ru sites. With higher energy resolution, the study can be extended to obtain information about the orbital character of these excitations. The development of new Ru-*L* β edge RIXS spectrometer could provide impetus for further studies on the single layered ruthenate system and other 4*d* compounds unveiling the low energy spin excitation sectors.

In the bilayer ruthenate– $\text{Ca}_3\text{Ru}_2\text{O}_7$, magnetoresistance measurements were carried out. The system consist of two electron like and hole like bands and ARPES studies and thermopower measurements have shown that with decrease in temperature below $T^* = 30\text{K}$ the chemical potential decreases and one of the electron like bands in FS is gapped out while the hole like band and the other electron like band survive, making it an effective two–band system at low temper-

atures. [14, 72]. With this as a starting point we have formulated in this thesis, an analytical scheme for magnetotransport study for two-band system, where the electron and hole carrier densities and conductivities are mapped into a dimensionless phase space defined by two parameters α and β obtained from magnetoresistance and Hall measurements. This scheme is then applied to $\text{Ca}_3\text{Ru}_2\text{O}_7$ and the usability of the model is further extended to other systems like the cuprate superconductors to check their compliance or lack thereof with a two-band model.

The last section of the thesis (in the appendix) describes the thermoelectric measurements on Weyl semimetals – EuCd_2As_2 and PrAlGe , carried out using a home built probe. The results showed the presence of anomalous contributions to Hall and Nernst effect in these systems stemming from Berry curvature associated with Weyl nodes. The experiments are still under way. With the field of topology making great strides over the past few years in various applications like spintronics, these materials are thus paradigm systems for providing useful insights into the interplay between magnetism and topology.

Appendix A

Thermoelectric Studies in Miscellaneous Systems

This section discusses briefly the thermoelectric measurements in various systems carried out using the custom made home built thermoelectric insert for PPMS developed during the PhD period. Results of some of these measurements have been published, and some are under preparation.

A.1 PrAlGe

Weyl semimetals (WSM) are topological conductors that host Weyl Fermions—the low energy excitations of the WSM—and possess Weyl nodes which are the crossing points of nondegenerate linearly dispersing bands in momentum space [155]. PrAlGe belongs to the half heusler compounds in the RAlGe (R is a rare earth) family and has been recently predicted to be magnetic Weyl semimetal that breaks both time-reversal and inversion symmetry [99]. See Fig A.1

The study by chang *et al.* [99] predicted that PrAlGe is a magnetic type I Weyl semimetal that breaks both time reversal and inversion symmetry. The breaking of the spatial inversion symmetry in this material facilitate the generation of Weyl nodes and the ferromagnetism breaks the time reversal symmetry (TRS) and shifts the momentum space location of the Weyl nodes. The TRS breaking in magnetic materials results in the berry curvature that acts likes a magnetic field in k-space and imparts an anomalous velocity to the charge carriers generating an intrinsic anomalous Hall response characterised by generation of a transverse Hall voltage even in the absence of magnetic field [98, 156]. Berry curvature can also generate the thermal analogue of the anomalous Hall called the anomalous nernst effect which creates an electric voltage perpendicular to both the magnetization and an applied temperature gradient [157]. Destraz *et al.* performed measurements with a

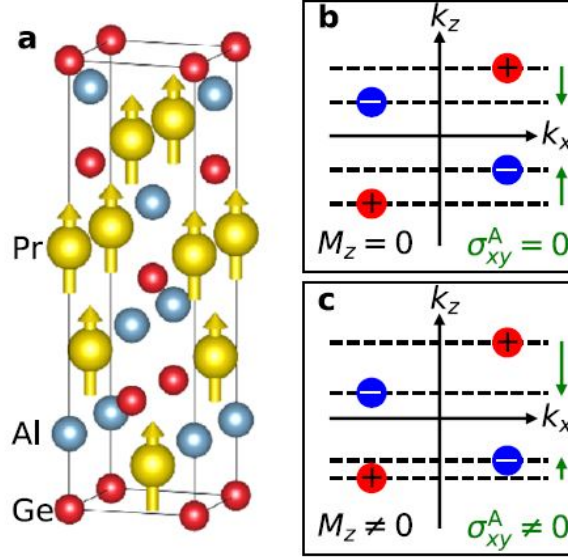


Fig. A.1 (a) Crystal structure of PrAlGe with space-group $I4_1md$ (No.109) composed of stacks of Pr, Al, and Ge layers, with each layer having only one type of element along the (001)direction. The arrows indicate the Pr- magnetic moments aligned along c-axis. (b)-(c)Pictorial illustration of effect of magnetisation on the location of Weyl nodes in k-space. Magnetisation shifts the Weyl nodes resulting in observable anomalous transport signals in the system. Taken from Reference [98]

range of experimental techniques on this material and unveiled the correspondence between the easy c -axis Pr ferromagnetism and the anomalous Hall and nernst effects [98]. Neutron scattering studies showed that PrAlGe orders as an easy c -axis ferromagnet below the critical temperature $T_c = 16K$. Although no spontaneous Hall or nernst response could be discerned at zero field, these effects emerged sharply with small magnetic fields that polarised the Pr- moments along crystallographic c -direction. The Hall and nernst isotherms are shown in Fig A.2 and shows a non linear dependence on magnetic field below T_c . The origin of the observed Hall and anomalous Nernst in this system has been attributed to Weyl node induced Berry curvature. The size of the anomalous Hall and anomalous nernst from the transport measurements were estimated to be $-\sigma_{xy}^A = 367 \text{ ohm}^{-1}\text{cm}^{-1}$ at 2K and $N^A = 28 \text{ nV/K}$ at 11 K respectively and are in good agreement with the values obtained from first principle calculations on electronic structure in the presence of uniform c -axis magnetisation thereby allowing us to allocate their origin to the berry curvature.

This work done by Destraz *et al.* has been published in npj quantum materials. Destraz, Daniel, *et al.* "Magnetism and anomalous transport in the Weyl semimetal

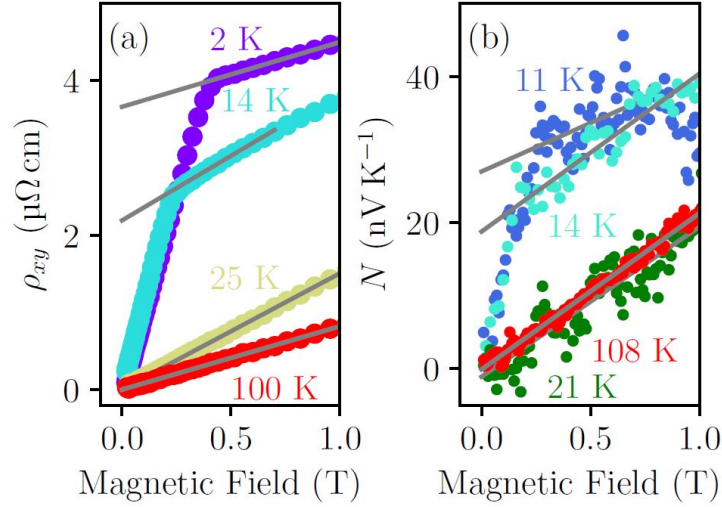


Fig. A.2 (a) The Hall resistivity isotherms.(b) Nernst isotherms resembling the behaviour of the Hall data. Both signals exhibit a kink at magnetic saturation below critical temperature that gets more pronounced as temperature is lowered. Taken from Reference [98]

PrAlGe: possible route to axial gauge fields." npj Quantum Materials 5.1 (2020): 1-8.

A.2 EuCd_2As_2

The discovery of Weyl semimetal phase in the non centrosymmetric compound of TaAs by Yang *et al.* [158] resulted in a wave of experimental investigations on various other candidate materials like GdPtBi [159], Mn_3Sn [160], $\text{Co}_3\text{Sn}_2\text{S}_2$ [161] etc... predicted to host the exotic and alluring low energy quasi particles - the Weyl Fermions. The extraordinary quantum transport properties exhibited by these systems arise from the topologically protected band crossings in these materials- dubbed Weyl nodes that come in pairs and have definite chirality(left or right handedness) [162]. The requirement for topological properties associated with Weyl semimetals to occur in crystals, is either broken time reversal symmetry or broken spatial inversion symmetry or both [163]. Although there have been various studies on Weyl semimetals with broken inversion symmetry like the compounds in the TaAs structural family, magnetic WSM with broken TRS are rare [100]. In order to delve deeply into the fundamental physics of Weyl Fermions, it is important to identify magnetic WSM systems that have a single pair of Weyl nodes located close to or near the Fermi level in an energy range not obscured by

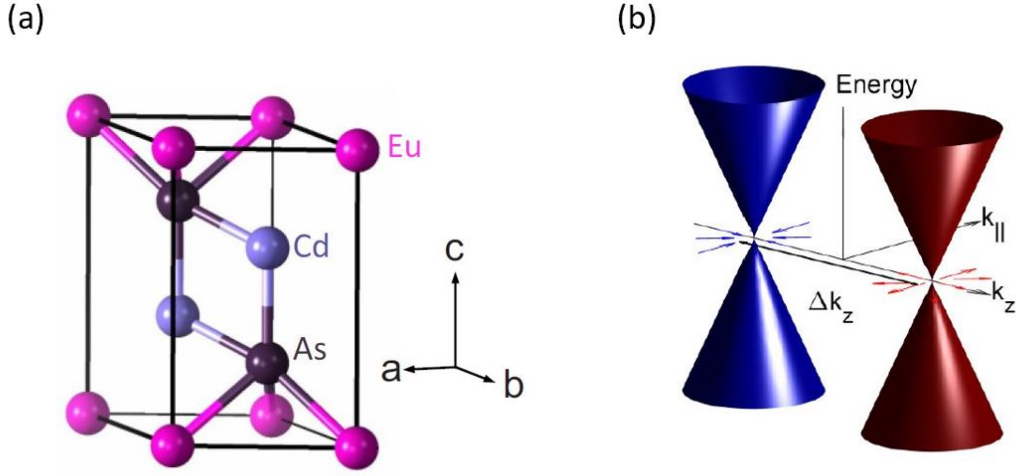


Fig. A.3 (a) Crystal structure of EuCd_2As_2 . (b) Schematic illustration of Weyl nodes. A small magnetic field applied parallel to c - axis fully align the Eu spins and in the fully spin polarised state a pair of Weyl nodes appear at the Fermi level. The singly degenerate conduction and valence bands cross at Weyl nodes which act as source and sink for berry curvature which is associated with the separation of the Weyl points in k - space. Taken from Reference [100]

other bands and such an ideal system would serve as a fertile ground to study Weyl physics [100, 164]. The studies by Soh *et al.* proposed that such an ideal WSM phase could be realised in the layered intermetallic EuCd_2As_2 (ECA) system [100]. Recent ARPES study by Ma *et al.* [165] showed that the Weyl physics emerge already in the paramagnetic phase of ECA with spin fluctuations breaking the time reversal symmetry. ECA has a trigonal layered structure and belongs to the space group $P\bar{3}m1$ (No.164) consisting of alternating layers of CdAs_2 and Eu layers [100, 165] and is an antiferromagnet with an ordering temperature $T_N \sim 9.5$ K (See Fig A.3).

A relatively small magnetic field of $B_c = 1.6$ T applied parallel to c - axis causes the Eu spins to be fully aligned along the c - axis and a single pair of Weyl nodes appear at the Fermi level [100]. In the wake of new TRS broken WSM which are predicted to be suitable candidates for carrying pure spin currents, [99] there is now a strong impetus to study anomalous transport properties arising from berry curvature in topological semimetals.

Here, a systematic study of the electrical and thermoelectrical properties of the ECA system has been carried out by Yang *et al.* [166] and this work is under preparation (See Fig A.4). This study showed that ECA system is a rare system

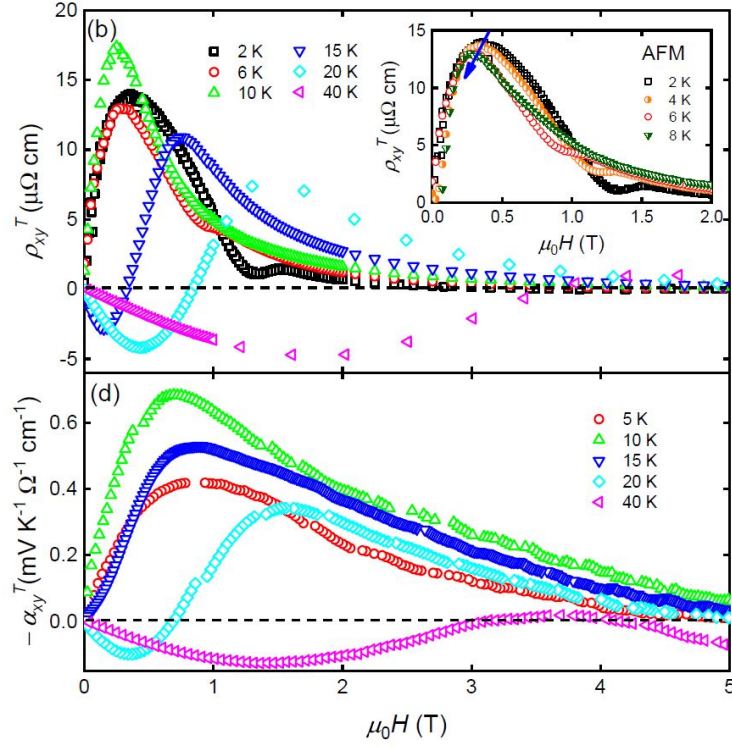


Fig. A.4 Magnetic field dependence of the topological Hall resistivity and the topological Nernst conductivity isotherms. Taken from Reference [166].

where signatures of topological transport have been observed both in the presence and absence of long range order.

Topological Nernst and Hall effect was observed above and below the AFM ordering temperature associated with Weyl points near the Fermi level. Topological transport effect in the presence of long-range magnetic order reported up to date has been attributed to either a real-space scenario or a momentum-space scenario. Whereas in the compound studied, a momentum-space scenario has been proposed previously, but with this study, we show that this is not sufficient, and real-space scenario like the presence of peculiar spin textures like skyrmions should also exist in the AFM phase. The work is currently in progress.

Acknowledgements

For everyone who has struggled and read the thesis upto this point I thank you for your patience and perseverance. And to those who immediately skipped to the acknowledgement section, well just know that the author is rolling her eyes and giving you looks of judgement.

My first and earnest acknowledgment goes to my PhD supervisor - Dr. Johan Chang for his advice, guidance and time and I am grateful to him for providing me the opportunity to work as a PhD student in his lab. I am also thankful to the members of my PhD committee - Dr. Titus Neupert, Dr. Jonathan White and Dr. David LeBoeuf for all the discussions and advice over the years. Special thanks to our theoretical collaborators at CNR Salerno - Dr. Mario Cuoco and Dr. Fiona Forte for all the helpful discussions.

An experimentalist without the samples is like a potter without clay - I express my sincere gratitude to all the crystal growers- Antonio Vecchione, Rosalba Fittipaldi, Veronica Granata and Pascal Puphal for their preparation of high quality samples within the time frame of our work.

A huge shout out to all the members of the electronic and mechanical workshop- especially Daniel Florin, Achim Vollhardt and Reto Maeier for all their help in every step of this Phd work. I also thank Dr. Xiaofu Zhang who always lend a helping hand to every student in the lab and for teaching me nuances of various measurement technique. The tremendous and excellent technical support from my groupmates – Dominik and Damian– requires special mention. I am very much thankful to my amazing groupmates from whom I learnt a lot- Dr. Yang Xu and Dr. Tian Shang for very fruitful discussions on topics ranging from condensed matter physics to chinese history and special thanks to Yang for teaching me Chinese chess and introduction to Chinese 101. I am also thankful to my groupmates - Dr. Masafumi Horio and Dr. Qisi wang for their patience and their help in various aspects of RIXS measurements and data analysis. Many thanks to Karin dearest friend of mine and her tea addiction and for the wonderful and crazy time together and the workshops and conferences which turned to fun vacations at the end. The lunch times in the mensa were made extra special by Kevin, one of the kindest person and a truest friend anyone can have, with his mini-lunchtime philosophical

discourse. Denys "Diablo" and "Sh"-Ivashko (they know what it means) were the first people I met when I first came to the University of Zurich. Since then they have been great friends and crazy fun to hang out with as it is always advisable to be with friends whose craziness surpasses yours that you end up being the normal person. Thank you for all the wonderful and crazy times and the chicken clucking sounds. I am really grateful to Ivashko who helped me a lot with RIXS measurement and analysis during the first year of my PhD. I thank Dr. Jaewon Choi for his patience in taking the time to listen to and explain any doubts in physics and for his cooking skills and a special thanks for introducing me to Korean cuisine. I thank Alsu for being a good friend and for the very many culinary adventures we shared. I thank Marianna for being one of the most caring person I have met and for the constant love, support and encouragement.

As a wise little birdie once said no matter where you are you should always remember where you came from- I thank Prof. Peter Lemmens and Dr. RajMohan - wonderful, kind, patient and great teachers and a constant source of inspiration to their students.

This acknowledgement is incomplete without Dani - the narrator of random thoughts, dweller of alternate universe, one of my closest ally, partner in crime, fellow appreciator of museums and castles, the one who taught me a wide range of important things ranging from filling Helium in the cryostat, doing measurements in the lab, Labview programming, to minigolf and "Magic:The gathering" card game - though his ardent morbid fascination to the card game is still a cause of concern.

My Family is my world - I thank my family - mum, pops, sis and my grandma for all the love and support throughout the years and my closest and 'bestest' friends in the whole wide world (getting old and sentimental, and hoping they dont read this part) - Swathi and Dipti - for years of unconditional love, oodles of fun, encouragement, and free therapy.

Lakshmi Das T.V

Curriculum Vitae

PERSONAL DETAILS

Address: Brandschenkestrasse 171, 8002 Zurich, Switzerland
Phone: (+41) 786587068
Mail: lakshmidastv90@gmail.com

PERSONAL SUMMARY

- 3+ years research work experience employing laboratory based experiments in Material Science with peer reviewed publications.
- People oriented team player, with good communication skills and work experience in a multicultural environment.
- Proactive and resilient hardworker and a problem solver capable of managing different aspects of projects simultaneously.

EDUCATION

PhD

2016-Present

University of Zurich

A comprehensive study of different properties, in a representative system of Ruthenates belonging to the strongly correlated family of materials, to uncover the fundamental principles that govern the various exotic properties in these systems using Spectroscopy measurements like Xray absorption Spectroscopy(XAS) and Resonant inelastic Xray Scattering techniques and Bulk measurements like Resistivity, Hall and Thermopower measurement techniques.

Master Of Technology (MTech)

2013-2015

Indian Institute of Technology(IIT-Delhi, India)

Masters studies with specialisation in Solid State Physics

Master Of Science (MSc)

2011-2013

Amrita University, Kerala, India

Masters in Physics

Bachelor of Science (BSc)

2008-2011

Amrita University, Kerala,India

Bachelors in Physics

PROJECT EXPERIENCE

MTech Project

2014-2015

University of Braunschweig, Full time

Raman Spectroscopic measurements in Topological Insulators. Supervised by:Dr Peter Lemmens Head of the Department,Department of Condensed Matter Physics,TU Braunschweig,Germany

Integrated MSc Project

2013

Indian Institute of Science(IISc), Bangalore, India; Full time

Low temperature noise measurements and magneto resistance measurements in 2D thin film superconductors.

Supervised by:Dr Aweek Bid Assistant Professor, Department of Physics, Indian Institute of Science, Bangalore ,India

HONOURS AND AWARDS

- Swiss Government Excellence Scholarship 2017-Present
- DAAD Sandwich model Scholarship for IIT students 2014-2015.
- Proficiency Award for Academic Excellence by Amrita School of Sciences in the years 2010,2011,2012,2013.
- First Rank holder in MSc

SKILLS

<i>Languages</i>	Malayalam(South Indian Language) (mother tongue) English (Highly Fluent) Hindi (Intermediate) Tamil (Intermediate) German (Beginner)
<i>Software</i>	MATLAB, L ^A T _E X, LABVIEW, Microsoft Office

TEACHING EXPERIENCE

- Bachelor thesis supervision (2019-2020).
- Responsible for student labs for physics major bachelor students from (2017-2019).

WORKSHOPS AND CONFERENCES

- Oral Presentation at the 10th international Conference in New Generation in Strongly Correlated Electrons Systems NGSCES (2019)
- Oral Presentation at the Joint Annual Meeting of the Swiss Physical Society-SPS(2019)
- Lab Hack Days Workshop- Introduction to CAD and 3D printing fundamentals and electronics fundamentals (2019)
- MaNEP WinterSchool SaasFee, Switzerland (2019).
- Poster Presentation at the Joint Annual Meeting of the Swiss Physical Society-SPS(2018)
- MaNEP WinterSchool SaasFee, Switzerland (2017).

INTERESTS AND ACTIVITIES

- Watercolor Painting
- Trained in Indian music
- Trained in Indian classical dance-Bharathanatyam
- Currently learning Piano
- Travelling
- Avid reader of both fiction and non fiction

PUBLICATIONS

1. Under preparation-"Two-carrier Magnetoresistance: Applications to $Ca_3Ru_2O_7$ ". **L. Das**, Y. Xu, T. Shang, M. Horio, S. Johr, J. Mueller, D. Biscette, V. Granata, R. Fittipaldi, A. Vecchione, and J. Chang
2. "Spin-Orbital Excitations in Ca_2RuO_4 Revealed by Resonant Inelastic X-Ray Scattering". **L. Das**, F. Forte, R. Fittipaldi, C. G. Fatuzzo, V. Granata, O. Ivashko, M. Horio, F. Schindler, M. Dantz, Yi Tseng, D. E. McNally, H. M. Ronnow, W. Wan, N. B. Christensen, J. Pelliciani, P. Olalde-Velasco, N. Kikugawa, T. Neupert, A. Vecchione, T. Schmitt, M. Cuoco, and J. Chang Physical Review X 8, 11048 (2018)
3. "Magnetism and anomalous transport in the Weyl semimetal PrAlGe: possible route to axial gauge fields". Daniel Destraz, **Lakshmi Das**, Stepan S. Tsirkin, Yang Xu, Titus Neupert, J. Chang, A. Schilling, Adolfo G. Grushin, Joachim Kohlbrecher, Lukas Keller, Pascal Puphal, Ekaterina Pomjakushina, Jonathan S. White npj Quantum Materials 5, 5 (2020)
4. Anisotropic magnetic excitations and incipient Neel order in $Ba(Fe_{1-x}Mn_x)_2As_2$ Fernando A. Garcia, Oleh Ivashko, Daniel E. McNally, **Lakshmi Das**, Mario M. Piva, C. Adriano, Pascoal G. Pagliuso, Johan Chang, Thorsten Schmitt, and Claude Monney Physical Review B 99, 115118 (2019)
5. Crossover from multiple- to single-gap superconductivity in $Nb_5Ir_{3-x}Pt_xO$ alloys Y. Xu, S. Joehr, **L. Das**, J. Kitagawa, M. Medarde, T. Shiroka, J. Chang, and T. Shang Physical Review B 101, 134513 (2020)
6. von Arx, K., Forte, F., Horio, M., Granata, V., Wang, Q., **Das, L.**, Tseng, Y. et.al (2020). "Comparative Resonant Inelastic X-ray Scattering Study of Ca_2RuO_4 and $Ca_3Ru_2O_7$ ". arXiv preprint arXiv:2004.13391.
7. Horio, M., Wang, Q., Granata, V., Kramer, K.P., Sassa, Y., Johr, S., Sutter, D., Bold, A., **Das, L.**, Xu, Y. and Frison, R., 2019. "Electron-driven C_2 -symmetric Dirac semimetal uncovered in $Ca_3Ru_2O_7$ ". arXiv preprint arXiv:1911.12163.
8. "Direct observation of orbital hybridisation in a cuprate superconductor". C. E. Matt, D. Sutter, A. M. Cook, Y. Sassa, M. Mansson, O. Tjernberg, **L. Das**, M. Horio, D. Destraz, C. G. Fatuzzo, K. Hauser, M. Shi, M. Kobayashi, V. N. Strocov, T. Schmitt, P. Dudin, M. Hoesch, S. Pyon, T. Takayama, H. Takagi, O. J. Lipscombe, S. M. Hayden, T. Kurosawa, N. Momono, M. Oda, T. Neupert, J. Chang Nature Communications 9, 972 (2018)

REFERENCES

Prof.Dr.Johan Chang (PhD Supervisor)
University of Zurich
Department of Physics
Winterthurerstrasse 190, 8057 Zurich
Switzerland
Tel: +41 44 635 5748
email: johan.chang@physik.uzh.ch

Bibliography

- [1] Nigel Goldenfeld and Leo P Kadanoff. Simple lessons from complexity. *science*, 284(5411):87–89, 1999.
- [2] Elbio Dagotto. Complexity in strongly correlated electronic systems. *Science*, 309(5732):257–262, 2005.
- [3] Philip W Anderson. More is different. *Science*, 177(4047):393–396, 1972.
- [4] Alan D McNaught, Andrew Wilkinson, et al. *Compendium of chemical terminology*, volume 1669. Blackwell Science Oxford, 1997.
- [5] G Cao, CS Alexander, S McCall, JE Crow, and RP Guertin. From antiferromagnetic insulator to ferromagnetic metal: a brief review of the layered ruthenates. *Materials Science and Engineering: B*, 63(1-2):76–82, 1999.
- [6] Feng Duan and Jin Guojun. *Introduction To Condensed Matter Physics: Volume 1*, volume 1. World Scientific Publishing Company, 2005.
- [7] Cao Gang et al. *Frontiers of 4D-and 5D-transition Metal Oxides*. World Scientific, 2013.
- [8] J George Bednorz and K Alex Müller. Possible high c superconductivity in the Ba-La-Cu-O system. *Zeitschrift für Physik B Condensed Matter*, 64(2):189–193, 1986.
- [9] Yoshiteru Maeno, T Maurice Rice, and Manfred Sgrist. The intriguing superconductivity of strontium ruthenate. *Physics Today*, 54(1):42–47, 2001.
- [10] Y Maeno, H Hashimoto, K Yoshida, S Nishizaki, T Fujita, JG Bednorz, and F Lichtenberg. Superconductivity in a layered perovskite without copper. *Nature*, 372(6506):532–534, 1994.
- [11] Denys Sutter. *Strong electron correlations in the ruthenates: a spectroscopic study of Ca_2RuO_4 and $\text{Ca}_{1.8}\text{Sr}_{0.2}\text{RuO}_4$* . PhD thesis, University of Zurich, 2019.
- [12] G Cao, S McCall, JE Crow, and RP Guertin. Observation of a metallic antiferromagnetic phase and metal to nonmetal transition in $\text{Ca}_3\text{Ru}_2\text{O}_7$. *Physical review letters*, 78(9):1751, 1997.
- [13] DA Sokolov, N Kikugawa, T Helm, H Borrmann, U Burkhardt, R Cubitt, JS White, E Ressouche, M Bleuel, K Kummer, et al. Metamagnetic texture in a polar antiferromagnet. *Nature Physics*, 15(7):671–677, 2019.
- [14] M Horio, Q Wang, V Granata, KP Kramer, Y Sassa, S Jöhr, D Sutter, A Bold, L Das, Y Xu, et al. Electron-driven c_2 -symmetric dirac semimetal uncovered in $\text{Ca}_3\text{Ru}_2\text{O}_7$. *arXiv preprint arXiv:1911.12163*, 2019.
- [15] G Cao, XN Lin, L Balicas, S Chikara, JE Crow, and P Schlottmann. Orbitaly driven behaviour: Mott transition, quantum oscillations and colossal magnetoresistance in bilayered $\text{Ca}_3\text{Ru}_2\text{O}_7$. *New Journal of Physics*, 6(1):159, 2004.

- [16] Haruka Taniguchi. Variation of the electronic states of Ca_2RuO_4 and Sr_2RuO_4 under uniaxial pressures. 2014.
- [17] Florian Gebhard. Metal–insulator transitions. In *The Mott Metal-Insulator Transition*, pages 1–48. Springer, 1997.
- [18] Jan H de Boer and Evert JW Verwey. Semi-conductors with partially and with completely filled 3d-lattice bands. *Proceedings of the Physical Society*, 49(4S):59, 1937.
- [19] NF Mott and R Peierls. Discussion of the paper by de boer and verwey. *Proceedings of the Physical Society*, 49(4S):72, 1937.
- [20] Richard T Scalettar. An introduction to the hubbard hamiltonian. *Quantum Materials: Experiments and Theory*, 6, 2016.
- [21] Masatoshi Imada, Atsushi Fujimori, and Yoshinori Tokura. Metal-insulator transitions. *Reviews of modern physics*, 70(4):1039, 1998.
- [22] Y Maeno, S Nakatsuji, and S Ikeda. Metal–insulator transitions in layered ruthenates. *Materials Science and Engineering: B*, 63(1-2):70–75, 1999.
- [23] Y Maeno. Electronic states of the superconductor Sr_2RuO_4 . *Physica C: Superconductivity*, 282:206–209, 1997.
- [24] AV Puchkov, MC Schabel, DN Basov, T Startseva, G Cao, T Timusk, and Z-X Shen. Layered ruthenium oxides: from band metal to mott insulator. *Physical review letters*, 81(13):2747, 1998.
- [25] Xiunu Lin. A systematic study on the thermodynamic and transport properties of layered ruthenates. 2006.
- [26] Y Tokura and N Nagaosa. Orbital physics in transition-metal oxides. *science*, 288(5465):462–468, 2000.
- [27] E Gorelov, M Karolak, TO Wehling, F Lechermann, AI Lichtenstein, and E Pavarini. Nature of the mott transition in Ca_2RuO_4 . *Physical review letters*, 104(22):226401, 2010.
- [28] Britta Bohnenbuck. Resonant x-ray scattering studies of ruthenium oxides and ruthenocuprates. 2009.
- [29] Christopher Johannes Dietl. Synthesis and electronic ordering phenomena of calcium ruthenate thin films. 2018.
- [30] John B Goodenough. Electronic and ionic transport properties and other physical aspects of perovskites. *Reports on Progress in Physics*, 67(11):1915, 2004.
- [31] T Mizokawa, LH Tjeng, GA Sawatzky, G Ghiringhelli, Oscar Tjernberg, NB Brookes, H Fukazawa, S Nakatsuji, and Y Maeno. Spin-orbit coupling in the mott insulator Ca_2RuO_4 . *Physical review letters*, 87(7):077202, 2001.
- [32] Daniel I. Khomskii. *Transition Metal Compounds*. Cambridge University Press, 2014.
- [33] T. Mizokawa, L. H. Tjeng, G. A. Sawatzky, G. Ghiringhelli, O. Tjernberg, N. B. Brookes, H. Fukazawa, S. Nakatsuji, and Y. Maeno. Spin-orbit coupling in the mott insulator Ca_2RuO_4 . *Phys. Rev. Lett.*, 87:077202, Jul 2001.
- [34] Christopher Johannes Dietl. *Synthesis and electronic ordering phenomena of calcium ruthenate thin films*, 2018.
- [35] Giniyat Khaliullin. Excitonic magnetism in van vleck–type d^4 mott insulators. *Phys. Rev. Lett.*, 111:197201, Nov 2013.

- [36] A Jain, M Krautloher, J Porras, GH Ryu, DP Chen, DL Abernathy, JT Park, A Ivanov, Jiří Chaloupka, G Khaliullin, et al. Higgs mode and its decay in a two-dimensional anti-ferromagnet. *Nature Physics*, 13(7):633–637, 2017.
- [37] Sofia-Michaela Souliou, Jiří Chaloupka, Giniyat Khaliullin, Gihun Ryu, Anil Jain, BJ Kim, Matthieu Le Tacon, and Bernhard Keimer. Raman scattering from higgs mode oscillations in the two-dimensional antiferromagnet Ca_2RuO_4 . *Physical Review Letters*, 119(6):067201, 2017.
- [38] G Cao, O Korneta, S Chikara, LE DeLong, and P Schlottmann. Non-fermi-liquid behavior in single-crystal CaRuO_3 : Comparison to ferromagnetic SrRuO_3 . *Solid State Communications*, 148(7-8):305–309, 2008.
- [39] Naoki Kikugawa, Luis Balicas, and Andrew Peter Mackenzie. Physical properties of single-crystalline CaRuO_3 grown by a floating-zone method. *Journal of the Physical Society of Japan*, 78(1):014701, 2008.
- [40] I Felner, I Nowik, I Bradaric, and M Gospodinov. CaRuO_3 is not a paramagnetic material. *Physical Review B*, 62(17):11332, 2000.
- [41] A Koriyama, M Ishizaki, TC Ozawa, T Taniguchi, Y Nagata, H Samata, Y Kobayashi, and Y Noro. Magnetism of CaRuO_3 crystal. *Journal of alloys and compounds*, 372(1-2):58–64, 2004.
- [42] T He and RJ Cava. Disorder-induced ferromagnetism in CaRuO_3 . *Physical Review B*, 63(17):172403, 2001.
- [43] JM Longo, PM Raccach, and JB Goodenough. Magnetic properties of SrRuO_3 and CaRuO_3 . *Journal of Applied Physics*, 39(2):1327–1328, 1968.
- [44] AP Mackenzie, JW Reiner, AW Tyler, LM Galvin, SR Julian, MR Beasley, TH Geballe, and A Kapitulnik. Observation of quantum oscillations in the electrical resistivity of SrRuO_3 . *Physical Review B*, 58(20):R13318, 1998.
- [45] P Kostic, Y Okada, NC Collins, Z Schlesinger, JW Reiner, L Klein, A Kapitulnik, TH Geballe, and MR Beasley. Non-fermi-liquid behavior of SrRuO_3 : evidence from infrared conductivity. *Physical Review Letters*, 81(12):2498, 1998.
- [46] DE Shai, Carolina Adamo, DW Shen, Charles M Brooks, JW Harter, Eric J Monkman, Bulat Burganov, Darrell G Schlom, and Kyle M Shen. Quasiparticle mass enhancement and temperature dependence of the electronic structure of ferromagnetic SrRuO_3 thin films. *Physical Review Letters*, 110(8):087004, 2013.
- [47] Zhong Fang, Naoto Nagaosa, Kei S Takahashi, Atsushi Asamitsu, Roland Mathieu, Takeshi Ogasawara, Hiroyuki Yamada, Masashi Kawasaki, Yoshinori Tokura, and Kiyoyuki Terakura. The anomalous hall effect and magnetic monopoles in momentum space. *Science*, 302(5642):92–95, 2003.
- [48] Marcos Verissimo-Alves, Pablo García-Fernández, Daniel I Bilc, Philippe Ghosez, and Javier Junquera. Highly confined spin-polarized two-dimensional electron gas in $\text{SrRuO}_3/\text{SrRuO}_3$ superlattices. *Physical review letters*, 108(10):107003, 2012.
- [49] Gertjan Koster, Lior Klein, Wolter Siemons, Guus Rijnders, J Steven Dodge, Chang-Beom Eom, Dave HA Blank, and Malcolm R Beasley. Structure, physical properties, and applications of SrRuO_3 thin films. *Reviews of Modern Physics*, 84(1):253, 2012.
- [50] CS Alexander, G Cao, V Dobrosavljevic, S McCall, JE Crow, E Lochner, and RP Guertin. Destruction of the mott insulating ground state of Ca_2RuO_4 by a structural transition. *Physical Review B*, 60(12):R8422, 1999.

- [51] L Das, F Forte, R Fittipaldi, CG Fatuzzo, V Granata, O Ivashko, M Horio, F Schindler, M Dantz, Yi Tseng, et al. Spin-orbital excitations in Ca_2RuO_4 revealed by resonant inelastic x-ray scattering. *Physical Review X*, 8(1):011048, 2018.
- [52] D Sutter, CG Fatuzzo, S Moser, M Kim, R Fittipaldi, A Vecchione, V Granata, Yasmine Sassa, F Cossalter, G Gatti, et al. Hallmarks of hunds coupling in the mott insulator Ca_2RuO_4 . *Nature communications*, 8(1):1–7, 2017.
- [53] Guoren Zhang and Eva Pavarini. Spin–orbit and coulomb effects in single-layered ruthenates. *physica status solidi (RRL)–Rapid Research Letters*, 12(11):1800211, 2018.
- [54] K Ishida, H Mukuda, Y Kitaoka, K Asayama, ZQ Mao, Y Mori, and Y Maeno. Spin-triplet superconductivity in Sr_2RuO_4 identified by ^{17}O knight shift. *Nature*, 396(6712):658–660, 1998.
- [55] Catherine Kallin and John Berlinsky. Chiral superconductors. *Reports on Progress in Physics*, 79(5):054502, 2016.
- [56] Yoshiteru Maeno, Shunichiro Kittaka, Takuji Nomura, Shingo Yonezawa, and Kenji Ishida. Evaluation of spin-triplet superconductivity in Sr_2RuO_4 . *Journal of the Physical Society of Japan*, 81(1):011009, 2011.
- [57] A Damascelli, DH Lu, KM Shen, NP Armitage, F Ronning, DL Feng, C Kim, Z-X Shen, T Kimura, Y Tokura, et al. Fermi surface, surface states, and surface reconstruction in Sr_2RuO_4 . *Physical review letters*, 85(24):5194, 2000.
- [58] AP Mackenzie, SR Julian, AJ Diver, GJ McMullan, MP Ray, GG Lonzarich, Y Maeno, S Nishizaki, and T Fujita. Quantum oscillations in the layered perovskite superconductor Sr_2RuO_4 . *Physical review letters*, 76(20):3786, 1996.
- [59] E Pavarini and II Mazin. First-principles study of spin-orbit effects and nmr in Sr_2RuO_4 . *Physical Review B*, 74(3):035115, 2006.
- [60] Stefan Kunkemöller, Daniel Khomskii, P Steffens, A Piovano, AA Nugroho, and M Braden. Highly anisotropic magnon dispersion in Ca_2RuO_4 : evidence for strong spin orbit coupling. *Physical Review Letters*, 115(24):247201, 2015.
- [61] H Gretarsson, H Suzuki, Hoon Kim, K Ueda, M Krautloher, BJ Kim, H Yavaş, G Khalullin, and B Keimer. Observation of spin-orbit excitations and hunds multiplets in Ca_2RuO_4 . *Physical Review B*, 100(4):045123, 2019.
- [62] SA Grigera, RS Perry, AJ Schofield, M Chiao, SR Julian, GG Lonzarich, SI Ikeda, Y Maeno, AJ Millis, and AP Mackenzie. Magnetic field-tuned quantum criticality in the metallic ruthenate $\text{Sr}_3\text{Ru}_2\text{O}_7$. *Science*, 294(5541):329–332, 2001.
- [63] C Lester, Silvia Ramos, RS Perry, TP Croft, RI Bewley, T Guidi, P Manuel, DD Khalyavin, EM Forgan, and SM Hayden. Field-tunable spin-density-wave phases in $\text{Sr}_3\text{Ru}_2\text{O}_7$. *Nature materials*, 14(4):373–378, 2015.
- [64] X Ke, J Peng, DJ Singh, Tao Hong, Wei Tian, CR Dela Cruz, and ZQ Mao. Emergent electronic and magnetic state in $\text{Ca}_3\text{Ru}_2\text{O}_7$ induced by ti doping. *Physical Review B*, 84(20):201102, 2011.
- [65] G. Cao, S. McCall, J. E. Crow, and R. P. Guertin. Observation of a metallic antiferromagnetic phase and metal to nonmetal transition in $\text{Ca}_3\text{Ru}_2\text{O}_7$. *Phys. Rev. Lett.*, 78:1751–1754, Mar 1997.
- [66] Naoki Kikugawa, Andreas Winfried Rost, Clifford William Hicks, Andrew John Schofield, and Andrew Peter Mackenzie. $\text{Ca}_3\text{Ru}_2\text{O}_7$: density wave formation and quantum oscillations in the hall resistivity. *Journal of the Physical Society of Japan*, 79(2):024704, 2010.

- [67] Yoshiyuki Yoshida, Shin-Ichi Ikeda, Hirofumi Matsuhata, Naoki Shirakawa, CH Lee, and Susumu Katano. Crystal and magnetic structure of $\text{Ca}_3\text{Ru}_2\text{O}_7$. *Physical Review B*, 72(5):054412, 2005.
- [68] G Cao, L Balicas, Y Xin, JE Crow, and CS Nelson. Quantum oscillations, colossal magnetoresistance, and the magnetoelastic interaction in bilayered $\text{Ca}_3\text{Ru}_2\text{O}_7$. *Physical Review B*, 67(18):184405, 2003.
- [69] G Cao, L Balicas, Y Xin, E Dagotto, JE Crow, CS Nelson, and DF Agterberg. Tunneling magnetoresistance and quantum oscillations in bilayered $\text{Ca}_3\text{Ru}_2\text{O}_7$. *Physical Review B*, 67(6):060406, 2003.
- [70] Maximilian Krautloher. *Neutron scattering studies on layered ruthenates*, 2018.
- [71] D. J. Singh and S. Auluck. Electronic structure and bulk spin-valve behavior in $\text{Ca}_3\text{Ru}_2\text{O}_7$. *Phys. Rev. Lett.*, 96:097203, Mar 2006.
- [72] Hui Xing, Libin Wen, Chenyi Shen, Jiaming He, Xinxin Cai, Jin Peng, Shun Wang, Mingliang Tian, Zhu-An Xu, Wei Ku, et al. Existence of electron and hole pockets and partial gap opening in the correlated semimetal $\text{Ca}_3\text{Ru}_2\text{O}_7$. *Physical Review B*, 97(4):041113, 2018.
- [73] F Baumberger, NJC Ingle, N Kikugawa, MA Hossain, W Meevasana, RS Perry, KM Shen, DH Lu, A Damascelli, A Rost, et al. Nested fermi surface and electronic instability in $\text{Ca}_3\text{Ru}_2\text{O}_7$. *Physical review letters*, 96(10):107601, 2006.
- [74] Claudia S Schnohr and Mark C Ridgway. *X-ray absorption spectroscopy of semiconductors*. Springer, 2015.
- [75] Jeroen A Van Bokhoven and Carlo Lamberti. *X-ray absorption and X-ray emission spectroscopy: theory and applications*, volume 1. John Wiley & Sons, 2016.
- [76] Kenneth Sauer, Junko Yano, and Vittal K Yachandra. X-ray spectroscopy of the photosynthetic oxygen-evolving complex. *Coordination chemistry reviews*, 252(3-4):318–335, 2008.
- [77] Luuk JP Ament, Michel Van Veenendaal, Thomas P Devereaux, John P Hill, and Jeroen Van Den Brink. Resonant inelastic x-ray scattering studies of elementary excitations. *Reviews of Modern Physics*, 83(2):705, 2011.
- [78] Federica Frati, Myrtille OJY Hunault, and Frank MF de Groot. Oxygen k-edge x-ray absorption spectra. *Chemical Reviews*, 120(9):4056–4110, 2020.
- [79] Claudia Giuseppina Fatuzzo. Spectroscopic studies of the electronic structure in layered cuprates and ruthenates. Technical report, EPFL, 2017.
- [80] G Ghiringhelli, Andrea Piazzalunga, Claudia Dallera, Gabriele Trezzi, Lucio Braicovich, T Schmitt, VN Strocov, R Betemps, L Patthey, X Wang, et al. Saxs, a high resolution spectrometer for resonant x-ray emission in the 400–1600 eV energy range. *Review of Scientific Instruments*, 77(11):113108, 2006.
- [81] VN Strocov, T Schmitt, U Flechsig, T Schmidt, A Imhof, Q Chen, J Raabe, R Betemps, D Zimoch, J Krempasky, et al. High-resolution soft x-ray beamline address at the swiss light source for resonant inelastic x-ray scattering and angle-resolved photoelectron spectroscopies. *Journal of synchrotron radiation*, 17(5):631–643, 2010.
- [82] Felix Marschall, Daniel McNally, Vitaliy A Guzenko, Benedikt Rösner, Marcus Dantz, Xingye Lu, Leonard Nue, Vladimir Strocov, Thorsten Schmitt, and Christian David. Zone plates as imaging analyzers for resonant inelastic x-ray scattering. *Optics express*, 25(14):15624–15634, 2017.

- [83] Thorsten Schmitt, Vladimir N Strocov, Ke-Jin Zhou, Justine Schlappa, Claude Monney, Uwe Flechsig, and Luc Patthey. High-resolution resonant inelastic x-ray scattering with soft x-rays at the adress beamline of the swiss light source: Instrumental developments and scientific highlights. *Journal of Electron Spectroscopy and Related Phenomena*, 188:38–46, 2013.
- [84] Matteo Minola. Magnetic, orbital and charge fluctuations in layered cuprates studied by resonant soft x-ray scattering. 2013.
- [85] M Moretti Sala, Valentina Bisogni, C Aruta, G Balestrino, H Berger, NB Brookes, GM De Luca, D Di Castro, M Grioni, M Guarise, et al. Energy and symmetry of dd excitations in undoped layered cuprates measured by cu l3 resonant inelastic x-ray scattering. *New Journal of Physics*, 13(4):043026, 2011.
- [86] K von Arx, F Forte, M Horio, V Granata, Q Wang, L Das, Y Sassa, R Fittipaldi, CG Fatuzzo, O Ivashko, et al. Comparative resonant inelastic x-ray scattering study of ca₂ruo₄ and ca₃ru₂o₇. *arXiv preprint arXiv:2004.13391*, 2020.
- [87] NB Brookes, F Yakhou-Harris, K Kummer, A Fondacaro, JC Cezar, D Betto, E Velez-Fort, A Amorese, G Ghiringhelli, L Braicovich, et al. The beamline id32 at the esrf for soft x-ray high energy resolution resonant inelastic x-ray scattering and polarisation dependent x-ray absorption spectroscopy. *Nuclear Instruments and Methods in Physics Research Section A: Accelerators, Spectrometers, Detectors and Associated Equipment*, 903:175–192, 2018.
- [88] Charles Kittel et al. *Introduction to solid state physics*, volume 8. Wiley New York, 1976.
- [89] Chihiro Hamaguchi and C Hamaguchi. *Basic semiconductor physics*, volume 9. Springer, 2010.
- [90] Quantum Design. Ppms resistivity option user’s manual. *PPMS Hardware and Options Manual*, 2004.
- [91] Daniel Destraz. *Electric Transport in Quantum Matter Systems*. PhD thesis, University of Zurich, 2019.
- [92] Bo Peng, Hao Zhang, Hezhu Shao, Hongliang Lu, David Wei Zhang, and Heyuan Zhu. High thermoelectric performance of weyl semimetal taas. *Nano energy*, 30:225–234, 2016.
- [93] A. v. Etingshausen and W. Nernst. Ueber das auftreten electromotorischer kräfte in metallplatten, welche von einem wärmestrome durchflossen werden und sich im magnetischen felde befinden. *Annalen der Physik*, 265(10):343–347, 1886.
- [94] AS Alexandrov and VN Zavaritsky. Nernst effect in poor conductors and in the cuprate superconductors. *Physical review letters*, 93(21):217002, 2004.
- [95] Brian Skinner and Liang Fu. Large, nonsaturating thermopower in a quantizing magnetic field. *Science advances*, 4(5):eaat2621, 2018.
- [96] Kamran Behnia and Hervé Aubin. Nernst effect in metals and superconductors: a review of concepts and experiments. *Reports on Progress in Physics*, 79(4):046502, 2016.
- [97] Nevill Francis Mott and Harry Jones. *The theory of the properties of metals and alloys*. Courier Corporation, 1958.
- [98] Daniel Destraz, Lakshmi Das, Stepan S Tsirkin, Yang Xu, Titus Neupert, J Chang, A Schilling, Adolfo G Grushin, Joachim Kohlbrecher, Lukas Keller, et al. Magnetism and anomalous transport in the weyl semimetal pralge: possible route to axial gauge fields. *npj Quantum Materials*, 5(1):1–8, 2020.

- [99] Guoqing Chang, Bahadur Singh, Su-Yang Xu, Guang Bian, Shin-Ming Huang, Chuang-Han Hsu, Ilya Belopolski, Nasser Alidoust, Daniel S Sanchez, Hao Zheng, et al. Magnetic and noncentrosymmetric weyl fermion semimetals in the rare earth family of compounds (rare earth). *Physical Review B*, 97(4):041104, 2018.
- [100] J-R Soh, F De Juan, MG Vergniory, NBM Schröter, MC Rahn, DY Yan, J Jiang, M Bristow, PA Reiss, JN Blandy, et al. Ideal weyl semimetal induced by magnetic exchange. *Physical Review B*, 100(20):201102, 2019.
- [101] Sarah J Watzman, Timothy M McCormick, Chandra Shekhar, Shu-Chun Wu, Yan Sun, Arati Prakash, Claudia Felser, Nandini Trivedi, and Joseph P Heremans. Dirac dispersion generates unusually large nernst effect in weyl semimetals. *Physical Review B*, 97(16):161404, 2018.
- [102] Hamza Balci. *Specific heat and Nernst effect of electron-doped cuprate superconductors*. PhD thesis, 2004.
- [103] M Buchner, K Höfler, B Henne, V Ney, and A Ney. Tutorial: Basic principles, limits of detection, and pitfalls of highly sensitive squid magnetometry for nanomagnetism and spintronics. *Journal of Applied Physics*, 124(16):161101, 2018.
- [104] MPMS Users Manual. Quantum design 1995; sager re, hibbs ad and kumar s. *IEEE Trans. Magn.*, 28:3072, 1992.
- [105] BN Sahu, KG Suresh, N Venkataramani, Shiva Prasad, and R Krishnan. Temperature and field dependent magnetization studies on nano-crystalline znfe₂o₄ thin films. *AIP Advances*, 8(5):056118, 2018.
- [106] PA Joy, PS Anil Kumar, and SK Date. The relationship between field-cooled and zero-field-cooled susceptibilities of some ordered magnetic systems. *Journal of physics: condensed matter*, 10(48):11049, 1998.
- [107] Simon Joehr. *Removing Domain Boundaries in La₂CuO₄, Ca₃Ru₂O₇ and YBa₂Cu₃O_{7-x} using a Thermo-Mechanical Detwinning Device*, 2019.
- [108] Karin Von Arx. *Discovery of a Collective Orbital Excitation in Ca₃Ru₂O₇*, 2019.
- [109] VV Voronkov, EI Givargizov, and AM Melnikova. Growth of crystals. 1986.
- [110] Ernest Burkhardt, Z-G Ye, and Hans Schmid. Low and high temperature uniaxial stress devices for the study of ferroelastic crystals. *Review of scientific instruments*, 66(7):3888–3893, 1995.
- [111] Satoru Nakatsuji and Y Maeno. Quasi-two-dimensional mott transition system ca_{2-x}sr_xruo₄. *Physical review letters*, 84(12):2666, 2000.
- [112] Guoren Zhang and Eva Pavarini. Mott transition, spin-orbit effects, and magnetism in ca₂ruo₄. *Physical Review B*, 95(7):075145, 2017.
- [113] Richard JD Tilley. *Perovskites: structure-property relationships*. John Wiley & Sons, 2016.
- [114] LM Woods. Electronic structure of ca₂ruo₄: a comparison with the electronic structures of other ruthenates. *Physical Review B*, 62(12):7833, 2000.
- [115] M Braden, G André, S Nakatsuji, and Y Maeno. Crystal and magnetic structure of ca₂ruo₄: Magnetoelastic coupling and the metal-insulator transition. *Physical Review B*, 58(2):847, 1998.
- [116] Zhong Fang, Naoto Nagaosa, and Kiyoyuki Terakura. Orbital-dependent phase control in ca_{2-x}sr_xruo₄ (0 < x < 0.5). *Physical Review B*, 69(4):045116, 2004.

- [117] M Neupane, P Richard, Z-H Pan, Y-M Xu, R Jin, David Mandrus, X Dai, Z Fang, Z Wang, and H Ding. Observation of a novel orbital selective mott transition in $\text{Ca}_{1.8}\text{Sr}_{0.2}\text{RuO}_4$. *Physical review letters*, 103(9):097001, 2009.
- [118] A Liebsch and H Ishida. Subband filling and mott transition in $\text{Ca}_{2-x}\text{Sr}_x\text{RuO}_4$. *Physical review letters*, 98(21):216403, 2007.
- [119] Guo-Qiang Liu. Spin-orbit coupling induced mott transition in $\text{Ca}_{2-x}\text{Sr}_x\text{RuO}_4$. *Physical Review B*, 84(23):235136, 2011.
- [120] VI Anisimov, IA Nekrasov, DE Kondakov, TM Rice, and M Sigrist. Orbital-selective mott-insulator transition in $\text{Ca}_{2-x}\text{Sr}_x\text{RuO}_4$. *The European Physical Journal B-Condensed Matter and Complex Systems*, 25(2):191–201, 2002.
- [121] A Shimoyamada, K Ishizaka, S Tsuda, S Nakatsuji, Y Maeno, and S Shin. Strong mass renormalization at a local momentum space in multiorbital $\text{Ca}_{1.8}\text{Sr}_{0.2}\text{RuO}_4$. *Physical review letters*, 102(8):086401, 2009.
- [122] BJ Kim and Giniyat Khaliullin. Resonant inelastic x-ray scattering operators for t_2g orbital systems. *Physical Review B*, 96(8):085108, 2017.
- [123] BJ Kim, Hosub Jin, SJ Moon, J-Y Kim, B-G Park, CS Leem, Jaejun Yu, TW Noh, C Kim, S-J Oh, et al. Novel $j_{\text{eff}}=1/2$ mott state induced by relativistic spin-orbit coupling in Sr_2IrO_4 . *Physical review letters*, 101(7):076402, 2008.
- [124] Hideto Fukazawa, Satoru Nakatsuji, and Yoshiteru Maeno. Intrinsic properties of the mott insulator $\text{Ca}_{2-x}\text{Sr}_x\text{RuO}_4$ ($\delta=0$) studied with single crystals. *Physica B: Condensed Matter*, 281:613–614, 2000.
- [125] Satoru Nakatsuji and Yoshiteru Maeno. Synthesis and single-crystal growth of $\text{Ca}_{2-x}\text{Sr}_x\text{RuO}_4$. *Journal of Solid State Chemistry*, 156(1):26–31, 2001.
- [126] Marco Malvestuto, V Capogrosso, E Carleschi, L Galli, E Gorelov, E Pavarini, R Fittipaldi, F Forte, M Cuoco, A Vecchione, et al. Nature of the apical and planar oxygen bonds in the $\text{Sr}_{n+1}\text{Ru}_n\text{O}_{3n+1}$ family ($n=1, 2, 3$). *Physical Review B*, 88(19):195143, 2013.
- [127] M Malvestuto, E Carleschi, R Fittipaldi, E Gorelov, E Pavarini, M Cuoco, Y Maeno, Fulvio Parmigiani, and A Vecchione. Electronic structure trends in the $\text{Sr}_{n+1}\text{Ru}_n\text{O}_{3n+1}$ family ($n=1, 2, 3$). *Physical Review B*, 83(16):165121, 2011.
- [128] M Schmidt, TR Cummins, M Bürk, DH Lu, N Nücker, S Schuppler, and F Lichtenberg. Nature of the electronic states in the layered perovskite noncuprate superconductor Sr_2RuO_4 . *Physical Review B*, 53(22):R14761, 1996.
- [129] CG Fatuzzo, M Dantz, S Fatale, P Olalde-Velasco, NE Shaik, B Dalla Piazza, S Toth, J Pellicciari, R Fittipaldi, A Vecchione, et al. Spin-orbit-induced orbital excitations in Sr_2RuO_4 and Ca_2RuO_4 : a resonant inelastic x-ray scattering study. *Physical Review B*, 91(15):155104, 2015.
- [130] David J Singh. Relationship of Sr_2RuO_4 to the superconducting layered cuprates. *Physical Review B*, 52(2):1358, 1995.
- [131] Mathieu Le Tacon, G Ghiringhelli, J Chaloupka, M Moretti Sala, V Hinkov, MW Haverkort, Matteo Minola, M Bakr, KJ Zhou, S Blanco-Canosa, et al. Intense paramagnon excitations in a large family of high-temperature superconductors. *Nature Physics*, 7(9):725–730, 2011.
- [132] Jagat Lamsal and Wouter Montfrooij. Extracting paramagnon excitations from resonant inelastic x-ray scattering experiments. *Physical Review B*, 93(21):214513, 2016.

- [133] C Monney, T Schmitt, CE Matt, J Mesot, VN Strocov, OJ Lipscombe, SM Hayden, and J Chang. Resonant inelastic x-ray scattering study of the spin and charge excitations in the overdoped superconductor $\text{La}_{1.77}\text{Sr}_{0.23}\text{CuO}_4$. *Physical Review B*, 93(7):075103, 2016.
- [134] Claudia Cancellieri and Vladimir N Strocov. *Spectroscopy of Complex Oxide Interfaces*. Springer, 2018.
- [135] Luuk JP Ament, Filomena Forte, and Jeroen van den Brink. Ultrashort lifetime expansion for indirect resonant inelastic x-ray scattering. *Physical Review B*, 75(11):115118, 2007.
- [136] *Supplemental for Spin Orbital excitations in Ca₂RuO₄*.
- [137] CN Veenstra, Z-H Zhu, M Raichle, BM Ludbrook, A Nicolaou, B Slomski, G Landolt, S Kittaka, Y Maeno, JH Dil, et al. Spin-orbital entanglement and the breakdown of singlets and triplets in Sr_2RuO_4 revealed by spin- and angle-resolved photoemission spectroscopy. *Physical review letters*, 112(12):127002, 2014.
- [138] Jungho Kim, M Daghofer, AH Said, T Gog, J Van den Brink, G Khaliullin, and BJ Kim. Excitonic quasiparticles in a spin-orbit mott insulator. *Nature communications*, 5(1):1–6, 2014.
- [139] XN Lin, ZX Zhou, V Durairaj, P Schlottmann, and G Cao. Colossal magnetoresistance by avoiding a ferromagnetic state in the mott system $\text{Ca}_3\text{Ru}_2\text{O}_7$. *Physical review letters*, 95(1):017203, 2005.
- [140] V Durairaj, XN Lin, ZX Zhou, S Chikara, E Ehami, A Douglass, P Schlottmann, and G Cao. Observation of oscillatory magnetoresistance periodic in $1/b$ and b in $\text{Ca}_3\text{Ru}_2\text{O}_7$. *Physical Review B*, 73(5):054434, 2006.
- [141] Wei Bao, Z Qu Mao, Z Qu, and JW Lynn. Spin valve effect and magnetoresistivity in single crystalline $\text{Ca}_3\text{Ru}_2\text{O}_7$. *Physical review letters*, 100(24):247203, 2008.
- [142] I Marković, MD Watson, OJ Clark, F Mazzola, E Abarca Morales, CA Hooley, H Rosner, CM Polley, T Balasubramanian, S Mukherjee, et al. Electronically driven spin-reorientation transition of the correlated polar metal $\text{Ca}_{-3}\text{Ru}_{-2}\text{O}_{-7}$. *arXiv preprint arXiv:2001.09499*, 2020.
- [143] Danilo Puggioni, M Horio, J Chang, and James M Rondinelli. Cooperative interactions govern the fermiology of the polar metal $\text{Ca}_3\text{Ru}_2\text{O}_7$. *Physical Review Research*, 2(2):023141, 2020.
- [144] Benoît Fauqué, Xiaojun Yang, Wojciech Tabis, Mingsong Shen, Zengwei Zhu, Cyril Proust, Yuki Fuseya, and Kamran Behnia. Magnetoresistance of semimetals: The case of antimony. *Physical Review Materials*, 2(11):114201, 2018.
- [145] AF Bangura, Cyril Proust, J Levallois, N Doiron-Leyraud, D LeBoeuf, L Taillefer, S Adachi, ML Sutherland, and NE Hussey. Fermi-surface reconstruction and two-carrier model for the hall effect in $\text{YbBa}_2\text{Cu}_4\text{O}_8$. *Physical Review B*, 82(2):020514, 2010.
- [146] P. M. C. Rourke, A. F. Bangura, C. Proust, J. Levallois, N. Doiron-Leyraud, D. LeBoeuf, L. Taillefer, S. Adachi, M. L. Sutherland, and N. E. Hussey. Fermi-surface reconstruction and two-carrier model for the hall effect in $\text{YbBa}_2\text{Cu}_4\text{O}_8$. *Phys. Rev. B*, 82:020514, Jul 2010.
- [147] David LeBoeuf, Nicolas Doiron-Leyraud, Julien Levallois, Ramzy Daou, J-B Bonnemaïson, NE Hussey, Luis Balicas, BJ Ramshaw, Ruixing Liang, DA Bonn, et al. Electron pockets in the fermi surface of hole-doped high- T_c superconductors. *Nature*, 450(7169):533–536, 2007.

- [148] Nicholas P Breznay, Ian M Hayes, BJ Ramshaw, Ross D McDonald, Yoshiharu Krockenberger, Ai Ikeda, Hiroshi Irie, Hideki Yamamoto, and James G Analytis. Shubnikov-de haas quantum oscillations reveal a reconstructed fermi surface near optimal doping in a thin film of the cuprate superconductor $\text{Pr}_{1.86}\text{Ce}_{0.14}\text{CuO}_{4\pm\delta}$. *Physical Review B*, 94(10):104514, 2016.
- [149] Mazhar N Ali, Jun Xiong, Steven Flynn, Jing Tao, Quinn D Gibson, Leslie M Schoop, Tian Liang, Neel Haldolaarachchige, Max Hirschberger, Nai Phuan Ong, et al. Large, non-saturating magnetoresistance in wTe_2 . *Nature*, 514(7521):205–208, 2014.
- [150] PB Alers and RT Webber. The magnetoresistance of bismuth crystals at low temperatures. *Physical Review*, 91(5):1060, 1953.
- [151] DoE Soule. Magnetic field dependence of the hall effect and magnetoresistance in graphite single crystals. *physical review*, 112(3):698, 1958.
- [152] Zhe Qu, Jin Peng, Tijiang Liu, David Fobes, Vlad Dobrosavljević, Leonard Spinu, and ZQ Mao. Effect of disorder on quantum phase transition in the double layered ruthenates $(\text{Sr}_{1-x}\text{Ca}_x)_3\text{Ru}_2\text{O}_7$. *Physical Review B*, 86(1):014434, 2012.
- [153] Eric Vincent and Vincent Dupuis. Spin glasses: experimental signatures and salient outcomes. In *Frustrated Materials and Ferromagnetic Glasses*, pages 31–56. Springer, 2018.
- [154] Hiroshi Yamada and Satoshi Takada. Negative magnetoresistance of ferromagnetic metals due to spin fluctuations. *Progress of theoretical physics*, 48(6):1828–1848, 1972.
- [155] NP Armitage, EJ Mele, and Ashvin Vishwanath. Weyl and dirac semimetals in three-dimensional solids. *Reviews of Modern Physics*, 90(1):015001, 2018.
- [156] Daniel S Sanchez, Guoqing Chang, Ilya Belopolski, Hong Lu, Jia-Xin Yin, Nasser Alidoust, Xitong Xu, Tyler A Cochran, Xiao Zhang, Yi Bian, et al. Observation of weyl fermions in a magnetic non-centrosymmetric crystal. *Nature Communications*, 11(1):1–8, 2020.
- [157] Akito Sakai, Yo Pierre Mizuta, Agustinus Agung Nugroho, Rombang Sihombing, Takashi Koretsune, Michi-To Suzuki, Nayuta Takemori, Rieko Ishii, Daisuke Nishio-Hamane, Ryotaro Arita, et al. Giant anomalous nernst effect and quantum-critical scaling in a ferromagnetic semimetal. *Nature Physics*, 14(11):1119–1124, 2018.
- [158] LX Yang, ZK Liu, Yan Sun, Han Peng, HF Yang, Teng Zhang, Bo Zhou, Yi Zhang, YF Guo, Marein Rahn, et al. Weyl semimetal phase in the non-centrosymmetric compound TaAs . *Nature physics*, 11(9):728–732, 2015.
- [159] Max Hirschberger, Satya Kushwaha, Zhijun Wang, Quinn Gibson, Sihang Liang, Carina A Belvin, Bogdan Andrei Bernevig, Robert Joseph Cava, and Nai Phuan Ong. The chiral anomaly and thermopower of weyl fermions in the half-heusler GdPtBi . *Nature materials*, 15(11):1161–1165, 2016.
- [160] K Kuroda, T Tomita, M-T Suzuki, C Bareille, AA Nugroho, Pallab Goswami, M Ochi, M Ikhlās, M Nakayama, S Akebi, et al. Evidence for magnetic weyl fermions in a correlated metal. *Nature materials*, 16(11):1090–1095, 2017.
- [161] Enke Liu, Yan Sun, Nitesh Kumar, Lukas Muechler, Aili Sun, Lin Jiao, Shuo-Ying Yang, Defa Liu, Aiji Liang, Qiunan Xu, et al. Giant anomalous hall effect in a ferromagnetic kagome-lattice semimetal. *Nature physics*, 14(11):1125–1131, 2018.
- [162] Shuang Jia, Su-Yang Xu, and M Zahid Hasan. Weyl semimetals, fermi arcs and chiral anomalies. *Nature materials*, 15(11):1140–1144, 2016.
- [163] Ashvin Vishwanath. Where the weyl things are. *Physics*, 8:84, 2015.

- [164] Lin-Lin Wang, Na Hyun Jo, Brinda Kuthanazhi, Yun Wu, Robert J McQueeney, Adam Kaminski, and Paul C Canfield. Single pair of weyl fermions in the half-metallic semimetal EuCd_2As_2 . *Physical Review B*, 99(24):245147, 2019.
- [165] J-Z Ma, SM Nie, CJ Yi, Jasmin Jandke, Tian Shang, Meng-Yu Yao, Muntaser Naamneh, LQ Yan, Yan Sun, Alla Chikina, et al. Spin fluctuation induced weyl semimetal state in the paramagnetic phase of EuCd_2As_2 . *Science advances*, 5(7):eaaw4718, 2019.
- [166] Yang.Xu et.al. Private Communication, 2020.